Università di Torino
Doctoral School of the University of Torino
PhD Programme in Chemical and Materials Sciences XXXV Cycle

Incorporation of Fe^{II} complex in Metal-Organic Frameworks as a possible way to increase excited state lifetimes

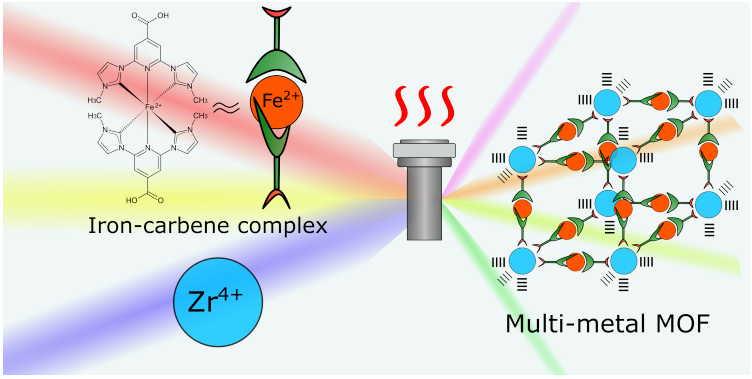

Luca Andreo

Supervisor:
Prof. Eliano Diana

UNIVERSITÀ
DI TORINO

Università di Torino
Doctoral School of the University of Torino
PhD Programme in Chemical and Materials Sciences XXXV Cycle

Incorporation of Fe^{II} complex in Metal-Organic Frameworks as a possible way to increase excited state lifetimes

Candidate: **Luca Andreo**

Supervisor: **Prof. Eliano Diana**
Università di Torino
Dipartimento di Chimica

Jury Members: **Prof.ssa Cristina Femoni**
Università di Bologna
Dipartimento di Chimica Industriale "Toso Montanari"

Prof. Davide Maria Proserpio
Università di Milano
Dipartimento di Chimica

Prof. Roberto Gobetto
Università di Torino
Dipartimento di Chimica

Head of the Doctoral School: Prof. Alberto Rizzuti
PhD Programme Coordinator: Prof. Bartolomeo Civalleri

Torino, July 14th 2023

Acknowledgements

First, I want to thank my supervisor, Professor Eliano Diana, for the scientific and human support during this path. It has been a pleasure working with him, and I could learn many things about different fields of science, from chemistry to cultural heritage. I am very grateful to Professor Giuseppina Cerrato, for putting a lot of trust in me and for all the opportunities she gave me, as well as the wonderful experiences of scientific dissemination she included me in. Both professors helped me feeling valorised as a person and as a scientist.

The PhD is a complicated path, difficult to explain to other people. Just as all the things in life, it has ups and downs, events we are grateful for and others that we would like to avoid. It is generally very stressful, and for many different reasons, from difficult and daunting tasks to unsuccessful results and very strict deadlines. I think that everyone has a unique experience of the PhD, and it is very common to feel alone and discouraged. However, I feel I have been very lucky in finding a very nice environment here in Turin, and thus my very special thanks go to all the "fourth floor" of via Giuria 7.

I want to thank Emanuele, for all the scientific discussions, the projects he included me in, the assistance; for the nice music played in his office, for the small chats and the many cultural references he always makes, and for the nice time spent together outside the university. I want to thank Alessia, for all the precious scientific discussions in the lab, the help and support she constantly provided me, the scientific advice on many different things (especially in vibrational spectroscopy) and the passion for science she instilled in me; thanks for having shared with me personal ideas, thoughts, deep conversations, doubts about the future and life in general,

and for all the time spent together. Thanks to Maria, for the awesome discussions about cultural heritage, conservation science, and for having allowed me to know more about this amazing topic. Her company and scientific discussions during PhD lessons and courses made me appreciate the "PhD life". Thanks for the meaningful discussions about life, for the help in difficult situations, for helping me observe things from a different perspective. All these four people really helped me growing up as a scientist, but most importantly as a human being. I am very happy and grateful for having had the opportunity to share these years with them. To all of them, a special thanks for sharing their life with me, and having endured my stubbornness! I want to thank Benedetta, for her support in the office especially during the last months of my PhD, for the concerts we attended to, and for the nice talks and moments we shared. Thanks to Elisabetta and Francesca, whose presence, talks and moments spent together made me feel part of a group. And thanks for the scientific dissemination activities we carried out together, helping me realise the beauty in sharing the knowledge with others.

Thanks to Simone Ghinato and Emanuele Azzi, two wonderful organic chemists, for their precious discussions and help with organic synthesis and chromatography when I most needed it. Thanks to Ettore Bianco and Francesco Pellegrino, for the help and assistance they provided during the photocatalytic measurements: without them I would not have been able to carry out the last measurements for my thesis. Thanks to Professor Maurino and Professor Deagostino, for letting me work in their labs for photocatalytic measurements and organic syntheses, respectively.

I want to thank my friend and colleague Davide Bernasconi: we shared a common path during the undergraduate and postgraduate studies, and we both started the PhD at the same time. He provided both human and scientific support in these years, and I am very grateful for that. I also want to thank all the undergraduate and postgraduate students who worked in the fourth floor labs; their enthusiasm, curiosity and willingness to learn in the lab were a motivational boost!

Special thanks to the research group in Bilbao, at BCMaterials, where I stayed for six months: thanks to Professor Stefan Wuttke for welcoming me in his research group, providing me many opportunities and a different perspective on scientific work; thanks to Madeline, Orysia, Nagore, Xian-

jiang and Anna, for sharing many nice moments in the Basque country, as well as sharing the lab and learning from one another; and a special thanks to Jacopo and Francesca, who took me under their wing during my stay in Bilbao, significantly helping me develop as a scientist, and sharing tons of social and fun moments throughout my stay. Without them, my PhD path would not have been the same, and I am very grateful to them for the experiences we shared together!

I want to acknowledge the choral associations where I sing in, *Coro La Manda* and *Coro La Rupe*, for having provided a safe environment where I could decompress my mind after the tough weeks. Singing with friends helped to relieve stress and to carry out my path in a better way.

Finally, the most heartfelt thanks go to my family: to my brother with Elisabetta, to my father and my mother, for their endless support, their constant presence during all these years and their tireless work, which have been key factors leading me where I am today.

Contents

Chapter 1

Introduction

The importance of harnessing the power of light was pointed out by the Italian chemist Giacomo Ciamician in 1912 [1]. He was the first to envision a world relying totally on solar energy, where the chemical industry of the future would have played a crucial role, thanks to the production of new substances without fossil fuel consumption. Nearly 100 years after Ciamician's words, harvesting solar energy and exploiting it for synthetic purposes is still one of the greatest challenges of our days, and it is among the most intriguing and complex fields in chemistry as well. Even if Ciamician's vision of "forests of glass tubes" that "will extend over the plains" as new industries relying only on solar energy is still a mirage, it pushed scientists towards research on fundamental aspects of photochemistry and photophysics, not just for the mere pleasure to discover and study something new, but also for solving a problem that is nowadays very critical, that is the quest for cleaner energy. Many of the secret processes of nature regarding photochemistry mentioned by the italian chemist more than one hundred years ago have been unveiled by scientists, and great discoveries and knowledge have been achieved during the last century. In the following sections we will briefly resume the most important concepts regarding the field of photochemistry and photophysics, with a special attention to metal complexes and their uses in photo-driven reactions.

1.1 Photochemistry and photophysics: general concepts

The effects of light on matter have been studied and observed as long as chemistry started developing as a science. The first observations of Carl Wilhelm Scheele in 1777 on the darkening of silver chloride were perfected by Theodor von Grotthuss in 1817, who established that *only the light absorbed is effective in producing a photochemical change*. This is considered as the first principle of photochemistry, also known as Grotthuss-Draper law, since John William Draper was the one restating this concept in 1841. At the beginning of 1900, the concept of photons and their quantized energy were developed, and a relation between light absorption and capture of a photon by an atom or molecule was established. Johannes Stark and Albert Einstein independently formulated the photoequivalence law (second law of photochemistry), which assesses that *there should be a* $1:1$ *equivalence between the number of molecules decomposed and the number of photons absorbed*. However, this ratio was not always experimentally observed, leading to the distinction between *photochemical primary processes*, that is processes directly initiated by light absorption, and *photochemical secondary processes*, for all the subsequent events or reactions following a primary process. This distinction preserves the second principle of photochemistry, acknowledging that chain reactions may occur after the absorption of only one photon [2].

The development in physics in the twentieth century allowed to understand and rationalise the photoprocesses: the absorption of a photon with a frequency ν corresponds to the absorption of an energy:

$$E = h\nu \tag{1.1}$$

where $h = 6.63 \cdot 10^{-34}$ J s. In the case of a molecule A that absorbs one photon, a chemical equation can be written:

$$\mathrm{A} + h\nu \longrightarrow \mathrm{A}^* \tag{1}$$

"A" denotes a generic molecule in its *ground state*, while A^* denotes the same molecule in an *excited state*. This example can be extended to one mole of A, absorbing one mole of photons, that is *one einstein* of photons.

The absorption of monochromatic light by a substance dissolved in a transparent medium is described by the Lambert-Beer law: the attenuation of the intensity of the incident light (I_0) decreases as follows:

$$I = I_0 \cdot 10^{-\epsilon b C} \tag{1.2}$$

where ϵ is the molar absorption coefficient ($\text{mol}^{-1} \cdot \text{L} \cdot \text{cm}^{-1}$), b is the optical path (cm) and C is the molar concentration of the solution ($\text{mol} \cdot \text{L}^{-1}$). The molar absorption coefficient is proportional to the ability of the molecule to absorb light, and it is wavelength dependent; the logarithmic ratio between the transmitted (I) and the incident intensities is the absorbance:

$$A = -\log(\frac{I}{I_0}) = \epsilon b C \tag{1.3}$$

A molecule can absorb one photon if the energy of the photon matches the energy difference between excited state (E_f) and ground state (E_i):

$$h\nu = E_f - E_i \tag{1.4}$$

The excited state of a molecule differs from the ground state not only for the amount of energy, but also for the electronic distribution, since the transition involves a rearrangement of electron density in the molecule. Since physical and chemical properties are linked to the electron distribution of a compound, a molecule in one excited state can be seen as a different molecule compared to those in the ground state. On the other hand, an excited state is intrinsically a transient species, since the excess of energy acquired during the transition can be released in different forms. A photoexcited molecule A^* can undergo different types of reactions, with their respective rate constants:

$$^*\text{A} \xrightarrow{k_r} \text{A} + h\nu \qquad \textit{radiative deactivation} \qquad \{2\}$$

$$^*\text{A} \xrightarrow{k_p} \text{Products} \qquad \textit{photoreaction} \qquad \{3\}$$

$$^*\text{A} \xrightarrow{k_{nr}} \text{A} + \text{heat} \qquad \textit{non-radiative deactivation} \qquad \{4\}$$

Reaction 2 is the *radiative deactivation*: the photoexcited molecule releases the extra energy through emission of a photon. The emitted photon

has an energy lower than the one which generated the photoexcited state. This happens because the electron transition populates "hot" excited states, that is vibrational excited states within electronic excited states: a vibrational relaxation dissipates a small amount of energy (*internal conversion*), yielding a "cold" excited state, whose energy is smaller than the transition which generated it. Reaction 3 is a general example of photoinduced chemical reaction, which can involve only the photoexcited molecule (e.g. an isomerisation) or the interaction of other molecules (e.g. photo-induced electron transfer, photo-oxidation, photo-reduction). Reaction 4 depicts the photoexcitation decay without emission of photon, and can happen between isoenergetic vibrational levels of different electronic states [2]; in other words, it is a coupling between vibrational states of two different electronic states.

All these processes are in competition among themselves, and are directly involved in defining the behaviour of the excited molecule, as well as the lifetime of the excited state, which indicates how long the molecule can stay in the excited state. Since the previously mentioned reactions can be described with first order kinetics, the total lifetime of the excited state $\tau(^*\mathrm{A})$ can be written as:

$$\tau(^*\mathrm{A}) = \frac{1}{k_r + k_p + k_{nr}} = \frac{1}{\sum\limits_j k_j} \tag{1.5}$$

The probability of a photodeactivation pathway is proportional to its relative rate, the *efficiency* for each process being described as:

$$\eta_i(^*\mathrm{A}) = \frac{k_i}{\sum\limits_j k_j} = k_i \tau(^*\mathrm{A}) \tag{1.6}$$

For one photochemical primary processes, the *quantum yield* can be defined as the ratio between the number of molecules undergoing the process per unit time and the number of photons absorbed per unit time. Only for primary processes, it can be demonstrated that the quantum yield Φ is numerically equal to the efficiency for that process. However, when excited states are originated from inter-system crossing or internal conversion, their photochemical and photophysical processes exhibit quantum yields which

take account of the efficiencies of the n previous steps that lead to the formation of *A:

$$\Phi_i(^*\mathrm{A}) = \eta_i(^*\mathrm{A}) \prod_n \eta_n \tag{1.7}$$

Using equation 1.6, the rate constant of a process for excited states generated as secondary process can be written as:

$$k_i = \frac{\Phi_i(^*\mathrm{A})}{\tau(^*\mathrm{A}) \prod_n \eta_n} \tag{1.8}$$

For metal complexes (especially for the second and third row metals of the periodic table), the high spin-orbit coupling grants intersystem crossing (ISC) efficiencies next to the unity, which means that the first generated excited states can decay to lower energy ones with different spin states. Thus, for these metal complexes phenomena such as emission occur from the lowest spin-forbidden excited state (phosphorescence), while in organic molecules, where spin-orbit coupling is very low, intersystem crossing is more rare, and usually the emission occurs from spin-allowed excited states (fluorescence).

1.1.1 Electron transfer

As already stated, the excited state can be regarded as a new molecule, with different properties and reactivity. A very interesting feature of photoexcited molecules concerns the electron transfer processes which can happen: if we simplify an electronic transition and imagine it as the promotion of one electron towards higher energy orbitals, we must recognize that the photoexcited molecule contains both a "hole", that is an electron missing from the highest occupied orbitals of the ground state, and a loosely bound electron, which is the photoexcited one. This means that the photoexcited molecule can be a better oxidant and reductant compared to the same molecule in the ground state. A relation exists between ground and excited state redox potential, and it can be demonstrated that a rough estimation of the latter can be given by the following equations:

$$E^0(\mathrm{A}^+/\mathrm{A}^*) = E^0(\mathrm{A}^+/\mathrm{A}) - E_{00}(\mathrm{A}^*/\mathrm{A}) \tag{1.9}$$

$$E^0(\mathrm{A}^*/\mathrm{A}^-) = E^0(\mathrm{A}/\mathrm{A}^-) + E_{00}(\mathrm{A}^*/\mathrm{A}) \tag{1.10}$$

$E^0(\mathrm{A}^+/\mathrm{A}^*)$ is the photo-oxidation potential and $E^0(\mathrm{A}^*/\mathrm{A}^-)$ is the photo-reduction potential; the convention is to write both of them as *reduction potentials*, that is with oxidated species on the left and reduced species on the right. $\mathrm{E}^0(\mathrm{A}^+/\mathrm{A})$ and $\mathrm{E}^0(\mathrm{A}/\mathrm{A}^-)$ are the ground state oxidation and reduction potential, respectively, and $\mathrm{E}_{00}(\mathrm{A}^*/\mathrm{A})$ the one-electron potential corresponding to the zero-zero spectroscopic energy of the excited state [3].

1.2 Metal complexes: photochemistry and photophysics

In contrast with closed shell organic molecules, whose ground state are always singlets, transition metal complexes exhibit a wide variety of electron configurations and spin multiplicities of ground states. Open shell systems, such as $\mathrm{Cr}^{\mathrm{III}}$ octahedral complexes, have unpaired electrons in their d orbitals, resulting in ground states with high spin multiplicity (for $\mathrm{Cr}^{\mathrm{III}}$, the ground state is a quartet); moreover, excited states can be associated with different electron configurations, and thus a wider range of excited states are available in metal complexes compared to organic molecules. Another difference between organic molecules and metal complexes arises thanks to heavy atoms effects: as previously discussed, transition metal complexes (especially second and third row) feature a high spin-orbit coupling, which increases the efficiency of intersystem crossing between excited states, making their photophysics richer and usually more complicated. Thus, phenomena requiring a change in spin multiplicity of the excited state are commonly seen in many metal complexes, such as phosphorescence or thermally activated delayed fluorescence (TADF).

As far as photochemical reactivity is concerned, metal complexes offer a wider playground to explore, as different types of transitions lead to different rearrangements of the electronic structure, thus modifying the photochemical properties of the complex. For example, transitions from bonding $\mathrm{t}_{2\mathrm{g}}$ to antibonding e_{g} orbitals are called *metal centred* transitions (MC): the population of an antibonding orbital by one electron can destabilise metal-ligand bonds, leading to a ligand substitution reaction. Besides

MC transitions, depending on their electron configuration metal complexes can undergo *charge transfer* (CT) transitions, which are divided in *metal to ligand* (MLCT) and *ligand to metal* (LMCT) transitions. The "CT" term implies that during the electronic transition an electron mostly localised on metal valence orbitals is delocalised towards ligand unoccupied orbitals for MLCT, and vice versa for LMCT. They are allowed by spin and orbital selection rules, and they feature a *radial* rearrangement of the electron density on the complex: this situation involves a transient change in the oxidation states of the ligand and the metal, and can possibly lead to intramolecular photoredox reactions. The overall reactivity depends on many different factors, such as the stability of the oxidation states of the metal and the ligands, the entity of the charge transfer and the localisation (or delocalisation) of the CT.

While being useful to gain a more clear understanding of the processes involved, it is not possible to directly predict the properties of a metal complex based on these considerations. Firstly, because these labels are only *approximations* of the observed phenomena; secondly, because the character of the electronic transitions does not allow to predict which will be the photoactive excited state. As already discussed, an excited state generated through direct photon absorption may readily decay on another one, whose character and properties may be very different. However, interpreting photochemical and photophysical properties in light of transition metal electron configuration can be helpful to understand the photoactivity of metal complexes, and to help guiding the design of new compounds. In the following paragraphs, we will try to depict the photochemistry and photophysics of some prototypical metal complexes, in view of their electron configuration, starting from the widely known Ru^{II} complexes.

1.2.1 Ru^{II} complexes

Ru^{II} has a d^6 electron configuration: in the low spin case, for octahedral coordination complexes all the electrons are paired in the t_{2g} orbitals, resulting in a singlet ground state. Polypyridyl ligands such as 2,2'-bipyridine and 1,10-phenantronline provide a ligand field strong enough to maintain the metal in the low spin configuration; the most famous example of this family of complexes is $[Ru(bpy)_3]^{2+}$. The presence of a filled set of t_{2g} orbitals on the metal and empty π^* on ligand group orbitals allows for

strong MLCT transitions, whose energy is in the visible light range thanks to the energetic positioning of these orbitals. Moreover, these are the lowest energy transitions, and so the electronic excited states associated are the lowest ones for these complexes; MLCT excited states have a geometry not very dissimilar from the ground state, since the photoexcited electron populates an empty ligand orbital, whereas MC states are more distorted, as a consequence of the occupation of an antibonding e_g orbital. In Ru^{II} complexes MLCT states exhibit longer excited state lifetimes compared to MC ones, and this is important for different applications, ranging from photocatalysis and optoelectronics: longer lifetimes allow for a higher chance for the excited state to manifest its properties. This is the reason why many Ru^{II} complexes show luminescence in solution from ^{3}MLCT states; $[Ru(bpy)_3]^{2+}$, for example, has a lifetime of 750 ns in alcoholic solutions (600 ns in water), and it has an emission centred at 620 nm [4].

The lifetime of an excited state has a crucial role also in the photochemical reactivity of the complex, since the more time is spent in the excited state, the higher are the chances for the complex to engage in energy transfer with surrounding molecules. This is a key factor when evaluating the photoactivity of the complex towards photo-oxidation and photo-reduction. Complexes in the ground state exhibit oxidation and reduction potentials, which are affected both by the metal and by the ligands used. $[Ru(bpy)_3]^{2+}$ has a ground state oxidation potential of +1.26 V and a reduction potential of −1.28 V; the ability of donating or accepting electron in the exciting state is different, since it has a different energy than the ground state. Knowing that the $E_{00}(A^*/A)$ is 2.12 eV for $[Ru(bpy)_3]^{2+}$, photoredox potentials can be estimated using equations 1.9 and 1.10: the photo-oxidation and photo-reduction potentials are −0.86 and +0.84 V respectively. The complex is both a good electron donor (photo-reductant) and electron acceptor (photo-oxidant).The thermodynamic requirements matched by the photoredox potential and the exceptionally long MLCT lifetimes make Ru^{II} polypyridyl complexes very good candidates in photocatalysis.

$$^*[Ru(bpy)_3]^{2+} + Q \longrightarrow [Ru(bpy)_3]^{3+} + Q^- \qquad \textit{oxidative quenching} \quad \{5\}$$

$$^*[Ru(bpy)_3]^{2+} + Q \longrightarrow [Ru(bpy)_3]^{+} + Q^+ \qquad \textit{reductive quenching} \quad \{6\}$$

Table 1.1: Abundance of some metal elements in Earth's crust (in mass percent); from [5]

Element	Abundance	Element	Abundance	Element	Abundance
Ru	10^{-6}	Cr	0.01	Zn	0.007
Re	10^{-7}	Mn	0.091	Zr	0.016
Os	$5 \cdot 10^{-6}$	Fe	4.7	Mo	$1.4 \cdot 10^{-4}$
Ir	10^{-7}	Co	$2.4 \cdot 10^{-3}$	Ce	0.006
Pt	10^{-6}	Ni	$7.2 \cdot 10^{-3}$	W	$1.5 \cdot 10^{-4}$
Au	$4 \cdot 10^{-7}$	Cu	0.005	U	$1.7 \cdot 10^{-4}$

1.2.2 Earth abundant metals

Among the photoactive metal complexes investigated in the recent years, the majority is made from precious metals, with low abundance on earth's crust; although many of them (such as Ru^{II} and Ir^{III}) are among the best metals for photocatalytic applications, featuring high excited states lifetimes, quantum yields and stability, it is clear that their cost and availability represents a considerable drawback for their applications on industrial scale processes. This is the reason why in the last years the attention of chemists has been focused on the more abundant first row transition metals: complexes of Cu^{I}, Fe^{II} and Cr^{III}, for example, have been studied to gain a better understanding of the factors involved in their photochemistry and photophysics. In general, the electronic configuration on the metal and the relative energetic positioning of the metal and ligand electrons are the crucial factors dictating the photochemistry of the resulting complex: it is thus reasonable to classify the photoactive metals based on their electron configuration, and understand the properties that these configurations involve.

Cr

Cr^{III} octahedral complexes feature a quartet $(t_{2g})^3$ electron configuration in the ground state, which is known for being kinetically and thermodynamically stable, and it belongs to the $^4A_{2g}$ term [6]. The first quartet excited state configuration for octahedral complexes is $(t_{2g})^2$ $(e_g)^1$: the resulting six

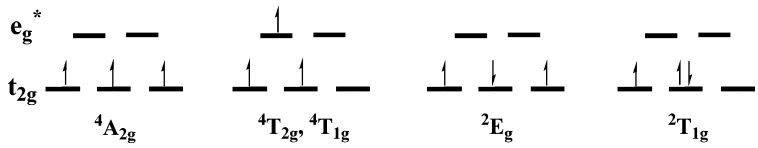

Figure 1.1: Electronic ground and excited states configurations in d^3 Cr^{III} complexes assuming O_h symmetry. From [6]

possible electron combinations yielding this configuration are subdivided into $^4T_{2g}$ and $^4T_{1g}$ terms, the former lying at lower energies than the latter. On the other hand, with sufficiently high ligand field strength on Cr^{III} ion, the lowest energy MC excited states are those associated with a doublet $(t_{2g})^3$ electron configurations, where spin pairing occurred in the t_{2g} shell; these doublet states belong to ^2E_g and $^2T_{1g}$ terms (figure 1.1). These states can be populated by ISC from the quartet excited states.

Having one electron in the e_g antibonding orbitals, the quartet excited states ($^4T_{2g}$ and $^4T_{1g}$) feature equilibrium geometries significantly distorted compared to the ground state, while lower lying doublet excited states (^2E_g and $^2T_{1g}$) feature the same electron configuration of the ground state, thus having equilibrium geometries very similar to it. This is the reason why Cr^{III} complexes exhibit long lived excited states (from nano to microseconds) and even photoluminescence: since the lowest lying excited states and the ground state have very similar geometries, non-radiative decay is significantly lowered, and phosphorescence can be observed. These luminescence properties have been widely examined and reviewed in the literature [7–11], and their photo-oxidizing properties were studied and proved to be successful in photoredox catalysis of radical cation cycloaddition [12, 13]. The very first studies on Cr^{III} octahedral complexes focused more on strong field monodentate ligands, such as CN^-; nowadays, chelating aromatic ligands with nitrogen donor atoms are among the most used and investigated, since they grant strong ligand field through σ donation and π acidity [14].

Cu

As far as Cu^I complexes are concerned, the electron configuration is d^{10}: the d orbitals are completely filled, thus providing a symmetrical

arrangement of the electrons around the metal centre. As a consequence, Cu^{I} complexes favour the tetrahedral disposition of the ligands around the metal, since it is minimises electrostatic repulsion and provides a highly symmetrical arrangement [15]. Moreover, the d^{10} configuration involves only MLCT transitions (provided that the ligands have π^{*} empty orbitals of suitable energy), while metal centred ones can not take place: thus, there are no MC excited states for Cu^{I}. In Cu^{II}, on the other hand, these states are responsible for a fast non-radiative decay of the photo-excitation, since they tend to couple with vibrational modes of the ground states (given the high difference in the two equilibrium geometries). Generally, MLCT transitions are very intense, and their corresponding excited states feature both long lifetimes (hundreds of nanoseconds) and radiative decay, which are interesting properties in photoredox catalysis and optoelectronics respectively. The majority of Cu^{I} compounds used in photoredox catalysis and for their luminescent properties is represented by α-diimine (such as phenantroline) or diphosphine complexes, or even heteroleptic complexes mixing these ligand classes [16]. The common strategy for granting long lived excited state lifetimes involves chelating the metal with bulky ligands, especially in their peripheral area, in order to restrict the planarisation in the MLCT excited state. The lability of Cu^{I} attracted the organic synthetic community [17, 18], also because it allows the Cu^{I} to bind an organic substrate and thus becoming a photoactive species [19].

Zn

Zinc is undoubtedly another interesting first row transition metal, relatively abundant on Earth's crust: however, even if Zn^{II} shares the same electron configuration as Cu^{I}, its complexes received less attention for photocatalysis mostly because the higher oxidation state of Zn^{II} involves MLCT excited states at higher energies compared to those of Cu^{I}. Zn^{II} complexes usually tend to preserve the electronic properties of the ligands bound to the metal, without adding too much complexity into their photochemistry and photophysics. Zn^{II} porphyrins are used in photocatalysis and electron transfer processes [20, 21], given the nice electron harvesting properties of these ligands, and other complexes have been explored as solid state emitters [22].

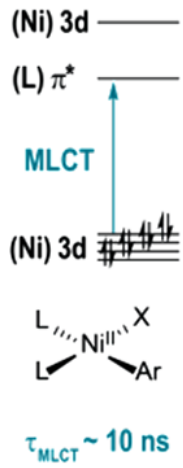

Figure 1.2: Electronic structure of d^8 Ni^{II} square planar complexes. Adapted from [23]

Ni

Nickel complexes are receiving a considerable attention concerning their photocatalytic activity. Ni^{II} compounds exhibit a d^8 electron configuration; in square planar geometry, the d orbitals splitting leaves only the $d_{x^2-y^2}$ empty and all the remaining ones filled, so that the ground state is a singlet. For sufficiently strong ligand fields, metal centred excited states have higher energies than MLCT excited states, since the empty π^* orbitals of the ligand are localised between the filled d_{xy} and the empty $d_{x^2-y^2}$ of the metal. As a consequence, square planar Ni^{II} complexes should exhibit long ^{n}MLCT lifetimes, since their deactivation through MC states is energetically not favourable (figure 1.2). A recent study confirmed this hypothesis, reporting a novel Ni^{II} square planar complex with $\tau = 4.1$ ns, whereas its tetrahedral homologue only exhibits $\tau = 60$ ps [23]. Tetrahedral Ni^0 complexes should behave similarly to the isoelectronic Cu^I compounds; however, only a few are luminescent, and only below room temperature [24].

Fe

A closer look at table 1.1 should raise the attention on Fe: it is among the most abundant metals on Earth's crust, and quite cheap compared to many other elements in that table. Iron belongs to the same group of Ru and Os, whose octahedral complexes are well known for their photoactive properties; in particular, Ru^{II} complexes are a landmark in many photo-driven applications, whether as emitters or as photocatalysts. As already highlighted, the d^6 electron configuration of Ru^{II} in octahedral complexes provides ^{3}MLCT states whose energy is lower than the metal centred states, which results in long excited state lifetimes and radiative decay of the photo-excitation. Being in the same group, Fe^{II} shares the same electron configuration; however, Fe^{II} polypyridyl complexes do not exhibit neither luminescence, nor long excited state lifetimes as the Ru^{II} ones. This is a consequence of the weaker ligand field of the first row transition metals compared to second and third row ones: the radial distribution of 3d electrons is closer to the metal core compared to 4d and 5d electrons, resulting in an intrinsically smaller ligand field. As a consequence, Fe^{II} complexes have metal centred excited states lying at lower energies compared to ^{3,5}MLCT ones, which can deactivate really fast (around 50 fs), since there is nearly no energetic barrier between MLCT and these MC states. The photoexcited electron is thus transferred to MC states, associated to high spin $(t_{2g})^5$ $(e_g)^1$ ($^3T_{1g}$ and $^3T_{2g}$) or even low spin $(t_{2g})^4$ $(e_g)^2$ ($^5T_{2g}$) configuration with highly distorted geometries compared to the ground state: non-radiative coupling through vibrations between MC and ground states is highly favoured, on a picosecond scale (figure 1.3). For $[Fe(bpy)_3]^{2+}$, the lifetime of MC excited state is $\tau = 650$ ps [25, 26], and it was exploited in photocatalysis by Gualandi et al. [27].

This electronic situation allows to tune the ligand field on Fe^{II} and make high spin complexes which can undergo light induced spin crossover (SCO): a first MLCT transition promotes one electron on the respective excited state, which deactivates to a lower ^{3}MC excited state and eventually to a ^{5}MC state, since their energy is comparable. This process has been well described [26], and many complexes with SCO properties have been studied. The versatility in coordination chemistry of Fe^{II} allows to synthesise complexes with medium and high ligand field strength on the same metal centre, providing intermediate ligand field splitting and good SCO [29].

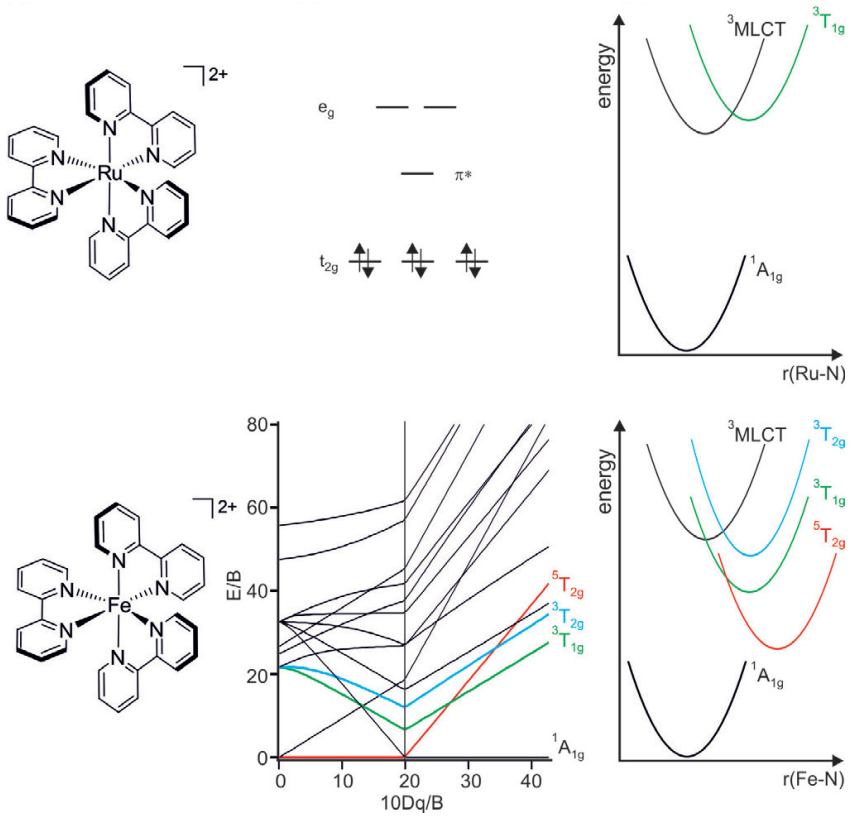

Figure 1.3: Electron configuration and potential energy diagram of the excited states for $[Ru(bpy)_3]^{2+}$ (top); Tanabe-Sugano diagram for d^6 electron configuration and potential energy diagram of the excited states for $[Fe(bpy)_3]^{2+}$ (bottom). Adapted from [28]

However, these complexes can not exhibit photoactivity, since the excited states formed have very short lifetimes.

Metal centred states on Fe^{II} have intrinsic low lifetimes, since the respective electron configurations always exhibit highly distorted geometries compared to the ground states, thus favouring non-radiative decay; to prevent crossing between MLCT and MC states on Fe^{II} complexes, it is necessary to increase the energy of MC states compared to MLCT ones. There are two possible ways to achieve this: to stabilise ^{3}MLCT (that is, decreasing their energy) and to push MC states to higher energies. This can be achieved by increasing the ligand field strength on the metal: many different strategies have been explored up to date, and all of them focus on the ligands and the coordination environment around the metal centre [28]. There are basically six key features at the core of each possible strategy for enhancing MLCT lifetimes in Fe^{II} complexes:

1. creating highly symmetric ligand fields around the metal;
2. using push-pull systems with high symmetry;
3. accessing ^{5}MLCT states through highly strained complexes;
4. enhancing ligand field strength with strong σ-donor NHC ligands;
5. cyclometalation with σ- and π-donor ligands;
6. combining σ-donation and π-acceptance with mesoionic carbene ligands.

High symmetry When the geometry around the metal centre is close to the ideal octahedron, the overlap between metal and ligand orbitals is very strong, resulting in a stronger ligand field splitting of the metal orbitals. This strategy was brilliantly applied by Jamula et al. [30]: the authors used 2,6-bis(2-carboxypyridyl)pyridine (dcpp), a tris-chelating ligand which provides a nearly perfect octahedral geometry in homoleptic complexes (figure 1.4 a). The presence of carbonyl groups between the pyridyl rings allows the ligand to adopt a sterically less constrained configuration around the metal centre compared to other polypyridyl ligands. Electrochemical measurements confirm the increase in the ligand field strength for the dcpp

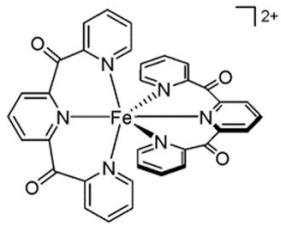

(a) High symmetry; $[Fe(dcpp)_2]^{2+}$

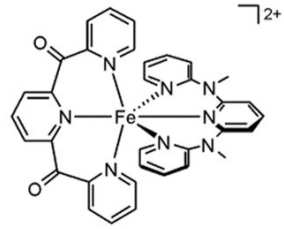

(b) Push-pull; $[Fe(dcpp)(ddpd)]^{2+}$

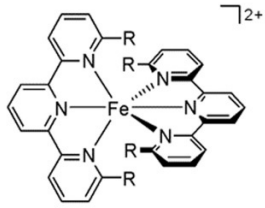

(c) High strain; $[Fe(dftpy)_2]^{2+}$ R=F

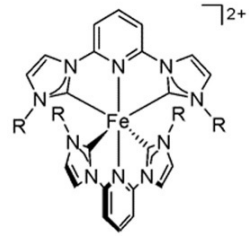

(d) NHC ligands; R=CH_3,*t*Bu,*i*Pr

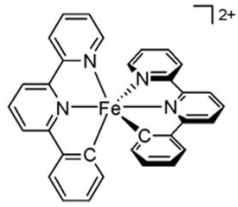

(e) Cyclometalating ligands

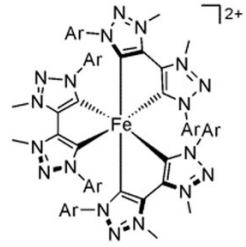

(f) Mesoionic NHC ligands; $[Fe(btz)_3]^{2+}$

Figure 1.4: Key strategies and concepts for extending MLCT lifetimes in Fe^{II} complexes. Adapted from [28]

ligand compared to bpy and terpy, since for $[Fe(dcpp)_2]^{2+}$ an oxidation potential $E_{1/2} = 1.29$ V was observed, which is higher than those reported for the bpy ($E_{1/2} = 0.66$ V) and terpy $E_{1/2} = 0.71$ V analogues. However, the complex shows excited state deactivation dynamics which are three times faster than those observed for $[Fe(bpy)_3]^{2+}$. The authors speculate that the ligand field is so strong that the lowest excited state is $^3T_{1g}$ and not $^5T_{2g}$, thus involving a higher coupling with the ground state, due to the reduced spin multiplicity of the triplet compared to the quintet.

Overall, providing a highly symmetric octahedral environment around the metal centre is generally a good option, and it is seldom employed in combination with strategies described in the next paragraphs.

Push-pull systems Push-pull complexes are systems in which there are both electron donating and withdrawing groups on the ligands bound to the metal centre: in an octahedral environment, electron donation to the metal destabilises the e_g orbitals, while electron acceptance stabilises the t_{2g} which have π symmetry. The resulting effect is the increase in energetic splitting of t_{2g} and e_g orbitals, and the destabilisation of MC excited states. Since Fe^{II} has a very versatile coordination chemistry, it is possible to synthesise heteroleptic complexes with two (or more) ligands bearing the two distinct electron donating and accepting properties. Mengel et al. [31] synthesised a complex with the dcpp ligand (as in reference [30]) and *N,N'*-dimethyl-*N,N'*-dipyridine-2-yl-pyridine-2,6-diamine (ddpd), which is a tris-chelating ligand whose pyridyl rings are bridged by $N-CH_3$ moieties (figure 1.4 b). While the carbonyl groups of dcpp provide electron accepting properties, the nitrogens on ddpd grant high electron donation. Unfortunately, picosecond MLCT excited states could not be observed for the heteroleptic complex $[Fe(dcpp)(ddpd)]^{2+}$, the observable ground state recovery being attributed to a $^3T_{1g}$ state; the authors speculate that this case is similar to the previously described one, where the ligand field is strong enough so that $^3T_{1g}$ state is lower in energy compared to $^5T_{2g}$, resulting in a faster deactivation of the photo-excitation.

Accessing ^{5}MLCT states: highly strained complexes A very different strategy stems from the results of a computational study on Ru^{II} complexes with high repulsion between ligands: the results highlighted how

interligand interaction may hinder the motions responsible for the coupling between MLCT and MC excited states [32]. Shepard et al. [33] studied strained Fe^{II} complexes with halogen substituted terpyridines (figure 1.4 c); the repulsion between ligands bound to the metal induced by the halogen atoms should be enough to force the ground state into a quintet $^5T_{2g}$, and not the singlet $^1A_{1g}$. ^{5}MLCT excited states can be directly populated by these complexes, and ^{7}MLCT can be generated through ISC. Despite showing some lability due to the high strain, the authors were able to prove that the ^{5}MLCT (or ^{7}MLCT) states deactivated with a time constant up to 14.0, 16.0 and 17.4 ps for the F, Cl and Br substituted complexes respectively. These lifetimes are nearly 360 times longer than $[Fe(bpy)_3]^{2+}$.

Enhancing ligand field strength with NHC carbenes Increasing π acidity of ligands proved to be successful in increasing the ligand field on the metal. A complementary approach is to boost σ donation, which directly increases the energy of e_g antibonding orbitals, and consequently the MC excited states. Ligands such as N-heterocyclic carbenes provide a highly directional and strong σ donation through the carbene moiety, much stronger than the usual M−N coordination bond, while giving only modest contributions to the π acidity. Luckily, NHC chemistry is versatile enough to:

- provide ligands with both carbene moieties and N coordinating sites, such as pyridines;
- allow functionalisation on the ligand backbone, such as extending the π system.

The first Fe^{II}-NHC complexes were reported by Liu et al. [34] (figure 1.4 d): electrochemical measurements proved that the σ donation of NHC is superior to the tpy, since the Fe^{III}/Fe^{II} potential for Fe^{II}-NHC complex is $300 - 400$ mV higher than for $[Fe(tpy)_3]^{2+}$. The excited state behaviour of the complex was investigated by ultrafast transient absorption (TA) spectroscopy, which revealed that the first generated ^{1}MLCT state interconverts in ^{3}MLCT in less than 100 fs, and the latter decays on MC in about 9 ps. The nature of the latter excited state has been elucidated only in another work [35], where a thorough computational characterisation of

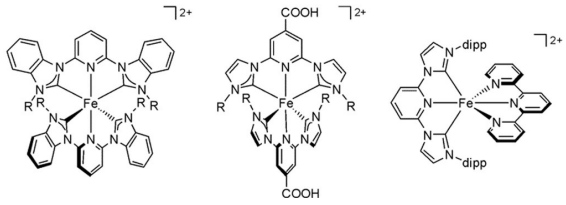

Figure 1.5: Fe^{II} complexes with NHC ligands. R=CH_3, dipp=diisopropylphenyl; adapted from [28]

the ground and excited states for the Fe^{II}-NHC complex has been carried out. Interestingly, the results suggest that the triplet ^{3}MC state is lower in energy than ^{5}MC, and that ISC between these two is not probable; on the other hand, the potential energy surface of ^{3}MLCT features a shallow minimum and a crossing point with the ^{3}MC state, confirming that the latter is populated in the deactivation pathway. This evidence marks a significant difference in the photodynamic behaviour of Fe^{II}-NHC compared to traditional polypyridyl complexes.

Giving their promising features, more NHC complexes have been studied and designed, aiming to increase even more the excited state lifetimes of ^{3}MLCT. Maintaining the $C_{(im)}-N_{(py)}-C_{(im)}$ backbone, Duchanois et al. [36] reported a NHC ligand functionalised with a carboxylic group on the pyridyl ring: the corresponding Fe^{II} complex exhibited ^{3}MLCT lifetimes of $16-18$ ps, nearly two times longer than the complex without carboxylic groups. It appears that MLCT transition in the visible range pushes electron density from the metal towards the COOH moieties: this effect was exploited to assemble a dye-sensitised solar cell, by anchoring the complex to TiO_2 support. Incident photon-to-current measurements proved that electron injection from the photoexcited Fe^{II} complex to the conduction band of TiO_2 was possible, and directly involved MLCT excited states. Further work was carried out to perfect the DSSC system, revealing that the Fe^{II}-NHC complex was able to inject electrons in TiO_2 conduction band with a 92% conversion of photons to electrons [37].

Other works presented results on carbenes featuring benzidimidazolylidene groups, which increase the π acidity of the ligand, and report even longer lifetimes (up to 26 ps) [38], raising even more interest in the research of new NHC photoactive complexes (figure 1.5). Heteroleptic complexes

containing NHC and traditional polypyridyl ligands have been characterised as well, and a correlation between the increase in number of NHC ligand around Fe^{II} and the ^{3}MLCT lifetime was found [39]. Many advances on Fe^{II}-NHC complexes have been brilliantly reviewed in the literature [40, 41].

Cyclometalation with σ- and π-donor ligands Cyclometalating ligands are another class of compounds which can provide strong ligand field on a metal centre; they stand out for the strong C−M bond, as the carbon brings a negative charge in the bonding, in contrast to carbene groups, in which the donor carbon atom are neutral (figure 1.4 e). Computational works predicted a destabilisation of ^{5}MC and a stabilisation of ^{3}MLCT states, with a little help from π donation as well [42]. Interestingly, calculations were able to predict a destabilisation of MC states only if the C atoms are placed on peripheral rings of tridentate ligand (in a C−N−C fashion), whereas the same effect is not observed for ligands with C donor atoms placed on the central ring [43]. However, studies on cyclometalated Fe^{II} are mostly limited to theoretical calculations, the experimental investigations being less advanced. It is possible that the little improvements observed with these ligands on Ru^{II} systems has lead chemists to explore other more viable routes [44, 45].

Mesoionic carbene ligands: strong σ-donation and π-acceptance Mesoionic carbene are a specific subclass of NHC which is characterised by the presence of both a positive and a negative charge on the heterocycle. Lewis structures of these compounds can be written in two mesomeric forms, where the charges are localised on different atoms. The formal negative charge on the C atom accounts for a greater σ-donation compared to normal NHC ligands, thus their Fe^{II} complexes should exhibit a stronger ligand field. The first heteroleptic complex with bpy and 4,4'-bis(1,2,3-triazol-5-ylidene) (btz) ligand was reported and characterised by Liu et al. [46] (figure 1.4 f): the ^{3}MLCT excited state showed a lifetime of 13 ps, which is about 100 times longer than in $[Fe(bpy)_3]^{2+}$. The homoleptic complex $[Fe(btz)_3]^{2+}$ was reported by Chábera et al. [47]: as expected, replacing a bpy with the mesoionic btz increased the lifetime of ^{3}MLCT state to the exceptional value of 528 ps. The latter complex was also predicted to be

a strong photo-reductant, with an oxidation potential of −1.2 V versus ferrocenium/ferrocene couple.

As far as photoluminescence is concerned, the d^5 electron configuration of Fe^{III} provided surprising and unexpected results, in contrast with the non-luminescent Fe^{II} compounds analysed so far. In particular, the homoleptic Fe^{III} complex with the mesoionic ligand btz provided superior photophysical properties compared to the Fe^{II} analogue: Mössbauer spectroscopy confirmed the *low spin* $3d^5$ configuration, associated to $^2T_2$ ground state. The absorption transitions at 528 and 558 nm are ligand to metal charge transfer transitions, leading to the corresponding ^{2}LMCT excited states: the surprising and unexpected result is the photoluminescence from these excited states, which makes $[Fe(btz)_3]^{3+}$ the first iron photoluminescent complex [48, 49]. The ^{2}LMCT decays to the ground state with $\tau = 100$ ps, and no evidence of population of MC states was found: the authors suggest that there are energetic barriers high enough to prevent the crossing between these states, and that the geometry of the ^{2}LMCT is only weakly distorted compared to the ground state.

Finally, the nanosecond range for excited state lifetimes in iron complexes has been reached by Kjær et al. [50], who synthesised a Fe^{III} complex with two scorpionate-like tris(carbene) ligands: again, the nearly perfect octahedral coordination coupled with the strong ligand field induced by the anionic ligands confers a low spin d^5 configuration. The ^{2}LMCT states exhibited a 2.2 ns lifetime, a true record for these complexes; furthermore, the same excited complex is both a strong reductant ($E_{ox} = -1.9$ V) and good oxidant ($E_{red} = 1.0$ V), thus representing a first valid alternative to Ru^{II} polypyridyl complexes even in photocatalysis.

Co

Given the same d^6 configuration, Co^{III} is a nice alternative to Fe^{II}, even if it is less abundant. Very promising and interesting results have been provided by Pal et al. [51]: the authors report two Co^{III} octahedral homoleptic complexes with strong σ-donor and electron rich tris-chelating ligands, with lifetimes of 3.21 and 5.07 ns. In this case, however, the long lived excited states are ^{3}LMCT, which turned out to be emissive in the blue visible region. The complexes proved to be very strong photo-oxidants and were used for the trifluoromethylation of polycyclic aromatic hydrocarbons;

albeit very interesting, it is worthy to note that a photosensitizing effect from the substrate was observed, since not all the tested aromatic hydrocarbon molecules were reactive.

1.3 Scope of the work

Of all the discussed Earth abundant metals, iron is the one that catches most of the attention: all the recent works published and the efforts of the scientific community in exploring the field rise interest, new ideas and questions. All the strategies proposed in the previous section for increasing MLCT excited state lifetimes of Fe^{II} complexes aim to emulate both photoluminescence and photoredox behaviour of Ru^{II} complexes; the research thus far aimed to perfect and to improve the photophysics of Fe^{II} complexes using a coordination chemistry approach. In fact, the main focus has been the increase of the ligand field on the metal centre, through accurate choice and design of the ligands; besides the studies of electron injection in TiO_2 conduction band [36], very little work has been done to examine the potential benefits of the interaction of Fe^{II} complexes with solids.

In this regard, metal-organic frameworks may provide an innovative approach for improving photophysical properties of Fe^{II} complexes. As an emerging class of optoelectronic materials, MOFs allow a flexible design of structures in which chromophore-based linkers (and even metallo-ligands, that is metal complexes with polytopic ligands) can be bound to metal nodes through coordination bonds, generating highly crystalline and even porous materials. Such MOFs could offer unique photophysics and exciton dynamics very different from those observed in stacked solid chromophore assemblies [52]. The ordered disposition of photoactive ligands can lead to a control of interchromophoric interactions, whether for boosting them or limiting them: phenomena such as aggregation-induced emission (AIE) from specifically designed ligands have been successfully transposed in the MOF world, thanks to the controlled aggregation systems provided by the latter [53]. Another important factor affecting photophysics in MOFs is the topology: chemically identical but topologically different chromophore-based MOFs may feature a non-identical concentration and orientation of the linkers in their nets, resulting in distinct photophysical properties. This

was actually observed for two Zr^{IV} with the same tetracarboxylate linker, NU-901 and NU-1000, but with different topologies. For NU-901, a direct evidence of excimer formation has been proved, while NU-1000 lacks this spectral feature. The authors were able to prove that the chromophore assembly and disposition in the two different topologies were responsible for the different photoactivity of the two materials [52].

Besides cooperation effects among chromophores and the possibility of having different orientations and dispositions in space of the photoactive ligands, metal-organic frameworks offer a rich playground of metal centres whose properties can be exploited in optoelectronics. The nature of the metal node directs not only the arrangements of the ligands in the final structure, but it also opens possibilities for photoexcited electron transfer from ligands. It has been suggested that the superior photocatalytic activity of Ti-UiO MOF analogues is provided by the good overlap of the empty *d* orbitals of Ti^{IV} with the ligand; this is possible since the energies of the orbitals involved are similar. On the other hand, Zr^{IV} and Hf^{IV} have *d* orbitals with energies too high for a good overlap with ligand orbitals, and they do not allow charge transfer from the ligand to the metal nodes [54]. In some cases, LMCT charge transfer could positively improve photoexcitation lifetime, but the effect seems to be system dependent: it is true if the acceptor states are intrinsically long lived, but if they provide non-radiative deactivation pathways (such as coupling with phonon modes), then the opposite is true.

Concerning the lifetimes of chromophores inside the MOFs, there is still not a clear vision on the key factors needed to improve them; one of the few successful results has been obtained by Luo et al. [55], who report a two orders of magnitude excited state lifetime increase of a Ru^{II} complex incorporated in a Zn-based MOF. The authors do not provide an explanation of the reasons of this outstanding lifetime increase, pointing out that the factors leading to these results are still not fully understood and harnessed. In fact, a different Ru^{II} complex has been previously incorporated into a MOF, but a shortening in excited state lifetime was reported in that case [56]. Since the emission detected by Luo et al. [55] was clearly attributed to the Ru^{II} complex and no significant shifts in UV-Vis reflectance were found, it could be speculated that here the role of the metal-organic framework is twofold: it may provide a reversible energy

transfer between MLCT states of the complex and either metal nodes or co-ligand orbitals, and it confers a structural rigidity to the metallo-ligand. The ordered arrangement of the polytopic metal complex and the local environment in the final structure may help to minimise the geometric distortions occurring during the electronic transition, thus resulting in less distorted excited states. As a consequence, their coupling with distorted MC excited states in d^6 metal complexes may suffer an increase of the energy barrier required for the inter-system crossing, since a geometrical reorganisation is disfavoured, and/or a kinetic control, due to the same reasons. On the other hand, photophysical studies on Ru^{II} complexes in rigid media, such as poly(methyl methacrylate), attribute the longer MLCT lifetimes to a "photochemical cage effect", that prevents ligand photodissociation from the accessible MC states. The main photophysical differences in solid media compared to solution ones were not ascribed neither to a stabilisation of MLCT or destabilisation of MC states, nor to a reduced energy barrier for their ISC, but mostly on the different polarisation environment and to the hindered photodissociation [57]. However, MOFs are not merely comparable to classic rigid media: the chromophores are arranged in an ordered manner, with regular orientations and definite chemical bonds within a crystalline structure. For chemically stable and non-flexible MOFs, photodissociation on the metallo-ligand is still hindered, thanks to the rigidity of the environment and the directionality of the coordination bonds. This concept has been proved by Micheroni et al. [58], who trapped a Ru^{II} polypyridyl complex into the pores of a MOF; the confined environment was able to prevent ligand photodissociation, thus hindering the non-radiative deactivation from MC states. Even Os^{II} complexes share this photochemical behaviour when confined in a MOF [59].

Within this background, we want to explore the possibility of synthesising a strong ligand field Fe^{II} complex following the guidelines depicted in the previous section, with a polytopic organic ligand, and we want to incorporate this complex as a metallo-ligand in a metal-organic framework. We believe that forming a coordination bond between the complex and another metal node can open a new way to enhance excited state lifetimes of these Fe^{II} complexes, leading to a possible new photochemistry and photophysics for this class of compounds. In the next sections we will

describe first the quest for a strong ligand field Fe^{II} complex, then the different trials we carried out for the synthesis of a MOF incorporating the chosen ligand. We provide complete information about unsuccessful and successful syntheses, as well as a critical analysis of the results, aiming to ease any further work with these kinds of systems.

Chapter 2

Tris(2-pyridyl) ligands

Tripodal ligands (also referred as tripod ligands) are facially coordinating, tridentate chelating molecules; the metal binding sites are usually nitrogen atoms on aromatic rings, such as pyrazolyl or pyridyl groups. Tris-pyridyl ligands are neutral and the pK_a of pyridine conjugate acid is 5.25, which makes these ligands better sigma donors than tris-pyrazolyl compounds (pK_a 2.48). Moreover, pyridine is a better π acceptor than pyrazole: these characteristics make tripodal pyridyl based ligands ideal for providing a strong ligand field in transition metal complexes [60].

Tris(2-pyridyl) (tp) ligands can be classified by the bridgehead atom, that is the atom connecting the three pyridyl moieties: besides carbon bridged ligands ($(py)_3C-R$), P, P=O, As, N, B, Al, Si, Sn and Ge bridged ligands can be found. Depending on the bridgehead atom, electron density on the ligand can be modulated, as well as the degree of conjugation among the pyridyl rings [61]. Carbon bridged tripodal ligands have been first synthesised with the procedure published by Wibaut et al. [62], where a lithiopyridine reacts with a dipyridyl ketone; many different compounds are reported in literature, with carbon based bridgeheads such as C−H, C−OH, $C-NH_2$, $C-OCH_3$ and C−py. One recent synthesis of 1,1,1,-tris(pyrid-2-yl)-ethane (tpe) (bridgehead group $C-CH_3$) has been proposed by Santoro et al. [63], where a monolithiated 2-ethylpyridine was reacted with 2 equivalents of 2-fluoropyridine. This synthesis provides a relatively easy way to obtain tpe ligand, and does not require any purification; the authors also report complexes of tpe with Fe^{II}, Co^{II}, Co^{III}, Cu^{II}, Pd^{II} and

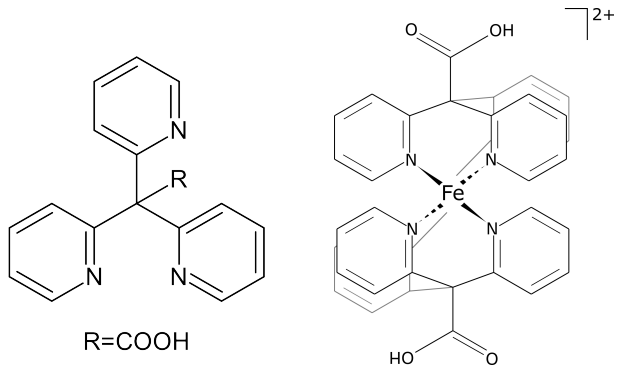

(a) 2,2,2-tris(pyridin-2-yl)acetic acid (tpa) ($C_{17}H_{13}N_3O_2$)

(b) $[Fe(tpa)_2]^{2+}$ ($FeC_{34}H_{26}N_6O_4$)

Figure 2.1: Lewis structures of tpa and its Fe^{II} complex

Ag^{I}, proving the high versatility of this ligand. Magnetic susceptibility measured at room temperature and NMR data show that complexes with Fe^{II} and Co^{III} are diamagnetic, and hence low-spin, confirming that the ligand exerts a strong ligand field on transition metals. Moreover, the coordination geometry around the metal centre is very close to octahedral, with *trans* angles of 180° and bite angles of pyridines belonging to the same ligand around 88°; Fe−N bond length are very similar, spanning only from 1.971(2) to 1.976(2) Å. Overall, both these geometric and electronic properties make tpe a strong field ligand, raising interest on the possibility of enhancing excited states lifetimes of Fe^{II} complexes.

Recently, Treiling et al. [64] synthesised a Cr^{III} complex with tpe ligand, featuring the astonishing excited state lifetime of $\tau = 4500$ µs in a $D_2O/DClO_4$ mixture, which shortens to $\tau = 2800$ µs in a $H_2O/HClO_4$ mixture. The autors attribute the increase in lifetime photoexcitation to the stronger ligand field of the facially coordinating tpe compared to other polypyridyl ligands; moreover, they suggest that the inversion centre occurring in $[Cr(tpe)_2]^{3+}$ may affect the absorption and emission properties, and that tpe ligand may also engage in ligand-based redox chemistry (ligand non-innocence).

For the scope of this work, it would be interesting to have a ligand

with the same properties of tpe, but with further functional groups on the bridgehead C atom able to coordinate other metals, such as a carboxylic group; in other words, it would be interesting to synthesise a polytopic tris-pyridyl ligand. A ligand such as 2,2,2-tris(pyridin-2-yl)acetic acid would grant the coordination of a transition metal, such as Fe^{II} (figure 2.1), through nitrogen atoms, and of other metals through the carboxylate moiety, allowing for the synthesis of supramolecular multi-metal systems. To date, polytopic ligands such as 2,2,2-tris(pyridin-2-yl)acetic acid ($C_{17}H_{13}N_3O_2$) are not reported in literature; thus, a computational study was carried out to understand if this compound could be efficiently modelled, and different synthetic routes to get this product have been attempted and described in the next sections.

2.1 Materials and methods

All calculations have been performed with Gaussian 16 software [65] at B3LYP/6-311+G(d,p) level of theory [66]; geometries were optimized to an energy minimum, and the calculated vibrational frequencies for the optimised geometries were all positive. All the reactions have been carried out in flame-dried vessels under inert N_2 atmosphere with standard Schlenck techniques. Tetrahydrofuran (THF) was distilled over Na/benzophenone; n-butyllithium (n-BuLi) solutions were titrated prior to use according to literature procedure [67]. Reactions requiring temperatures of -78 °C were cooled by an ethanol-liquid nitrogen bath, which was hosted in a small semispherical dewar suited for round bottom Schlenck flasks.

NMR spectra were recorded on a JEOL ECZR 600 spectrometer, operating at 14 T, at 25°C in an appropriate deuterated solvent; chemical shifts were referenced using the residual solvent proton resonances.

2-pyridylacetic acid hydrochloride 99% (CAS: 16179-97-8), ethyl 2-pyridylacetate 98% (CAS: 2739-98-2), n-butyllithium solution (nominal concentration: 2.5 M in hexanes, CAS: 109-72-8) diisopropylamine 99.95% (CAS: 108-18-9) and sodium sulfate 99% (CAS: 7757-82-6) were bought from Sigma-Aldrich. 2-fluoropyridine 99% (CAS: 372-48-5) was bought from Alfa Aesar. Tetrahydrofuran 99% (stabilised with 250-350 ppm BHT) was bought from Thermoscientific. TLC silica gel 60 F_{254} were bought from Merck.

2.2 Computational modelling

Optimised geometry of 2,2,2-tris(2-pyridyl)acetic acid features the three pyridyl rings arranged in a propeller-like fashion, as observed in many free scorpionate ligands; the rings are still able to rotate around the $C_{py}-C_{\alpha}$ axis, provided that the rotation of all three rings happens in the same direction, to minimise repulsion between C−H groups of different rings. Rotation of the pyridyl group allows the ligand to acquire the right conformation for the coordination of metal ions through nitrogen atoms. Calculated UV-Vis spectrum *in vacuo* shows the lowest borad transition centred at 237 nm, and a narrower one at higher energies, centred at 196 nm. Both transitions embrace different exctited states; however, while the greatest contribution to the highest energy transition is observed mostly from one state (number 47), the lowest energy transition shows equal contributions from states number 11 and 7. *Natural Transition Orbital* (NTO) analysis of these states reveals that state 7 features a transition occurring from one occupied orbital, with electron density well distributed on the whole molecule, to a virtual orbital which shows a greater contribution from two pyridyl rings and the COOH group. Contrariwise, NTOs of states 11 and 47 feature mostly a rearrangement in the electron density on the pyridyl rings during the transition (figure 2.2).

The cationic complex $[Fe(tpa)_2]^{2+}$ has been modelled as well; similarly to other tripodal ligands, the structure of tpa allows only a *fac* coordination of the metal centre. The optimised geometry is in agreement with the one of $[Fe(tpe)_2]^{2+}$ complex reported by Santoro et al. [63]: Fe−N bond distances are very similar to the experimental ones for the tpe complex, and the angles of the octahedral coordination environment are nearly identical as well. Comparisons of bond lengths and angles between the experimental tpe complex and the calculated tpa complex are reported in table 2.1; the longest Fe−N bond length was used to assign the numbering in the calculated $[Fe(tpa)_2]^{2+}$ structure, thus obtaining the numbering for the rest of the molecule according to the work of Santoro et al. [63]. These data suggest that the C−COOH bridgehead group does not alter the coordination properties of the tpa ligand compared to the tpe analogue.

Electronic spectra of $[Fe(tpa)_2]^{2+}$ have been calculated as well; as expected, new transitions arise in the complex, compared to the free ligand. A new broad transition centred at 352 nm with a shoulder at 321 nm is

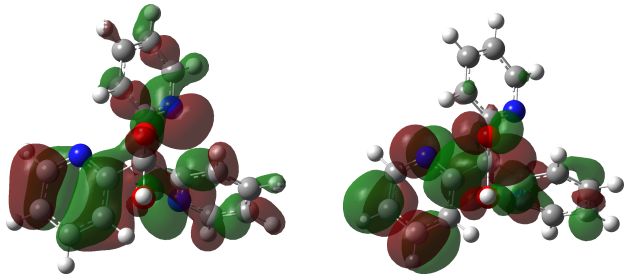

(a) State 7 - occupied

(b) State 7 - virtual

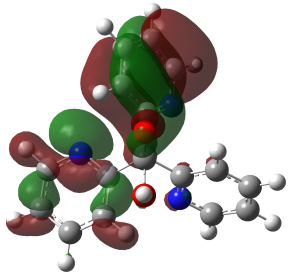

(c) State 11 - occupied

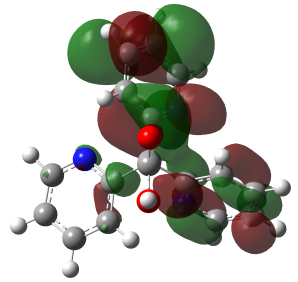

(d) State 11 - virtual

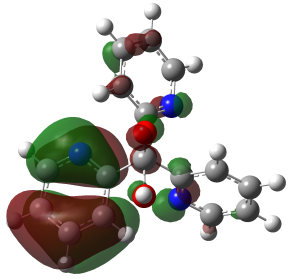

(e) State 47 - occupied

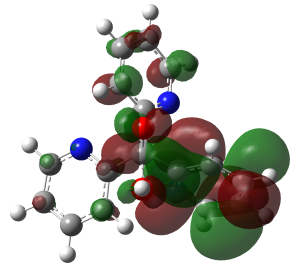

(f) State 47 - virtual

Figure 2.2: Natural transition orbitals for tpa ligand (top view)

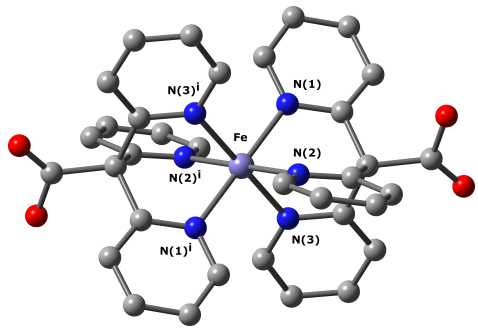

Figure 2.3: Calculated molecular structure of $[Fe(tpa)_2]^{2+}$; hydrogens have been removed, and all bonds are represented as single bonds for better clarity

Table 2.1: Bond distances (Å) and angles (°) of $[Fe(tpe)_2]^{2+}$ [63] and calculated $[Fe(tpa)_2]^{2+}$

	$[Fe(tpe)_2]^{2+}$	$[Fe(tpa)_2]^{2+}$
Fe−N(1)	1.971(2)	2.011
Fe−N(2)	1.972(2)	2.011
Fe−N(3)	1.976(2)	2.045
N(1)−Fe−N(1^i)	180	179.99
N(1)−Fe−N(2)	88.34(9)	87.79
N(1)−Fe−N(2^i)	91.66(9)	92.20
N(1)−Fe−N(3)	88.12(9)	87.47
N(1)−Fe−N(3^i)	91.88(9)	92.53
N(2)−Fe−N(2^i)	180	179.99
N(2)−Fe−N(3)	88.20(9)	92.53
N(2)−Fe−N(3^i)	91.80(9)	92.53
N(3)−Fe−N(3^i)	180	179.99

Table 2.2: Calculated absorption maxima of tpa ligand and $[Fe(tpa)_2]^{2+}$

tpa (nm)	$[Fe(tpa)_2]^{2+}$ (nm)
196	212
236	236
	321 (sh)
	352

present in the calculated spectrum of the complex, while at higher energies two transitions can be found at 236 and 212 nm, as in the free complex (see table 2.2). This behaviour is in agreement with the electron structure of a d^6 metal complex, where the highest energy transitions are mostly ligand based, and the lowest energy ones arise from the interaction of the metal orbitals with those of the ligand, thus being MLCT in nature. NTO analysis of the lowest energy transitions proved that states 7, 8, 11 and 13 are involved in the broad transition centred at 352 nm, and the contributions of the occupied orbitals are metal centred, while those of unoccupied orbitals are mostly on the ligands: the same happens for the weaker transition around 321 nm, which is generated by states 16 and 17. These results confirm that these low energy transitions are MLCT in nature, and they involve a major rearrangement of electron density from the metal towards the pyridyl ring of the ligand. Pictures of the calculated NTO can be found in section A.

It is interesting to note that the carbonyl group does not seem involved in these low energy transitions; it is thus expected that deprotonation of the COOH would not result in a dramatic colour change of the complex. It could be speculated that there are two reasons why the carbonyl group is not significantly involved in these transitions: first, the orientation of the pyridine rings after the coordination to the metal centre prevents the overlap between pyridyl and carboxyl group orbitals. Second, the C bridgehead atom may not provide enough conjugation among pyridine rings and the carboxyl group, thus limiting the electronic effects of metal coordination to the pyridyl rings.

2.3 Synthesis of 2,2,2-tris(2-pyridyl)acetic acid

The synthesis of the ligand was designed based on literature syntheses of other tris-pyridyl compounds: the main strategy is metalation of an alkylpyridine, followed by reaction with a 2-substituted pyridine. For example, literature syntheses of 1,1,1-tris(2-pyridyl)ethane involves the reaction of 2-ethylpyridine with only 1 equivalent of n-buthyllithium at −78 °C, followed by addition of 2 equivalents of 2-fluoropyridine at −30/−40°C as the coupling partner [63, 64]. It is argued that the release of F^- by the first equivalent of 2-fluoropyridine reacted with the lithiated substrate is responsible for the deprotonation of the intermediate 1,1-bis(2-pyridyl)ethane, which undergoes the second addition of 2-fluoropyridine to yield the desired product.

To synthesise the new ligand, 2-pyridylacetic acid hydrochloride has been selected as starting material; 3 equivalents of n-BuLi are necessary to neutralize the hydrochloride, the carboxylic acid proton and the proton on Cα. Thus, to a suspension of 1 equivalent of 2-pyridylacetic acid hydrochloride (175.3 mg, 1 mmol) in dry THF (15 mL), 3 equivalents of n-BuLi were added dropwise at −78 °C while stirring. After 1 hour, the temperature was adjusted at −30 °C and 2-fluoropyridine (173 µL, 2 mmol) was added dropwise though a syringe. After 1 hour, the reaction was left to reach room temperature and heated to reflux overnight. The reaction was quenched with THF, and then all the solvent was evaporated under vacuum. The resulting yellow solid was dissolved in the minimum amount of water, and acidified at pH 7 with HCl 1 M. Through slow evaporation, this solution yielded big colourless crystals, suitable for SC-XRD measurements. The obtained product is a 1D Li coordination polymer of 2-pyridylacetate, whose formula is $[Li(H_2O)]_3(2-pyridylacetate)_2Cl$ (compound **1**, figure A.7, section A). The asymmetric unit of this product contains two 2-pyridylacetate ions, one of which coordinates two Li^+ on the oxygen atoms of the carboxylate in a *syn,anti* mode, while the other one only chelates one Li^+ between the O of the carboxylate and N of they pyridyl ring. The three water molecules in the asymmetric unit bridge different Li^+ ions, and one Cl^- balances the total charge. Expanding the structure allows to understand the connectivity of the 1D Li polymer: it has a rod-like structure, where the unidimensional connection is granted by bonds between Li^+ ions and oxygen atoms of carboxylates and water molecules both. The pyridyl groups

point outwards the resulting rod, and the chlorides are aligned in a row, separating each rod from another. Overall, this coordination polymer was the only isolated product from this synthesis, and it is thus reasonable to assume that the reaction between 2-pyridylacetic acid and 2-fluoropyridine did not take place.

A different synthetic procedure was adopted, involving the use of ethyl 2-pyridylacetate as precursor and lithium diisopropylamide (LDA) as deprotonating agent: the ester is liquid, and can be better dissolved in THF, while the use of LDA prevents nucleophilic addition on the carbonyl moiety during the deprotonation step. The setup was optimised as follows: LDA was prepared by slowly adding to a small excess of diisopropylamine in anhydrous THF the n-BuLi solution at 0 °C, under inert atmosphere; the resulting mixture was stirred for 30 minutes. Then, the reaction was brought to −80 °C with the cooling bath, and ethyl 2-pyridylacetate was slowly added though a syringe and left to react under stirring for 2 h at −80 °C. The reaction was then allowed to reach −40 °C and 2-fluoropyridine was slowly added to the mixture, which was left to react for 2 h under stirring. The reaction mixture was then left to reach room temperature and quenched with brine (10%); the organic layer was separated from the aqueous one, and evaporated under vacuum. The resulting brown oil was tested by TLC, using a petroleum ether/ethyl acetate mixture (98% in petroleum ether): one product was found running on the TLC plate, with a R_f=0.15; moreover, TLC allowed to assess that the reagents used are not present in the raw product.

The product was then purified by flash column chromatography, and dried at the rotary evaporator. The resulting colourless oil was analysed through ^{1}H-NMR spectroscopy, using $CDCl_3$ as solvent. The isolated molecule features the following signals and integrations: ^{1}H-NMR ($CDCl_3$): δ 1.3 (d, 12 H), 4.3 (septet, 2 H), 6.4 (t, 1 H), 6.5 (d, 1 H), 7.3 (t, 1 H), 8.1 (d, 1 H). The spectrum can be found in figure A.8 in section A. The combination of doublet at 1.3 ppm integrating 12 and of a septet at 4.3 ppm with total integration of 2 indicates that the isolated product has two isopropyl groups; the shift of the septet suggests that the C−H is bound to a nitrogen atom. All the other signals feature an integration of 1, and their shifts correspond with those of aromatic protons of a 2-substituted pyridine.

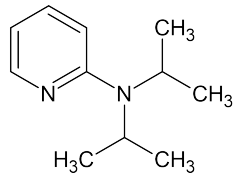

Figure 2.4: Lewis structure of 2-(diisopropyl)pyridine

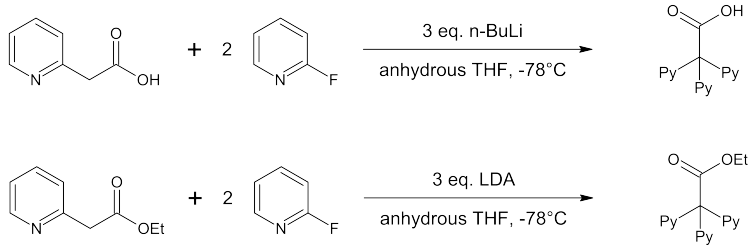

Figure 2.5: Two synthetic routes for 2,2,2-tris(pyridin-2-yl)acetic acid

Interpretation of NMR data allows to assess that the isolated molecule is 2-(diisopropylamino)pyridine (figure 2.4): instead of the desired reaction between ethyl 2-pyridylacetate and 2-fluoropyridine, an aromatic nucleophilic substitution occurred on the 2-fluoropyridine, yielding the 2-(diisopropylamino)pyridine. It could be speculated that ethyl 2-pyridylacetate and 2-pyridylacetic acid are not easily deprotonated on the C_α, and are thus not suitable for a coupling reaction with 2-fluoropyridine.

Literature studies on enantioselective direct alkylation of arylacetic acids with chiral lithium amides suggest that the low reactivity of 2-pyridylacetic acid compared to 3-pyridylacetic acid may be due to the presence of an enamide resonance structure of the deprotonated substrate, which hinders the normal reactivity as enediolate [68]. This is a direct consequence of the 2-substitution on the pyridyl ring (figure 2.6). This effect should be seen also on any ester of 2-pyridylacetic acid as well. Overall, even if different deprotonating agent ratios and more reactive coupling partners (such as alkyl iodides) are used, it does not seem possible to efficiently synthesise the 2,2,2-tris(2-pyridyl)acetic acid in high yield through the proposed pathways.

It was thus clear that a change in the ligand studied was required. The next sections will focus on another class of promising ligands, able to

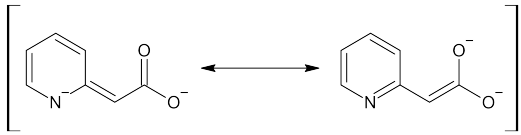

Figure 2.6: Resonance structures of hypothetical reaction intermediate of α deprotonated 2-pyridylacetate

exert a strong ligand field on metal complexes and to provide octahedral coordination geometries, as well as good π acidity: N-heterocyclic carbene (NHC) ligands.

Chapter 3

Fe-carbene complex

3.1 Materials and methods

Single crystal data have been collected on a Gemini R Ultra diffractometer equipped with a nitrogen Oxford Diffraction CryojetHT device (Agilent Technologies UK Ltd. , Oxford, U.K.) using graphite-monochromatic Mo(Kα) radiation (λ=0.71073 Å) with the ω-scan method. CrysAlisPro software (CrysAlis PRO 1.171.38.46 (Rigaku OD, 2015) has been used for retrieving cell parameters, for performing data reduction and for absorption correction (with multi-scan technique). All structures were solved by direct methods using ShelXS-14 [69] and refined with full-matrix least-squares on F^2 using the SHELXL-14 [70] in $Olex^2$ program [71]. All non-hydrogen atoms have been anisotropically refined. Hydrogen atoms have been calculated and riding on the corresponding atom.

FT-Raman spectra were acquired with a Bruker Vertex 70 spectrometer, equipped with the RAMII accessory, by exciting with a 1064 nm laser, with a resolution of 4 cm^{-1} and 300 scans. Attenuated Total Reflectance (ATR) spectra were recorded in the 4000–370 cm^{-1} range using a Bruker Vertex 70 spectrophotometer, equipped with a Harrick MVP2 ATR cell and DTGS detectors with KBr beamsplitters. The adopted resolution was equal to 4 cm^{-1}, the number of scan per sample was 36.

Calculations have been performed both with Gaussian 16 [65] for DFT and TD-DFT modelling, with GFN2-xTB [72, 73] for semi-empirical modelling of the ground state, and with the sTDA procedure for semi-empirical

modelling of excited states [74]. DFT and TD-DFT calculations have been performed with B3LYP functional [66] and 6-311+G(d,p) basis set, and with TPSSh functional [75]. Crystal structures solved from SC-XRD were used as input structures for the calculations; geometry optimization minima were assessed by checking that all vibrational frequencies for the optimised geometries were positive.

UV-Vis measurements in liquid phase were performed on a Cary 5000 spectrometer; diffuse reflectance (DR) UV-Vis-NIR solid state measurements were performed on a Cary 5000 spectrometer equipped with a reflectance sphere. Steady-state emission spectra were recorded with a Fluoromax-P-spectrometer from HORIBA Jobin Yvon IBH by using fluorescence acquisition mode.

1-methylimidazole 99% (CAS: $616-47-7$) and 2,6-dibromopyridyl-4-carboxylic acid 98% (CAS: $2016-99-1$) were bought from Fluorochem; potassium hexafluorophosphate 98% (CAS: $17084-13-8$), $FeCl_2$ anhydrous 99.5% (CAS: $7758-94-3$) and anhydrous DMF (CAS: $68-12-2$) were bought from Alfa Aesar; potassium *tert*-butoxide $\geq$ 98% (CAS: $865-47-4$) and nitric acid $\geq$ 65% (CAS: $7697-37-2$) were bought from Merck; diethyl ether (CAS: $60-29-7$) was bought from VWR.

3.2 Synthesis and characterisation

2,6-bis(3-methylimidazolium-1-yl)pyridine-4-carboxylic acid bis-hexafluorophosphate (**2**) and the Fe^{II} bis-chelated complex (**3**) (figure 3.1) were synthesized according to the literature procedure described by Duchanois et al. [36]

3.2.1 Synthesis of ligand 2

2,6-dibromopyridyl-4-carboxylic acid (0.35 mg, 1.24 mmol) was dissolved and refluxed in 1 mL of 1-methylimidazole, the latter acting both as reagent and solvent. The reaction mixture was left to reflux overnight, then cooled down to room temperature. The solid product was then directly washed three times with 5 mL Et_2O, and sonicated to ensure a thorough washing of the product; the yellowish solution was discarded, while the remaining brown paste is dissolved in the minimum amount of water. A

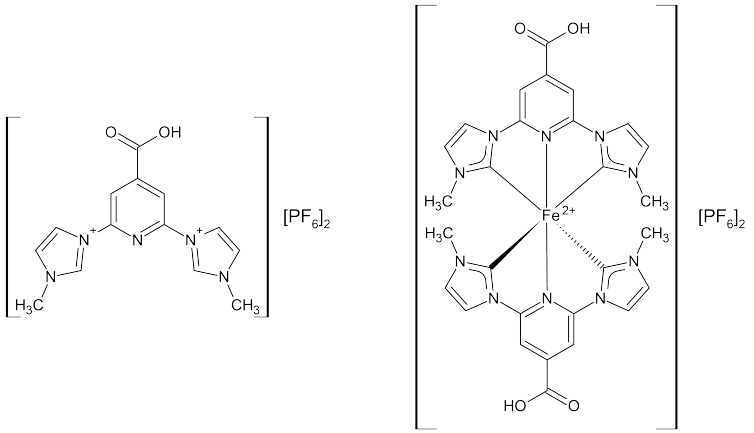

Figure 3.1: Structure of ligand **2** (left) and complex **3** (right)

saturated aqueous solution of KPF_6 (around 10 mL) was added, and the solution was acidified to pH 2 with HNO_3 1 M: a light brown product started to form and precipitate. It was then collected by filtration, washed with water, Et_2O and then left to dry ($C_{14}H_{15}N_5O_2P_2F_{12}$, yield: 83%). The synthesis was successfully scaled up to 1 g of reagent.

3.2.2 Synthesis of complex 3

The synthesis is carried out with standard Schlenck techniques, under N_2 atmosphere, with flame-dried glassware. In a 25 mL round bottom flask, anhydrous $FeCl_2$ (22 mg, 0.175 mmol) and ligand **2** (200 mg, 0.35 mmol) were dissolved in 3 mL of anhydrous DMF. Under continuous stirring, KO*t*Bu (200 mg, 1.78 mmol) was added, and the resulting dark brown suspension stirred at room temperature for 10 min. Then, the flask was transferred in an ice bath and the reaction mixture was acidified to pH 2 with HNO_3 1 M: the solution turned wine-red. After the addition of 10 mL KPF_6 saturated aqueous solution, a deep purple precipitate started to form over several minutes. The product was filtered, washed with ice cold water and with Et_2O, and left to dry ($FeC_{28}H_{26}N_{10}O_4P_2F_{12}$, yield: 46%). The synthesis was successfully scaled up to 100 mg of $FeCl_2$ reagent.

3.2.3 Crystal structures

The cationic part of ligand **2** will be referred as $[H_3L]^{2+}$, so that ligand **2** can be referred as $[H_3L][PF_6]_2$; it is soluble in organic solvent such as dimethylformamide and acetonitrile, slightly soluble in water and in hot ethanol. Small needle shaped crystals could be obtained from hot ethanol by slow cooling of the solution, and from acetonitrile by slow evaporation. Interestingly, the two sets of crystals yielded two different structures. The crystal structure obtained from hot ethanol belongs to $P\,\overline{1}$ space group and it features an asymmetric unit with one water molecule, 1.5 hexafluorophosphate ions and 0.5 hydrogen atoms on the carboxylic group. These partial occupations within the unit are in agreement with the charge balance of the ligand: the two imidazole rings on the molecule yield a charge of +2, which is balanced by −0.5 of the carboxylic group (having only half a hydrogen) and by −1.5 of the hexafluorophosphate ions. By expanding the asymmetric unit, an adduct between two ligand molecules can be observed (figure 3.2 a and b): the two molecules share an hydrogen atom on the carboxylic groups, taking a head-head arrangement. As expected, the experimental C=O distance (1.21 Å) is shorter than the C−O (1.28 Å), while the distance between two oxygen atoms sharing the hydrogen is 2.40 Å. We can thus give this compound **4** the formula $[H_3L][H_2L](H_2O)_2[PF_6]_3$. Crystals obtained from acetonitrile solutions have a different structure: it belongs to the $P\,\overline{1}$ space group and the asymmetric unit contains two ligand molecules, both protonated on the carboxylic group, two hexafluorophosphate ions and two nitrate ions (figure 3.2 c). This compound **5** has the formula $[H_3L][NO_3][PF_6]$. The presence of nitrates is clearly a consequence of the workup used for the precipitation of the ligand, since diluted HNO_3 was used to ensure protonation of the carboxylic group; the nitrates are arranged on the same plane drawn by the ligand molecules, and they interact with the latter by hydrogen bonding.

Complex **3** is highly soluble in water, acetone, methanol, acetonitrile and DMF; we can attribute to that compound the formula $[Fe(HL)_2][PF_6]_2$. While single crystals of complex **3** could not be obtained, crystals of the deprotonated complex were accidentally obtained while testing the stability of the complex in solvothermal conditions, from DMF solutions in autoclave at 120°C. The crystal structure belongs to the $C2/m$ space group; the asymmetric unit contains one single molecule of Fe^{II}-carbene complex,

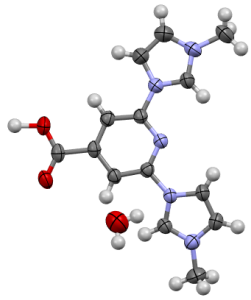

(a) Asymmetric unit

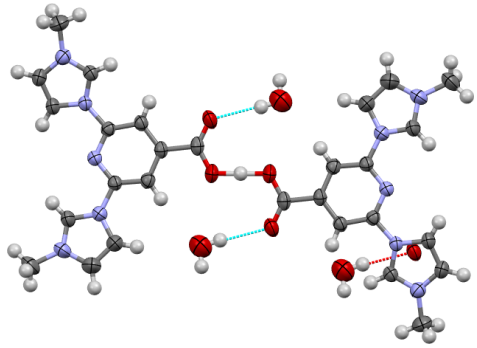

(b) Adduct between two ligand molecules

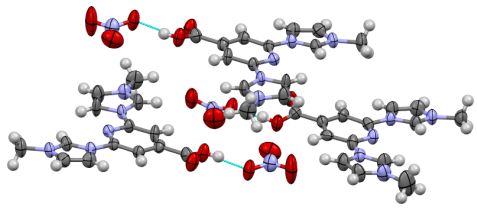

(c) Adducts between ligand molecules and nitrates

Figure 3.2: Crystal structures of ligand **2** obtained from ethanol (a,b) and acetonitrile (c); hexafluorophosphate ions are omitted

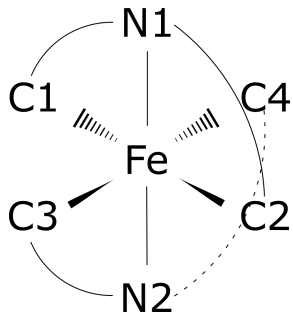

Figure 3.3: Octahedral environment around Fe^{II} in complex **6**; C1, N1 and C2 belong to one ligand, while C3, N2 and C4 to the other one. The ligands bind the complex in *mer* mode.

formed by two organic ligands binding the Fe^{II} on the nitrogen of the pyridyl group and on two carbene moieties of the imidazole rings, which have been formed through deprotonation of the C−H by KOtBu. In the crystal structure, the protons on both carboxylic groups are absent, and the formula can be written as FeL_2 (compound **6**): this could be the result of the deprotonation of the dimethylamine formed as degradation product of DMF in solvothermal conditions. Being deprotonated both on the two C (carbene) and O (carboxylic) atoms, each ligand has locally a -1 charge, which nullifies the $+2$ charge of the Fe^{II}: thus, the complex crystallised in this form is neutral. The structure has been reported in figure 3.4. The local geometry around Fe^{II} is a slightly distorted octahedron: given the structure of the ligand, the only possible isomer is *mer*, since all the three binding sites of the ligand lay on the same plane (figure 3.3). As a result, the shape of the complex resembles a cardan joint, the ligand planes being perpendicular to each other. A few selected bond distances and angles describing the octahedral geometry around the metal centre are collected in table 3.1.

The distances between the metal centre and the binding atoms are nearly the same, except one Fe−N distance which is shorter than the others. As far as angles are concerned, the N−Fe−N bond angle is nearly close to the ideal 180° angle of the octahedral geometry, while bond angles between N−Fe−C of the same ligand have values shorter than the ideal 90°. This is a result of the small bite angle of the organic ligand; on the other hand,

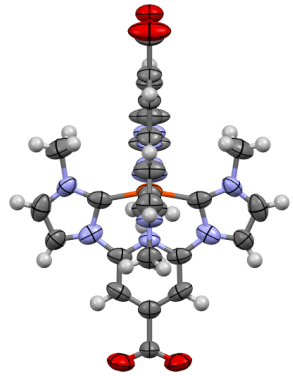

Figure 3.4: Structure of complex **6**; view along axis *a*

Table 3.1: Experimental (for compound **6**) and calculated (for compound **3**) distances and angles

Distance	Experimental (Å)	GFN2-xTB (Å)	B3LYP (Å)
Fe-N1	1.936(9)	2.64	1.95
Fe-N2	1.888(8)	2.64	1.95
Fe-C1	1.940(9)	2.61	2.01
Fe-C2	1.940(9)	2.61	2.01
Fe-C3	1.937(11)	2.61	2.01
Fe-C4	1.933(12)	2.60	2.01

Angle	Experimental	GFN2-xTB	B3LYP
N1-Fe-N2	179.2(4)°	178.18°	179.00°
N1-Fe-C1	79.5(3)°	63.52°	78.96°
N1-Fe-C2	79.5(3)°	63.84°	78.99°
C2-Fe-C4	92.5(2)°	101.39°	92.06°
C1-Fe-C3	91.4(2)°	101.70°	92.18°

Table 3.2: Lowest energy transition maximum of ligand **2** in different solvents

Solvent	λ_{max} (nm)
H_2O	291
CH_3CN	299
HCl 1 M	299
NaOH 1 M	331

C−Fe−C bond angle values for C atoms on different ligands are around 90°.

Geometry optimisation with B3LYP functional was carried out on the protonated complex **3**, $[Fe(HL)_2]^{2+}$ yielded both bond distances and angles very similar to the experimental ones, as can be seen in table 3.1. On the other hand, semi-empirical GFN2-xTB method predicted bond distance values longer than the experimental ones, smaller bite angles for the ligand and broader C−Fe−C angles within the octahedral coordination geometry.

3.2.4 Electronic characterisation

UV-Vis electronic solution spectra of compound **2** have been recorded in water, acetonitrile, HCl 1 M and NaOH 1 M. Molar concentration of the ligand was $2.0 \cdot 10^{-5}$ M; spectra are reported in figure 3.5. Depending on the solvent used, the lowest energy absorption bands of the ligand shift slightly; the maxima of the lowest energy transition are reported in table 3.2. In acetonitrile, the compound absorbs UV light up to 260 nm: the broad absorption features two shoulders at 212 and 244 nm. The lowest absorption band is well resolved and weaker compared to the other ones, and it is centred at 300 nm. The spectrum recorded in water yields the same absorption profile in the UV range, but the lowest energy band is slightly blueshifted, showing its maximum at 291 nm. On the other hand, the same band is unaltered in the spectrum recorded in HCl 1 M, which is superimposable to the one in acetonitrile. This suggests that the lowest energy band is sensitive to solvent, but also to the degree of deprotonation of the carboxylic group of the ligand. In fact, the spectrum recorded in NaOH shows a significant redshift of that band, which is centred at 331 nm.

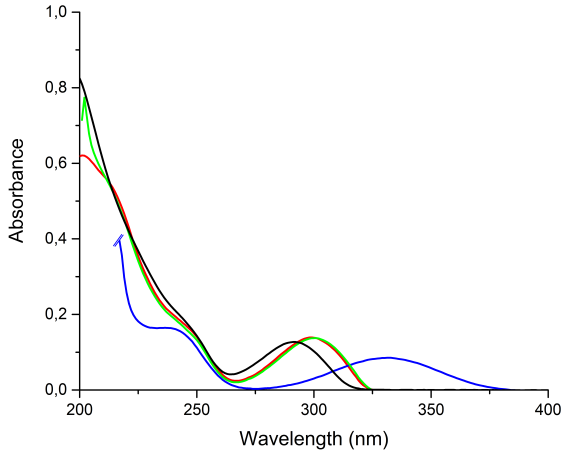

(a) Spectra in water (black), acetonitrile (red), HCl 1 M (green) and NaOH 1M (blue)

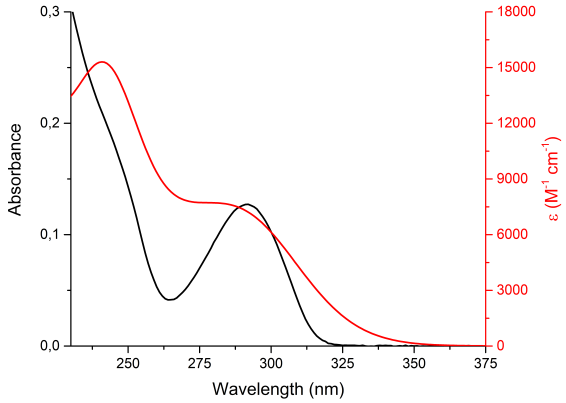

(b) Experimental (black) and calculated (red) spectra in water

Figure 3.5: UV-Vis absorption spectra of ligand **2**

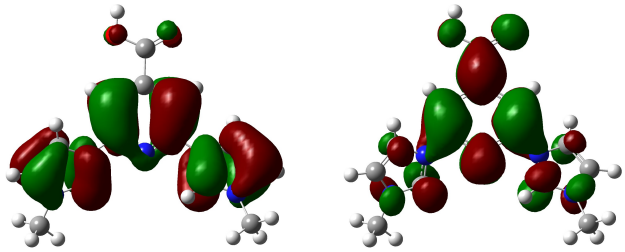

(a) HOMO **(b)** LUMO

Figure 3.6: Molecular orbitals of ligand **2** involved in the lowest energy electronic transition

Electronic spectra have been calculated as well with TD-DFT on a previously optimised geometry, using the B3LYP functional and simulating the solvent with the PCM (polarised continuum model). A total of 12 excited states have been calculated, 6 singlets and 6 triplets. As can be seen in figure 3.5, calculated spectra in water matches with the experimental one, the lowest energy transition being calculated with high accuracy. To gain further insights on the orbitals involved in this transition, a *Natural Transition Orbital* (NTO) analysis of the ligand orbitals was performed. The orbitals involved in the transition are the HOMO and LUMO of the ligand, as can be seen in figure 3.6. The contribution of the carboxylic group orbitals to the NTO is smaller for the HOMO and higher for the LUMO. Furthermore, the HOMO-LUMO transition involves a significant rearrangement of electron density on the ligands: the contribution of the orbitals on the imidazole rings in the HOMO is higher than in the LUMO, while the opposite is true for the carboxylic group. Thus, during the transition the electron density is rearranged from the imidazole rings to the central pyridyl ring and the carboxylic group.

The deprotonated ligand has been modelled at the same level of theory in water, so that comparison with the experimental spectrum of the ligand in NaOH 1 M could be made. The HOMO-LUMO transition is calculated at 272 nm (figure 3.7), and it is blueshifted compared to the experimental one recorded in alkaline environment reported in table 3.2, while the UV transition is calculated with high accuracy at 241 nm. Since the spectrum recorded in HCl 1 M should correspond to the organic ligand protonated

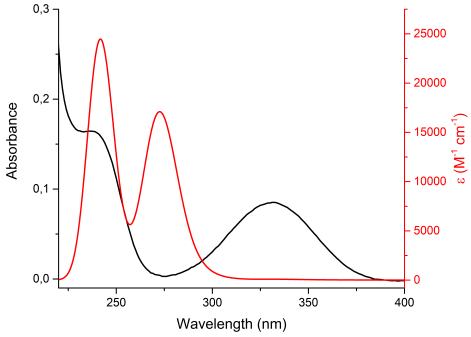

(a) Ligand in basic solution (black) and calculated organic anion (red)

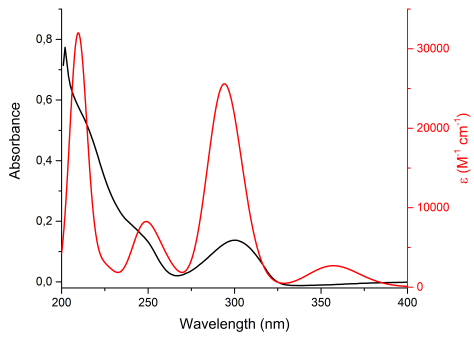

(b) Ligand in acidic solution (black) and calculated organic cation (red)

Figure 3.7: Experimental and calculated spectra of deprotonated and protonated ligand in water

on the nitrogen atom of the pyridyl group, the pyridynium ion of ligand **2** has been modelled as well. The calculated spectrum in water features the band at 299 nm, which is found in the experimental spectrum in HCl 1 M as well. On the other hand, the computation predicts a low energy band at 357 nm, which is absent in the experimental spectrum.

Electronic spectra of complex **3** have been measured at low concentration ($2.0 \cdot 10^{-5}$ M) in water, methanol, acetonitrile, HCl 1 M and NaOH 1 M (figure 3.8). Taking the spectrum in acetonitrile as reference, three main absorption bands can be observed, whose maxima can be found at 302, 397 and 521 nm. The lowest energy band can be described as a MLCT transition, from the Fe^{II} t_{2g} to the empty ligand orbitals: thus, it is a transition that involves a huge rearrangement of valence electrons in the complex. Moreover, this band is quite sensitive to solvent and pH, as summarised in table 3.3: in methanol it lowers at 507 nm, while in water at 496 nm. In NaOH 1 M the maximum can be found at 497 nm, while in HCl 1 M at 524 nm. These behaviours suggest that the rearrangement of electron density during the transition involves molecular orbital of the ligand with a significant contribution from the carboxylic group, since deprotonation of the latter involves a blueshift of the band. It could be also argued that the orientation of solvent molecules around the carboxylic group (for example, through hydrogen bonding) could also be responsible

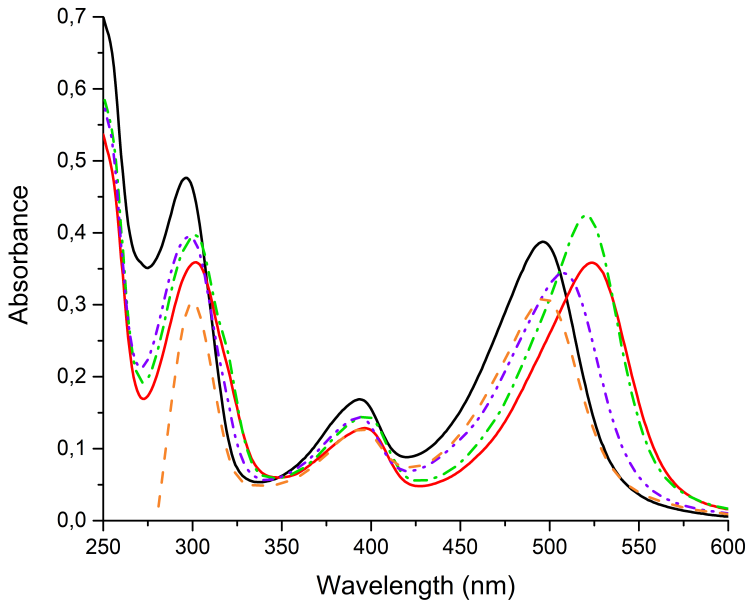

Figure 3.8: UV-Vis absorption spectra of complex **3** in water (black), acetonitrile (green), methanol (purple) HCl 1 M (red) and NaOH 1 M (orange)

for a shift of that transition. However, only the lowest energy transition is affected by solvent and pH, the other absorption bands being mostly unaffected by the different experimental conditions explored.

Fluorescence measurements have been carried out on Fe^{II} complex solutions in acetonitrile and HCl 1 M, by exciting the samples at 302, 397 and 521 nm (524 for HCl 1 M); no emission was detected from the samples.

Electronic spectra of the complex have been calculated as well, simulating the solvent with PCM model for TD-DFT calculations and with ALPB (analytical linearized Poisson-Boltzmann) model for the semi-empirical STDA method. The latter models with high accuracy the high energy transitions, while fails to reproduce the low energy bands of the complex, as can be seen in table 3.4; it also underestimates the absorption coefficient of the transition at 400 nm and it predicts a low energy band which is totally absent in the experimental spectrum. These results could be a consequence of the low accuracy of geometry optimization through the semi-empirical method, which results in a poor accuracy on the calculated

Table 3.3: Lowest energy transition maximum of complex **3** in different solvents

Solvent	λ_{max} (nm)
H_2O	496
CH_3CN	521
CH_3OH	507
HCl 1 M	524
NaOH 1 M	497

Table 3.4: Experimental and calculated absorption maxima for complex **3** in acetonitrile

Experimental (nm)	STDA (nm)	B3LYP (nm)
302	298	269
397	400 (very weak)	354
521	487	443

electronic transitions. On the other hand, TD-DFT calculations with B3LYP functional well reproduces the absorbance pattern, but fails to calculate accurate energies for these transitions, which are all shifted to higher energies compared to experimental ones. While this functional well predicts both geometry and vibrations of the complex, it could be argued that it does not efficiently model the electronic structure of the complex, since a systematic shift in the absorbance transition has been observed.

A better modelling of complex **3** was achieved with the meta-GGA density functional TPSSh [75]. The best concordance between observed and calculated transitions have been found when comparing the spectra recorded in water and calculated in water using PCM method (figure 3.9): the experimental transitions at 296 and 394 nm have been reproduced with outstanding accuracy, while the lowest energy transition was calculated at 467 nm, around 20 nm below the experimental one (table 3.5). Calculation output highlights that the transitions centred at 299 and 385 nm are linked to two distinct states, state number 5 and 7 respectively, while transition at 299 nm is composed by three transitions close in energy, corresponding

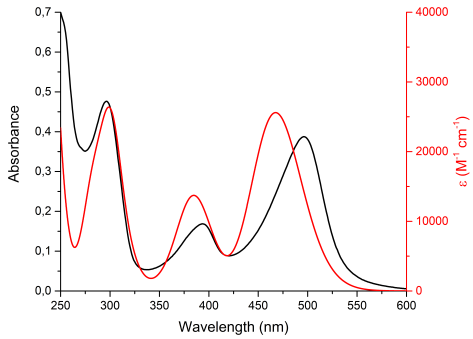

Figure 3.9: Experimental (black) and TPSSh calculated (red) spectrum of compound **3** in water

to states 31, 32 and 33, very close in energy one to another. NTO analysis for state 5 revealed the contribution of two occupied and two unoccupied (virtual) orbitals to the transition; the two occupied orbitals have strong contributions of atomic orbitals of the metal, while the two virtual ones feature major contributions from the pyridyl and −COOH group of the ligand, confirming that this transition is a metal-to-ligand. Similarly, contributions to the occupied and virtual natural transition orbital for state 7 are from the metal and the ligand respectively, suggesting that even this transition is a MLCT; on the other hand, the occupied NTO has a small ligand character, since electron density can be found mostly on the imidazole ring. It is interesting to note that this transition does not involve rearrangement of electron density on the −COOH groups of the ligand, opposed to the previous case. States 31, 32 and 33 feature different orbitals involved in their respective transitions: in these cases, there is no marked metal or ligand centred character for these orbitals, the total contributions being equally spread on the metal and on the ligands for both occupied and virtual NTOs.

Given the strong colour of the compound, a high dilution in $BaSO_4$ was necessary to record solid state diffuse reflectance spectra: 5 mg of compound were diluted in 100 mg of $BaSO_4$ (dilution factor 1 : 20). The complex starts absorbing light at around 900 nm, and the reflectance decreases significantly below 800 nm (figure 3.10). A reflectance minimum is observed at 522 nm, with two shoulders at 660 and 564 nm. Two more minima can

Table 3.5: Experimental and TPSSh calculated transition for complex **3** in water

Experimental nm	TPSSh nm
296	299
394	385
496	467

Table 3.6: Electronic transitions of complex **3** in acetonitrile and in solid state (diluted in $BaSO_4$)

CH_3CN (nm)	Solid state (nm)
302	260
397	410
521	522

be found at 410 and 260 nm. Table 3.6 compares electronic transitions in solid state and in acetonitrile.

Solid state fluorescence spectra of compound **3** excited at 260, 410 and 522 nm did not reveal any emission from the sample.

3.2.5 Vibrational characterisation

Both semi-empirical and DFT calculated IR spectra of ligand **2** are slightly shifted compared to the experimental one, and lack the wide and strong hexafluorophosphate band at 826 cm^{-1}, since the organic molecule has been modelled without the counterion. Table 3.7 collects a selection of vibrational transitions: DFT calculated vibrational spectrum matches well the multiplicity of the most intense bands, but significantly overestimates the C=O stretching. The two bands at 1625 and 1585 cm^{-1} have been calculated at 1649 and 1620 cm^{-1}, and are assigned respectively to C−C aromatic symmetric stretching on the pyridyl ring and to a composite of C−C and C−N asymmetric stretching on the imidazole ring and C−C and C−N asymmetric stretching on the pyridyl ring. The band at 1546 cm^{-1}

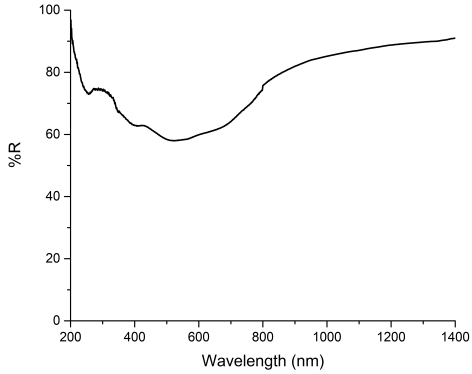

(a) Reflectance spectrum

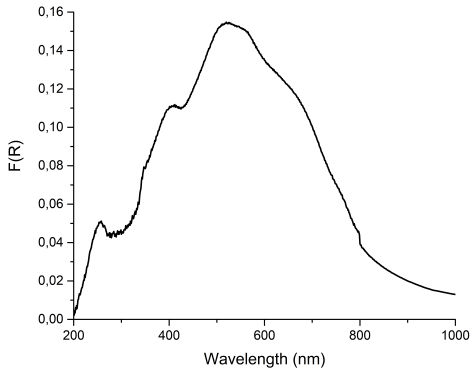

(b) Kubelka-Munk spectrum

Figure 3.10: Solid state electronic spectra of diluted complex **3**

is assigned to C−N symmetric stretching on the imidazole rings, with only small contribution from the pyridyl ring, while the band at 1446 cm^{-1} is a sum of C−H bending of methyl groups with stretching of C−C and rocking of C−H on the pyridyl ring. The two bands at 1389 and 1370 cm^{-1} are assigned to O−H bending, coupled with aromatic ring deformation, while the band at 1212 cm^{-1} is assigned to C−O stretching coupled with O−H bending and C−H aromatic scissoring.

Even if ligand **2** shows fluorescence at the infrared exciting wavelength of Raman (1064 cm^{-1}), a few vibrational transitions could be observed in the $2000 - 100$ cm^{-1} range. By comparing the experimental spectrum to the computed Raman activities, the weak band at 1728 cm^{-1} is assigned to C=O stretching; other Raman modes share the same frequencies of the IR modes discussed previously, as can be seen in table 3.7, and some modes are more active in Raman spectroscopy, such as C=N in plane bending of imidazole rings, which can be found at 1316 cm^{-1}.

IR spectrum of complex **3** shows C=O stretching band at 1694 cm^{-1}. The C=C stretching lies at 1575 cm^{-1}, while C=C and C=N combined stretching on the pyridyl ring can be found at 1545 cm^{-1}: compared to the values of the free ligand, these bands lie at lower frequencies (figure 3.12). The strong band at 1482 cm^{-1} is assigned to the C_{py}−N_{im} + C_{py}=C_{py} asymmetric stretching. O−H bending can be found at 1345 cm^{-1}; bands at 1263 and 1234 cm^{-1} are assigned to O−H and C−H aromatic bending.

As far as Raman bands are concerned, the calculation yields a theoretical band at 1814 cm^{-1}, but it appears that the C=O stretching is not active. While the free ligand shows the band of both IR and Raman modes nearly in the same position, in the Fe^{II} complex the IR spectrum has a band ascribed to that mode, but Raman spectrum does not show any presence of it in that spectral range. The band in the Raman spectrum whose frequency is closer to the calculated one for the carbonyl group is found at 1624 cm^{-1}: this band is assigned to a combined C=C stretching on the pyridyl ring and a C−H scissoring on the same ring. The group of transitions found between 1500 and 1400 cm^{-1} is assigned to vibrations involving both CH_3 bending and pyridyl ring expansion, while the vibrations associated to C_{im}−N_{im} stretching coupled with C−H rocking and with C−H scissoring on pyridyl ring are found at 1280 and 1260 cm^{-1} respectively. Finally, the three signals in the $980 - 1033$ cm^{-1} range correspond to deformation of

Table 3.7: A selection of experimental and calculated IR (top) and Raman (bottom) transitions for ligand **2**. st = stretching, b = bending, r = rocking

IR mode	Experimental (cm^{-1})	B3LYP (cm^{-1})
C=O st.	1736	1824
C=C st.	1625	1649
C=C + C=N st.	1585	1620
C=N st.	1546	1570, 1559
C−H b. + C=C st. + C−H r.	1446	1458, 1452
O−H b.	1389, 1370	1387, 1370
C−O st.	1212	1183

Raman mode	Experimental (cm^{-1})	B3LYP (cm^{-1})
C=O st.	1728	1824
C=C st.	1629	1649
C=C + C=N st.	1585	1612
C=N st.	1547	1570, 1559
C−H b. + C=C st. + C−H r.	1446	1458, 1452
O−H b.	1373, 1362	1387, 1370
C=N imidazole b.	1316	1328
Imidazole rings deformation	1020	1030
Pyridyl ring deformation	999	1012
Aromatic rings deformation	986	998

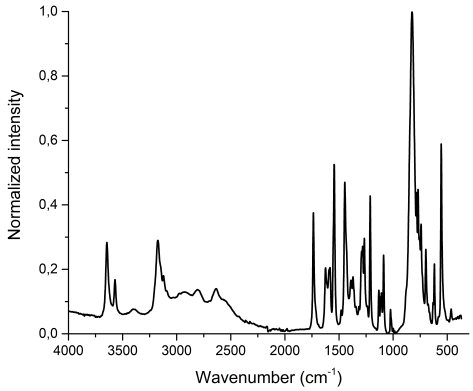

(a) FT-IR-ATR

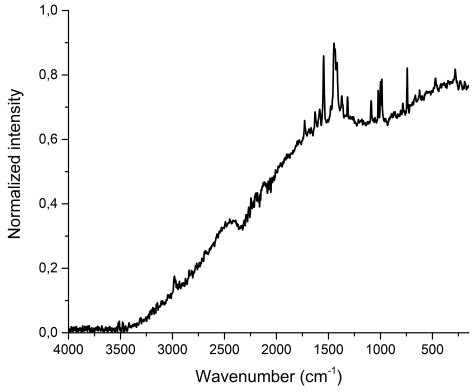

(b) Raman

Figure 3.11: Vibrational spectra of ligand **2**

Table 3.8: A selection of experimental and calculated IR (top) and Raman (bottom) transitions for complex **3**. st = stretching, b = bending, r = rocking, sc = scissoring

IR mode	Experimental (cm^{-1})	B3LYP (cm^{-1})
C=O st.	1694	1814
$C_{im}{=}C_{im}$ st.	1575	1623
$C{=}C_{py,im}$ + $C_{py}{=}N_{py}$ st.	1545	1590
$C_{py}{-}N_{im}$ + $C_{py}{=}C_{py}$ st.	1482	1498
O−H b.	1345	1355
O−H b. + C−H	1263, 1234	1187, 1154

Raman mode	Experimental (cm^{-1})	B3LYP (cm^{-1})
$C_{py}{=}C_{py}$ st. + C−H sc.	1624	1649
C−H b. + py ring expansion	1490, 1445	1462, 1427
$C_{im}{=}N_{im}$ st. + C−H r.	1280	1283, 1279
$C_{im}{=}N_{im}$ st. + C−H sc.	1260	1252, 1249
Pyridyl ring deformation	1033	1041
Imidazole rings deformation	1006	1014
Aromatic rings deformation	982	987

imidazole and pyridyl rings; compared to the free ligand, the three signal pattern is preserved, but shifted to higher wavenumbers as a result of the coordination to Fe^{II}. However, the relative order in energy is inverted: while in the free ligand the modes are assigned as simultaneous vibration of the three rings (lower), of the pyridyl (middle) and imidazole (higher) rings, in complex **3** the highest energy vibration is assigned to pyridyl ring deformation, and the middle peak corresponds to imidazole rings deformation. Selected values of IR and Raman modes are reported in table 3.8.

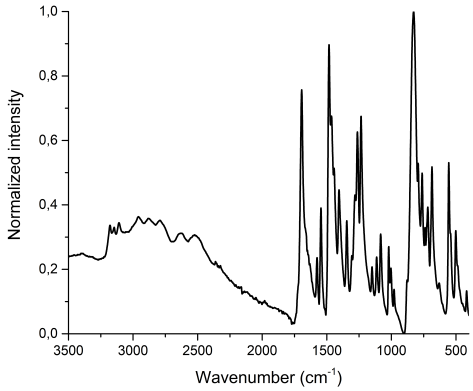

(a) FT-IR-ATR

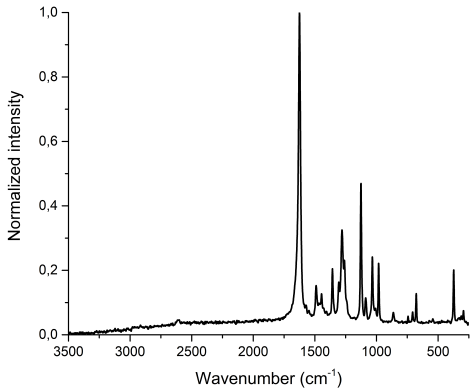

(b) Raman

Figure 3.12: Vibrational spectra of complex **3**

Chapter 4

Synthesis of metal-organic frameworks with Fe^{II} carbene complex

4.1 Zn-MOFs

Zn-MOFs based on carboxylate ligands are well known and studied in literature; their synthesis is easy and straightforward, seldom requiring an optimisation of the M:L ratios and solvent mixtures. Common solvothermal conditions are perfect for achieving crystalline materials in high yield, but sometimes even low temperature syntheses (e.g. 80°C) yield crystalline products in high quantity. Moreover, Zn-MOFs tend to give nice single crystals, allowing for good SC-XRD measurements. According to Pearson's classification of *hard/soft* acid and bases [76], Zn^{II} is considered a *soft* metal and carboxylate ligands *hard* bases, and thus the ligand in Zn^{II}-carboxylate MOFs is not as strong as, for example, in Zn^{II}-imidazolate MOFs, where the *soft-soft* interaction yields more stable materials. However, the *hard-soft* interaction in Zn^{II}-carboxylate MOFs often entails a flexibility in the framework, which could be a very interesting property for these materials: flexible frameworks can expand as a consequence of an increase of partial pressure of gases, thus enhancing gas storage capacity.

Zn^{II}-carboxylate MOFs can feature different secondary building units, and different connectivities. MOF-2 is built on dinuclear Zinc paddle wheel

clusters, $[Zn_2(-COO)_4(H_2O)_2]$: this unit is formed by two Zn^{II} ions bridged by four carboxylates [77]. Each Zn^{II} ion has a square pyramydal coordination, the basis being four oxygen atoms of four different carboxylates, while the axial ligand is a water molecule (for MOF-2). The resulting building unit leads to the formation of 2D layers; it is also possible to connect these layers and generate pillared structures, if the axial ligand of the paddle wheel is a monodentate ditopic linker such as an aromatic diamine [78]. Conversely, MOF-5 is built on octahedral $Zn_4O(-COO)_6$ secondary building units; the basic zinc acetate SBU consists of four Zn^{II} tetrahedra sharing a vertex (the oxygen atom), bridged by carboxylate moieties of 4,4'-biphenyldicarboxylic acid. All these secondary building units grant both structural and mechanical stability, since they are formed by groups with highly directional chemical bonds [79].

There are no precise synthetic techniques leading to the preferential formation of the different Zn^{II} SBUs in metal-organic frameworks, since many factors occur in determining the SBU and the structure of a MOF, from synthetic conditions to the choice of solvents and the nature of the chosen ligands. Moreover, the same reagents could yield different products: especially for Zn^{II} based MOFs, products with slightly different structures could have similar formation energies. This usually results in mixtures of more than one phase in the reaction products. The optimisation of the synthetic parameters such as M:L ratio, solvents, reaction times and temperature is thus a crucial step to push the synthesis towards the desired product, or at least to a pure phase. While most parameters need to be optimised in a trial and error fashion, some general considerations for a good synthetic starting point could be made. First, adapting the synthesis from existing recipes is a good choice, especially if the literature procedure proves the purity of the sample through p-XRD diffraction. Second, among the different synthetic methods, solvothermal syntheses give the highest yields, and could help to favour the formation of the thermodynamic product over the kinetic one [80]. Furthermore, using DMF (or DEF) as solvent (or co-solvent) allows for good solubilisation of the starting materials: while most nitrates are soluble in substituted formamides, some carboxylate ligands are insoluble even in these solvents. However, when DMF (and, to a fewer extent, DEF) is heated, it slowly starts degrading to formic acid and dimethylamine (diethylamine for DEF): the presence of a weak

base is enough to deprotonate small potions of the ligand and to form the corresponding anion, which is more soluble.

A multi-metal Zn^{II} based MOF was recently reported by Luo et al. [55]: the structure is built on 2D layers formed by $[Zn_2(-CO_2)_4]$ paddle wheel unit with 2,6-naphtalenedicarboxylate (ndc), the axial positions being occupied by two pendent pyridyl groups of a $[Ru(pytpy)_2]^{2+}$ complex (pytpy=4'-(pyridin-4-yl)2,2':6',2"-terpyridine). The metallo-ligand acts as a pillar, connecting two $[Zn_2(ndc)_2]$ layers; the spacing between layers is enough to allow for an interpenetration of the material, resulting in a 2-fold primitive cubic (**pcu**) topology.

The authors reported a Brunauer-Emmett-Teller (BET) and Langmuir area of 340.3 and 457.3 m^2g^{-1} respectively, which proved to be higher than those of previously reported MOFs with Ru^{II} complexes, usually spanning from 20 to 50 m^2g^{-1}. Overall, the synthesis of the MOF is straightforward: 0.04 mmol of $Zn(NO_3)_2 \cdot 6\,H_2O$, 0.02 mmol of Ru^{II} complex and 0.04 mmol of H_2ndc were dissolved in 4 mL of DMF/EtOH 2 : 1 v/v mixture, and placed in a 10 ml Pyrex glass vial. The reaction was heated at 120 °C for 72 h, then cooled to room temperature at a rate of 5 °C·h^{-1}.

The authors report a remarkable increase in fluorescence intensity and in the excited state lifetime of the Ru^{II} complex incorporated within the MOF compared to the free one: the values obtained are 22.09 ns for the Ru^{II}-MOF and 0.39 ns for the free complex. On the other hand, the absorption band around 500 nm is weaker in the Ru^{II}-MOF than in the Ru^{II} complex; the latter observation was not commented by the authors, but it appears to be unrelated to the photoluminescence properties.

Since this strategy proved to be successful in enhancing excited state lifetimes of a metal complex, it has been applied with the previously synthesised Fe^{II}-carbene complex. However, while the complex used by Luo et al. [55] could coordinate only through two nitrogen atoms of a pyridyl ring in a monodentate fashion, compound **3** can bind metal ions only through carboxylate groups. As a consequence, in this case the structure built on $[Zn_2(ndc)_2]$ layers connected by metal complexes can not be obtained, since the axial positions on the paddle wheel of Zn^{II} can only be capped by monodentate linkers. On the other hand, since the coordination chemistry of Zn^{II} is very versatile, different coordination environments around the metal centre could be expected, such as $Zn_4O(-COO)_6$, where carboxylate

moieties belong to both (ndc^{2-}) and complex **3**.

Another ligand employed for mixed MOF synthesis was 4,4'-stilbenedicarboxylic acid (H_2sdc): since its length (12.25 Å) is comparable to the one of the Fe^{II} complex (12.41 Å), it could be speculated that the formation of a mixed ligand metal-organic framework would be easier, leading to structures either with a regular repetition in space of the ligands or with a less defined arrangement in space.

4.1.1 Materials and methods

The syntheses were carried out either in Pyrex 30 mL vials (maximum available volume for solvothermal reactions 10 ml) or in stainless steel teflon lined Paar autoclaves (total volume 45 mL, maximum available volume for solvothermal reactions 15 mL). The general synthetic procedure adopted for the syntheses described in the next sections is straightforward: all the reagents are placed inside the reaction vial (or in the teflon vessel of the autoclave), followed by the addition of solvent and sonication for 5 minutes at room temperature. Reactions were heated at 80 °C in a laboratory oven for 72 h, unless otherwise noted, with cooling ramps of 5 $°C \cdot h^{-1}$. All products have been filtered and washed three times with fresh DMF, then left to dry in air flux.

Thermogravimetric analyses (TGA) were carried out on a AutoTGA 2950HR V5.4A instrument, heating samples at 10 $°C \cdot min^{-1}$ from 30 to 800 °C in air.

SC-XRD measurements, FT-Raman and ATR spectra, DR-UV-Vis-NIR and steady-state emission spectra were recorded with the same instrumentation of section 3.1.

X-ray powder diffraction patterns (p-XRD) were collected by a Philips X'pert PRO automatic diffractometer operating at 40 kV and 40 mA, in theta-theta configuration, secondary monochromator with Cu Kα radiation ($\lambda = 1.5418$ Å) and a Pixel solid-state detector (active length in $2\theta - 3.347°$). Data were collected from 5 to 75° 2θ with a step size of 0.026° and a time per step of 700 s at RT (total time 2 h). 1° fixed soller and divergence slits giving a constant volume of sample illumination were used.

Images of products were acquired with Leica MZ16 stereomicroscope (Leica Microsystems, Wetzlar, Germany), in reflected light mode, with D65 illumination and fiber optics placed on both sides of the samples at 45°.

Table 4.1: List of Zn−ndc−Fe MOF syntheses. Entries with * are carried out in autoclave.

Name	Solvent	Amount of product retrieved (mg)
S56	DMF/EtOH 9:1	9.5
S57	DMF/EtOH 2:1	12.1
S59*	DMF/EtOH 9:1	19.5
S062*	DMF/EtOH 9:1	20.9
S65	DMF/EtOH 9:1	6.7
S66	DMF/EtOH 9:1	13.2
S67*	DMF/EtOH 9:1	29.2
S70*	DMF/EtOH 9:1	21.1
LA87	DMF/EtOH 9:1	21.16

The morphology of sample **S81** was assessed through a scanning electron microscope operating with a field emission source (model: TESCAN S9000G; source: Schottky type FEG; resolution: 0.7 nm) at 15 keV (in In-Beam SE mode), fitted with an EDS detector (Oxford EDS Ultim Max operating with Aztec software). Before the investigations, the sample was coated with Cr in order to enhance the conductivity.

Compound **3** was synthesised as described in paragraph 3.2.2, page 41. N,N-dimethylformamide (DMF) 99% (CAS: 68-12-2) was bought from Alfa Aesar; EtOH 96% v/v (CAS: 64-17-5) and MeOH (CAS: 47-56-1) were bought from VWR chemicals; 2,6-naphtalenedicarboxylic acid (H_2ndc) 99% (CAS: 1141-38-4) was bought from Sigma Aldrich, 4,4'-stilbendicarboxylic acid (H_2sdc) 96% (CAS: 100-31-2) from Alfa Aesar.

4.1.2 Zn−ndc−Fe MOF

Syntheses were carried out with $4.5 \cdot 10^{-2}$ mmol of $Zn(NO_3)_2 \cdot 6\,H_2O$, $4.5 \cdot 10^{-2}$ mmol of H_2ndc, and $2.25 \cdot 10^{-2}$ mmol of Fe^{II} carbene complex. The overall Zn:ndc:Fe ratio is $2:2:1$, the same one used by Luo et al. [55]; synthesis S57 was carried out only with 4 mL of solvent, using the same concentrations in the aforementioned work, while for the other syntheses 10 mL of solvent were used. The list of the syntheses can be found in table 4.1.

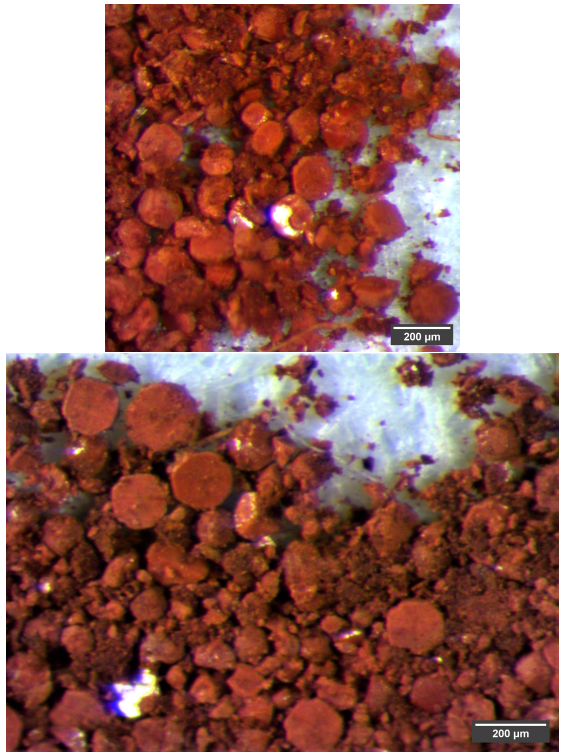

Figure 4.1: Images of S56 acquired with stereomicroscope

Synthesis S56 yielded nice and big red crystals on the vial walls, while S57 yielded only a red powder. After filtration, product S56 was observed at the stereomicroscope (figure 4.1): small red cubic shaped crystals could be found, along with red powder. However, the crystals faded very quickly outside the solvent, transitioning from bright to opaque, then cracking and eventually pulverizing. The flat faces of the aggregates in figure 4.1 were those on which the crystals started to grow on the pyrex vial walls; a few aggregates with a more cubic shape could still be observed, but they soon cracked and pulverized.

Vibrational FT-IR-ATR spectra of S56 and S57 are superimposable, meaning that the two products are identical; the coordination of the carboxylate to the Zn^{II} is responsible for the enhancement intensity of the bands in the $1540-1610$ cm^{-1} range, where asymmetric COO^- stretching bands mix

with C=C stretching of the complex, and in the $1330 - 1400$ cm^{-1} range, where the symmetric COO^- stretching lies [81]. The presence of the Fe^{II} complex is confirmed by the bands around 1480 cm^{-1}, which are not found in the 2,6-naphtalenedicarboxylate; conversely, the presence of the latter is suggested by the bands around 925 cm^{-1}. The shoulder around 1567 cm^{-1} belongs most likely to DMF, which can still be present in the final product. Raman spectra of both S56 and S57 are superimposable as well, and many bands can unambiguously be attributed to 2,6-naphatalenedicarboxylate, such as 1127, 1033 and 982 cm^{-1}. Vibrational spectra are reported in figure 4.2.

The S56 synthesis has been replicated three times, always in vial, with the same reaction conditions: all the obtained products showed the same spectroscopic behaviour. The same synthesis in autoclave with the respective replica gave constantly the same product as well. During these various trials, several single crystals suitable for SC-XRD measurements could be isolated; by keeping them in the mother solution, transferring them on a capillary tube or covering them with a drop of oil as soon as possible, the crystals did not fade. It was thus possible to carry out SC-XRD measurements at 200 K; unfortunately, every crystal analysed did not yield diffraction with sufficient intensity to collect significant data. p-XRD measurements carried out on replica LA84 evidence a low signal to noise ratio (figure 4.3); even if a few peaks can be found in the $8 - 12°$ range, the diffractogram confirms the low crystallinity of the sample after solvent loss.

TGA analysis on S66 (figure 4.4) reveals a weight loss up to 80 °C, which is water loss, and another one above 110 °C, ascribed to DMF loss. The material is quite stable up to 320 °C, then a huge weight loss is observed until 600 °C; heating in air stream above this temperature does not result in further weight loss, meaning that all the organic matter has been oxidised to CO_2, leaving only metal oxides, whose total percentage is around 20% of the analysed sample amount.

Unfortunately, surface area measurements could not provide useful data, since every attempt yielded values comparable to measurement errors; the cause is most likely the very modest sample quantities employed for the measurements. Up to now, it was not possible to upscale the synthesis and to provide meaningful surface area data.

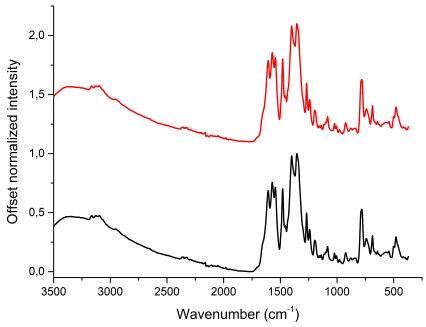

(a) FT-IR-ATR spectra of S56 (black) and S57 (red)

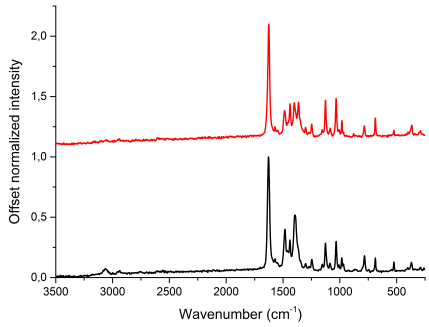

(b) Raman spectra of S56 (black) and S57 (red)

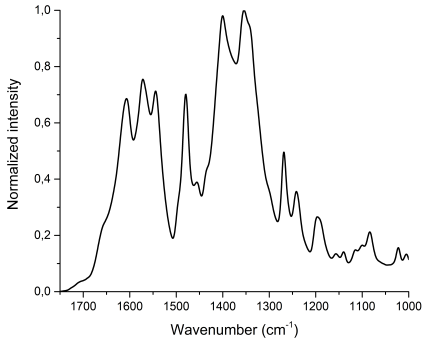

(c) FT-IR-ATR spectrum of S56 - detail

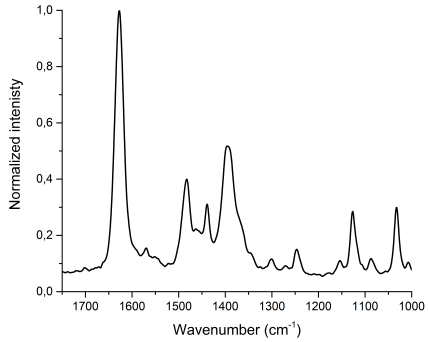

(d) Raman spectrum of S56 - detail

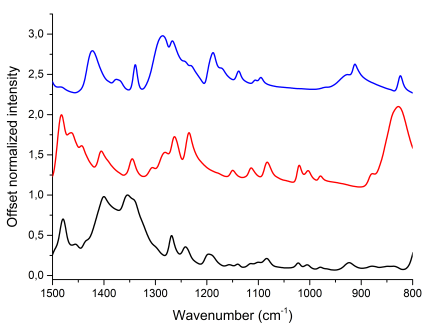

(e) FT-IR-ATR spectra of S56 (black), Fe^{II} complex (red), H_2ndc (blue)

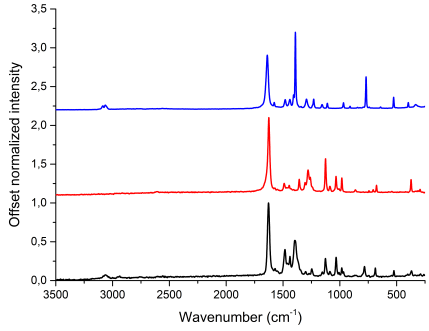

(f) Raman spectra of S56 (black), Fe^{II} complex (red), H_2ndc (blue)

Figure 4.2: Normalized vibrational spectra of Zr−Fe−ndc syntheses

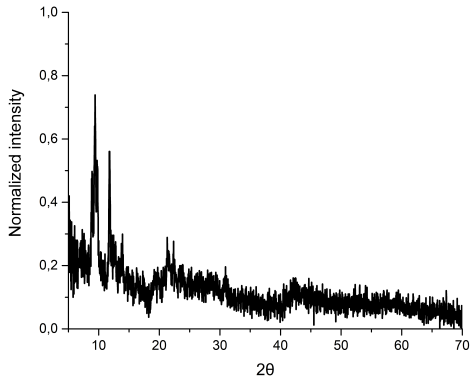

Figure 4.3: Powder diffractogram of LA87

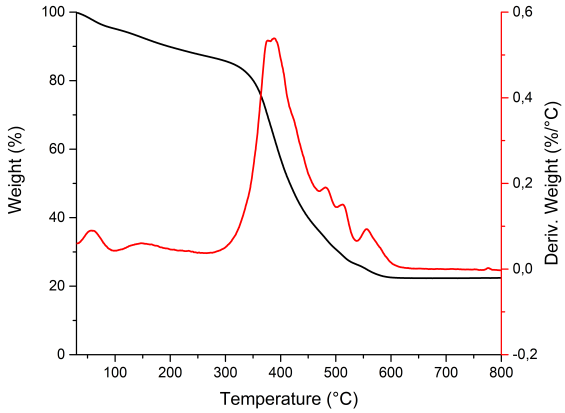

Figure 4.4: TGA of S66

Table 4.2: List of Zn−sdc−Fe MOF syntheses. All syntheses were carried out in 30 mL Pyrex glass vials.

Name	Solvent	Amount of product retrieved (mg)
S79	DMF	23.9
S80	DMF/EtOH 2:1	51.6
S81	DMF/MeOH 9:1	31.7
LA70	DMF/MeOH 9:1	17.52

4.1.3 Zn−sdc−Fe MOF

Syntheses were carried out with $4.5 \cdot 10^{-2}$ mmol of $Zn(NO_3)_2 \cdot 6\,H_2O$, $4.5 \cdot 10^{-2}$ mmol of H_2sdc, and $2.25 \cdot 10^{-2}$ mmol of Fe^{II} carbene complex. The overall Zn:sdc:Fe ratio is $2 : 2 : 1$, the same one used for Zn−ndc−Fe syntheses in the previous section. All the different trials were carried out with 10 mL of solvent, either with pure DMF, or with a DMF/EtOH $9 : 1$ or DMF/MeOH $9 : 1$ mixture (table 4.2).

All the syntheses reported in table 4.2 yielded red crystals: DMF/EtOH and DMF/MeOH provided bigger crystals and orange solutions, while S79 had a more red solution. Generally, these syntheses gave a greater amount of product compared to the Zn−ndc−Fe ones, starting with the same moles of reagent. While it's true that H_2sdc is heavier than H_2ndc, this is not the main cause of the difference in the amounts of products; the increased yields for 4,4'-stilbenedicarboxylate products could be the consequence of their easier formation compared to the 2,6-naphtalenedicarboxylate product, possibly because the similarity in length between the Fe^{II} complex and 4,4'-stilbenedicarboxylic acid favours the formation of a mixed ligand MOF.

Crystals of the products with 4,4'-stilbenedicarboxylate are bigger than those with 2,6-naphtalenedicarboxylate, their length exceeding the millimetre; the crystals look like elongated lamellae, their shape recalling those of little daggers. Even in this case, the crystals faded quickly when taken out from their mother solutions, losing colour brightness and eventually breaking into smaller particles. Figure 4.5 shows crystals after filtration and crystals dried and re-immersed in DMF, the latter being brighter and with more vivid colours than the former. While the crystallinity of the samples in DMF mother solution could not be assessed, p-XRD on LA70

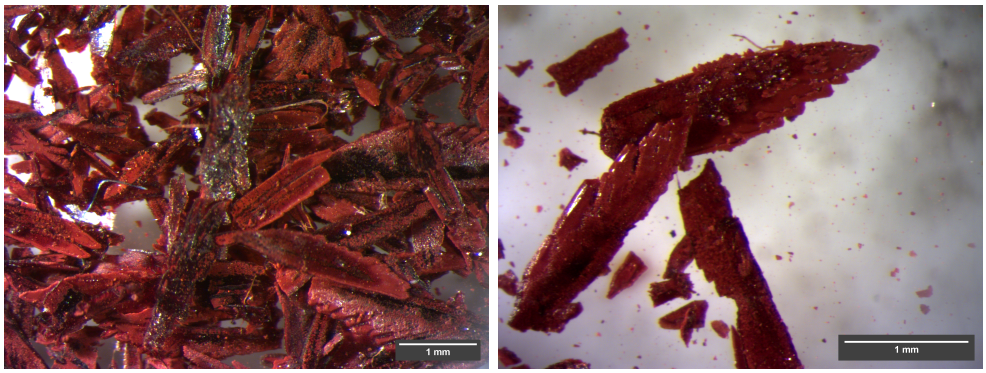

(a) Crystals filtered, washed with DMF and left to dry in air

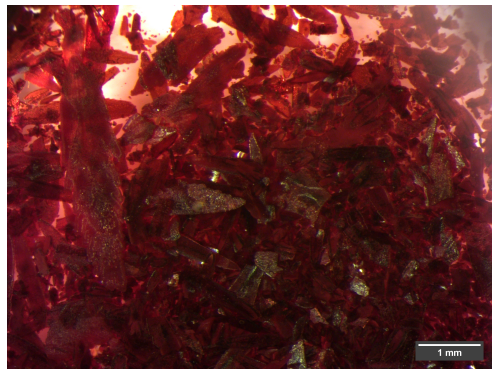

(b) Crystals re-immersed in DMF

Figure 4.5: Images of S81 acquired at the stereomicroscope

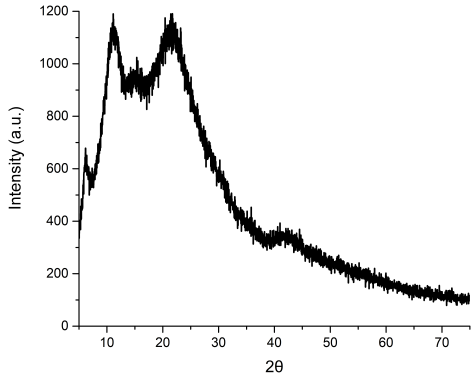

Figure 4.6: Powder diffractogram of LA70

yields a very noisy and broad signal (figure 4.6), which is linked to the presence of amorphous material in the sample. Even though all the samples showed crystals potentially suitable for SC-XRD measurements, it was not possible to carry out these measurements because of their very quick fading and cracking.

FT-IR-ATR and Raman spectra have been recorded on the product washed three times with DMF and then three times with dichloromethane, by directly soaking the crystals in these solvents for approximately 4 hours per washing cycle. Raman spectra assess the presence of both 4,4'-stilbenedicarboxylate and the Fe^{II} complex: signals at 1603 and 1196 cm^{-1} are uniquely ascribed to 4,4'-stilbenedicarboxylate, while those at 1033 and 982 cm^{-1} to the Fe^{II} complex (figure 4.7). As far as infrared spectrum is concerned, the same observations of the Zn−ndc−Fe system can be made: asymmetric carboxylate stretching modes are shifted in the $1540 - 1610$ cm^{-1} range, while its symmetric stretching modes are in the $1330 - 1400$ cm^{-1} range. Thus, concerning COO^- vibrations no significant spectroscopic differences between Zn−ndc−Fe and Zn−sdc−Fe arise from the coordination of two different carboxylate based ligands; the small differences in the two systems are mostly associated to other characteristic vibrational modes of the two organic ligands.

SEM images of S81 have been acquired; the pictures in figure 4.8 show a material with a lot of cracks, and some spots appear to be formed by thin sheets layered one on the other, with a remarkable tendency towards

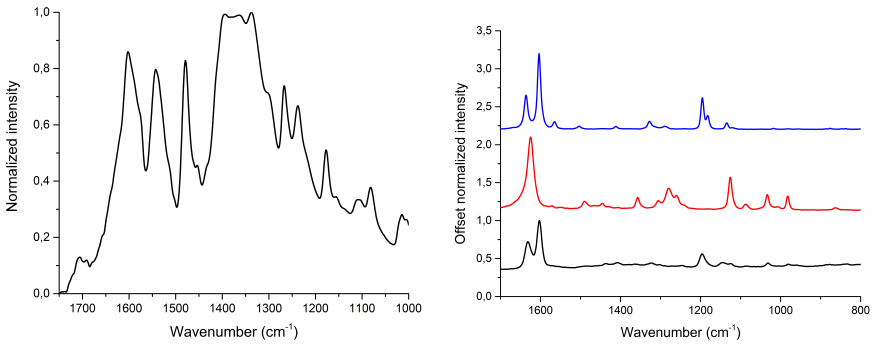

(a) FT-IR-ATR spectrum of S81

(b) Raman spectra of S81 (black), Fe^{II} complex (red), H_2sdc (blue)

Figure 4.7: Normalized vibrational spectra of Zn−Fe−sdc product

exfoliation. The fractures observed are a direct consequence of crystal fading after solvent loss, and are responsible for the breaking of big crystals into a fine powder. The pictures also highlight flat and regular surfaces, from which portion of material seldom protrude; interestingly, back-scattered electrons (BSE) images do not differ from the secondary electron (SE) ones, meaning that the composition of the material is highly homogeneous, both on the regular flat surfaces and on the protruding aggregates.

Energy-dispersive X-ray spectroscopy (EDS) was carried out on four different sites of the sample; data reveal an average Zn:Fe molar ratio of 3.5 : 1 for the measured points. Areas of roughly 30x30 µm were mapped as well, revealing a highly homogeneous distribution of these two metals in the sample. Lighter elements such as C, O and N were detected as well, but the technique does not allow a reliable quantification of elements below atomic number 11. However, even in this case the distribution maps highlight a homogeneous dispersion in the analysed areas; moreover, qualitative evaluation of the elemental ratios for these light elements is in agreement with a Fe^{II} : stilbenedicarboxylate ratio around 2 : 1.

4.2 Zr-MOFs

Many parameters are believed to affect MOF stability, and they are both linked to the ligands and the metals involved: pK_a of the ligand,

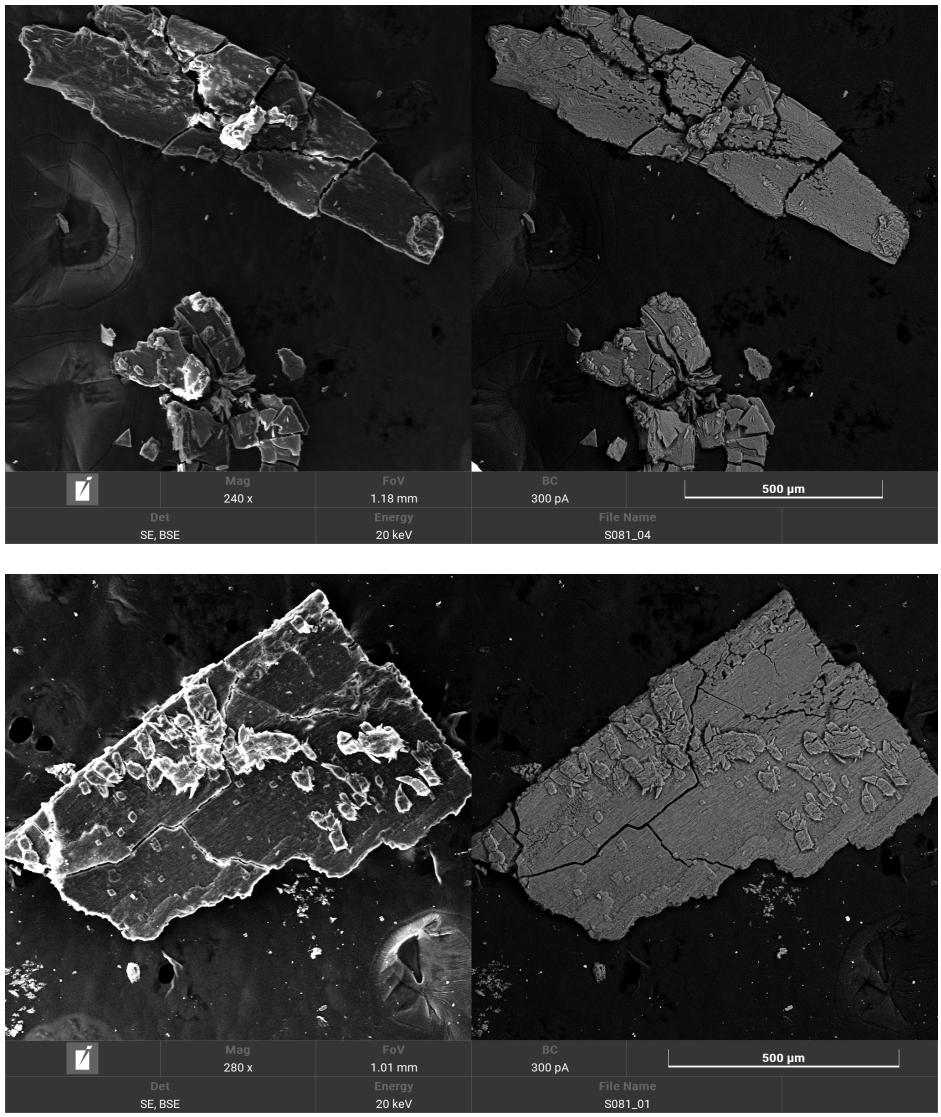

Figure 4.8: SEM pictures of S81; for each image, secondary electron (SE) images are on the left side, backscattered electron (BSE) on the right

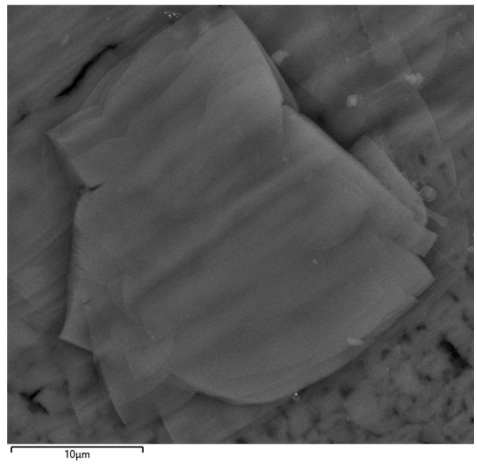

(a) Mapped sample area

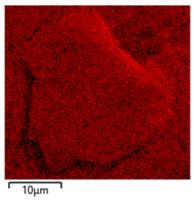

(b) C K_{α_1} K_{α_2}

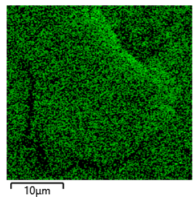

(c) O K_{α_1}

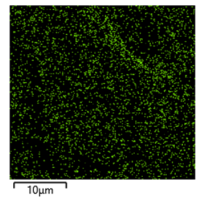

(d) N K_{α_1} K_{α_2}

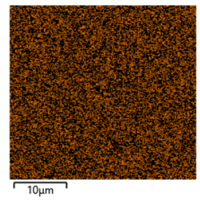

(e) Zn K_{α_1}

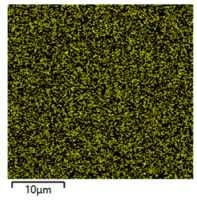

(f) Fe K_{α_1}

Figure 4.9: EDS maps of S81

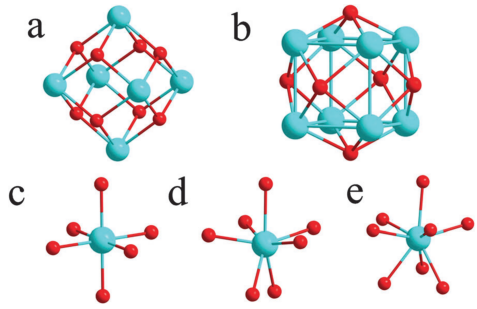

Figure 4.10: Zr clusters and cores. (a) Zr_6O_8 (b) Zr_8O_6 (c) ZrO_6 (d) ZrO_7 (e) ZrO_8. Atom colour scheme: O, red, and Zr, blue. From reference [82].

oxidation state, reduction potential and ionic radius for metals. Parameters depending both on metal and ligand are very important, such as the coordination geometry and metal-ligand bond strength, which is considered crucial in assessing hydrothermal stability of MOFs [82]. According to Pearson's classification of *hard/soft* acid and bases [76], some qualitative considerations can be done on the affinity between metal ions and atoms of the linker involved in coordination. Metal ions with high charge density have great bonding affinity for atoms with high charge densities (*hard-hard* interaction), and the same observation can be done for the opposite couple (*soft-soft* interaction). This high affinity results in a higher bond strength for *hard-hard* and *soft-soft* couples. In this context, Zirconium based MOFs (Zr-MOFs) feature Zr^{IV}, a high charge density metal ion and thus a *hard* acid, showing a strong affinity to *hard* bases, such as carboxylate O atoms. The coordination bonds are thus very strong: as a result, these materials are highly stable in organic solvents, water, and even in acidic solutions.

Zr-MOFs structures are built from inorganic building units of Zr^{IV} oxo clusters, connected through polytopic ligands featuring carboxylate moieties. Depending on the coordination environment of the metal nodes, different topologies are possible. Two types of clusters have been reported thus far: Zr_6O_8 and Zr_8O_6. Some Zr-MOFs feature single Zr^{IV} ions as metal nodes, or chain structures formed by Zr^{IV} ions and ligands (figure 4.10).

The Zr_6O_8 cluster is one of the most commonly observed: six Zr^{IV} ions form the vertices of an octahedron, whose triangular faces are alternatively

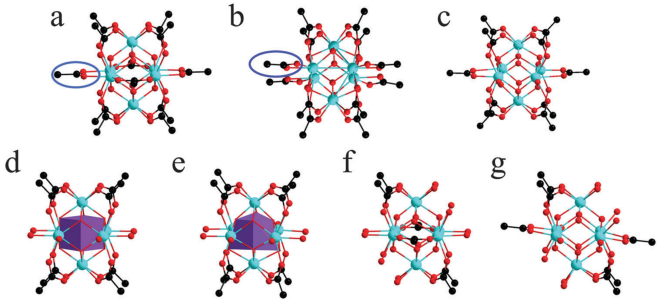

Figure 4.11: The observed SBU based on $Zr_6(\mu_3\text{-}O)_4(\mu_3\text{-}OH)_4$ cluster in reported Zr-MOFs: (a) 12-connected $Zr_6(\mu_3\text{-}O)_4(\mu_3\text{-}OH)_4(CO_2)_{12}$ in UiO-66; (b) 12-connected $Zr_6(\mu_3\text{-}O)_4(\mu_3\text{-}OH)_4(CO_2)_{12}$ in PCN-223; (c) 10-connected $Zr_6(\mu_3\text{-}O)_4(\mu_3\text{-}OH)_4(CO_2)_{10}(AcO)_2$ in DUT-69; (d) 8-connected $Zr_6(\mu_3\text{-}OH)_8(OH)_4(CO_2)_8$ in PCN-222; (e) distorted 8-connected $Zr_6(\mu_3\text{-}O)_4(\mu_3\text{-}OH)_4(OH)_4(H_2O)_4(CO_2)_8$ in PCN-225; (f) 6-connected $Zr_6(\mu_3\text{-}O)_4(\mu_3\text{-}OH)_4(OH)_6(H_2O)_6(CO_2)_6$ in PCN-224; (g) 6-connected $Zr_6(\mu_3\text{-}O)_4(\mu_3\text{-}OH)_4(OH)_6(H_2O)_6(CO_2)_6$ in PCN-777. Atom colour scheme: C, black; O, red; and Zr, blue. From reference [82].

capped by four μ_3-O and μ_3-OH groups. Depending on the number of coordinated carboxylates on the coordination geometry, the secondary building unit can have different symmetries. For 12-connected clusters, each Zr^{IV} is eight-coordinated by O atoms in a square antiprismatic geometry: four of these O atoms belong alternatively to μ_3-O and μ_3-OH groups, while the remaining four are from carboxylate ligands. The resulting secondary building unit is thus $Zr_6(\mu_3\text{-}O)_4(\mu_3\text{-}OH)_4(CO_2)_{12}$: it has a O_h-symmetry and is found in the majority of Zr-MOFs (figure 4.11 a). A 12-coordinated cluster with the lower D_{6h}-symmetry has been recorded: each Zr^{IV} is eight-coordinated by two μ_3-O, two μ_3-OH, and four O atoms provided by only *three* carboxylates [83]. As a result, only eight carboxylates out of twelve are bridging two adjacent Zr^{IV}, and the remaining four chelate single Zr^{IV} and are disposed on the equatorial plane (figure 4.11 b).

It is thus clear that the Zr^{IV} clusters provide a potentially wide spectrum of topologies thanks to the different available sites on the metal-oxo nodes. By reducing the connectivity, we can find 10-connected SBUs such as in

DUT-69 [84], where ten edges of the Zr^{IV} cluster are occupied by carboxylic groups of the ligands while the remaining four are capped by acetate ions and water (figure 4.11 c); 8-coordinated systems such as PCN-222 [85], where eight edges of the cluster are occupied by carboxylates and the four equatorial positions are occupied by OH^- groups (figure 4.11 d), or as in PCN-225 [86], where the eight μ_3-O)$_4$ form a distorted octahedron (figure 4.11 e). Finally, 6-connected SBUs have been observed as well, where H_2O and OH^- groups cap the uncoordinated positions (figure 4.11 f and g) [87, 88].

Another cluster for Zr-MOFs is Zr_8O_6, where each Zr^{IV} occupies the vertices of a cube and the six faces are occupied by μ_4-O, thus resulting in each Zr^{IV} binding three O atoms of the cluster and four carboxylate O atoms (figure 4.10 b) [89]. Finally, Zr^{IV} cores can be found in MOF nodes composed only by one Zr^{IV} ion coordinated to oxygen atoms: ZrO_6 [90–92], ZrO_7 [93, 94] and ZrO_8 [95, 96] (figure 4.10 c, d and e). These examples are more rare and can be found with peculiar ligands, such as phosphonates and gallates.

Whichever coordination adopted in the framework, strong Zr−O bond polarisation has two effects: fast nucleation and slow and difficult ligand exchange. While the former factor hinders mostly the dimension of crystals, the latter affects both crystal growth and defects repairing through ligand exchange on the clusters. In fact, being already disfavoured by entropy, the rearrangement of polytopic linkers connecting more than one cluster requires a high amount of energy, since Zr−O bonds are very stable.

The modulated synthesis offers a solution to these issues. A modulator is a molecule with the same functional group of the linker that contains only one coordination site (e.g. a monocarboxylic acid), and can thus compete with the linker for the coordination to the metal nodes, slowing down both nucleation and crystal growth. Since modulators have only one binding functional group per molecule, with sufficient reaction time the overall entropy gain will always favour the coordination of the polytopic linker and the release of free modulator molecules from the metal nodes, thus ensuring high crystallinity in the final product. Moreover, modulating agents may promote anisotropic growth of crystals through selective regulation of coordination interactions in one of the coordination nodes, resulting in a control over the morphology of the formed crystals. Another advantage

of the use of modulators is the reduced agglomeration of the particles formed: the more the crystals grow, the less polytopic linker is available for coordination of metal nodes at their surface, which can thus be occupied by the modulator. The preferential coordination of these molecules over those of the linker prevents the latter from bridging two (or more) different crystallites; the overall result is a reduced agglomeration of the final product.

Modulators can also act as structure-directing agents, by binding to the metal nodes in specific positions and lowering the cluster coordination number. In these cases, the final products feature higher porosity, and depending on the choice of the modulator different structures can be obtained.

Finally, the modulated approach enhances the reproducibility of the syntheses and of the crystal features, such as size, morphology and crystallinity. The choice of the modulator is usually a result of a trial and error process, and so is its concentration. Even if many studies highlighted the best conditions to be used to obtain a crystalline and reproducible product [97], it is difficult to draw universally applicable rules for modulated MOF synthesis.

Besides offering stable and robust materials, using Zr^{IV} provides a metal centre that does not absorb visible light, since there are no *d* electrons in the outer electron shell of Zr^{IV}. On the other hand, many studies have shown that Zr^{IV} nodes provide *d* states whose energy is too high compared to the lowest unoccupied linker orbitals, resulting in poor ligand to metal charge transfer for photoexcited ligand electrons [54, 98]. Overall, a Zr-MOF with the Fe^{II} carbene complex would preserve the optical properties of the complex, but would also provide an environment where the chromophores are ordered and strongly bound to the Zr^{IV}, lowering the chances of non-radiative decay of the photoexcitation.

The length of the Fe^{II} carbene complex is around 12.41 Å, and it has been determined from its crystal structure, by taking the distance between the two C atoms in the carbonyl groups. Zr-MOFs with linkers of similar length have been reported: for example, 4,4'-stilbenedicarboxylic acid (H_2sdc) has about the same length of the complex (12.25 Å). It can form MOFs with the formula $Zr_6(\mu_3\text{-}O)_4(\mu_3\text{-}OH)_4(sdc)_6$, featuring the 12-coordinated octahedral Zr_6O_8 cluster. The linker itself is non linear, due to the alkene moiety bridging the two aromatic rings. In the MOF, the ligand is geometrically

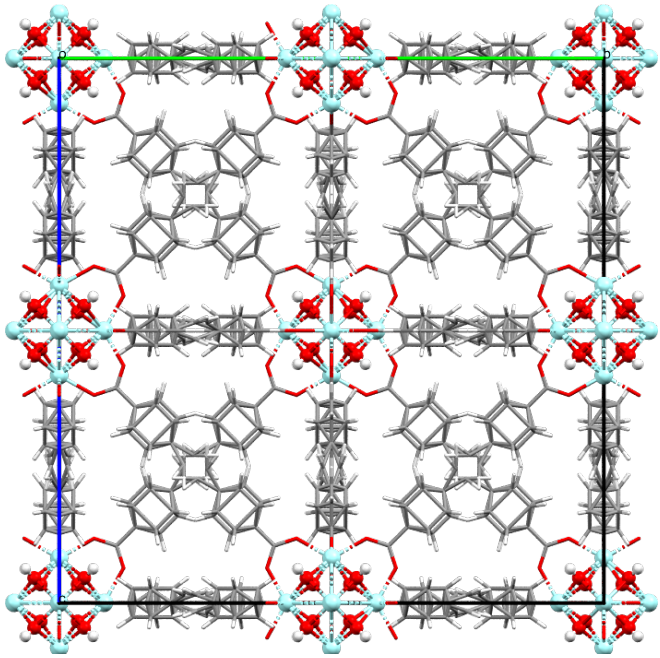

Figure 4.12: Structure of $Zr_6(\mu_3\text{-}O)_4(\mu_3\text{-}OH)_4(sdc)_6$ along crystallographic axis a.

strained, resulting in an end-to-end disorder within the structure (figure 4.12)[99].

This MOF is stable upon heating up to 500 °C, and it appears to be easily obtainable through traditional modulated syntheses, either with amino acids or with benzoic acid as modulator [99–101]. It can be thus imagined that the Fe^{II} carbene complex could be incorporated in a MOF with mixed linker, since both the complex and H_2sdc have similar length and are stable in the reaction conditions required. However, a different coordination on the Zr^{IV} cluster should be expected, since the Fe^{II} complex is more bulky than the organic ligand and may force some coordination site to be coordinated to the smaller modulator molecules.

4.2.1 Materials and methods

The syntheses have been carried out in 6 mL DURAN® glass vials (height 100 mm), with screw caps made of PBT (polybutene terephtalate) with PTFE-coated seals. These vessels are completely autoclavable and can withstand temperatures up to 180 °C. Heating is provided through a silicone oil thermostatic bath at 120 °C, unless otherwise noted; the oil bath was kept in an aluminum pot under constant stirring, to ensure uniform heating. High-boiling point solvents have been used, such as DMF or DEF, and modulators added to the syntheses. Since the reactions are carried out in solvothermal conditions, the reaction volume has been kept *below or up to* one third of the total reaction volume of the vessel (thus, 2 mL reaction volume for the glass vials). Leaving two thirds of free volume helps preventing explosion risks related to autogenous pressure developed during the reaction. Reactions where heated for 48 h and allowed to cool at room temperature, unless otherwise noted.

Depending on the choice of the modulator, the synthetic procedure changes slightly. When modulators in the liquid state at room temperature (that is HCOOH and CH_3COOH) are used, the Zr^{IV} salt is placed in the vessel and the modulator added shortly after. The vessel is then sonicated for 1 or 2 minutes; then, the ligand is added as a solid, and the solvent is placed in the vessel. The reaction mixture is then sonicated for $10 - 15$ minutes and then placed in the oil bath. For solid modulators (such as benzoic acid), both the modulator and the Zr^{IV} salt are added as solids in the reaction vessel, then the solvent is added. The mixture is sonicated for 10 minutes until clear; then, the ligand is added, the resulting mixture sonicated for $10 - 15$ minutes and then placed in the oil bath.

When stock solutions are used, the preparation is different for the Zr^{IV} and the ligand solution. The desired quantity of the Zr^{IV} salt is dissolved in the liquid modulator of choice, and then sonicated for 5 minutes to ensure complete dissolving, while ligands are dissolved in the solvent and then sonicated for 5 minutes until completely dissolved. Note that H_2sdc is insoluble in every solvent used for the syntheses of Zr-MOFs, so no stock solution has been prepared for this ligand. Note also that Zr^{IV} salt stock solutions need to be freshly prepared and readily used, otherwise a white precipitate starts to form.

Syntheses carried out in autoclave undergo the same procedure as those

explained before. Stainless steel autoclaves from Yuyao Haiju Laboratory Equipment have been used; the total volume of the teflon chamber is 100 mL, so the reaction volume used is 25 mL. Extreme care must be used when opening an autoclave after cooling it down to room temperature, since overpressure developed during the reaction could be high.

Before every use, glassware and autoclave teflon vessels are thoroughly washed according to the following procedure. Labware is soaked overnight in a base bath, which can be prepared by slowly adding 560 g of KOH into 2 L of deionised water and stirring until dissolved, followed by the addition of 8 L of isopropyl alcohol. The glassware is then rinsed with tap water and soaked overnight in a weak acid bath, which is made by using deionised water and a small quantity of CH_3COOH. This last step ensures the protonation of the Si−OH groups at the surface of the glass vessels, so that it is not electrostatic. Finally, the glassware is rinsed with deionised water and dried in a dedicated oven at 120 °C for 2 h.

Directly after the synthesis, every product has been washed with the same procedure: $1-2$ mL of DMF were put in the reaction vessel, stirred for a few seconds and left to exchange for about 4 h. This step was repeated three times; then, $1-2$ mL of acetone were put in the vessel, manually stirred for a few seconds and left to exchange for about 4 h. This step was repeated thrice. Finally, the solvent was removed with a pipette and the product left to dry inside the same vessel under the hood overnight. For syntheses in autoclave, the amount of solvent varies, depending on the amount of product. As a general rule, the products need to be completely covered by the solvent, and the solvent level should be above the product for about 2 cm. This washing procedure ensures that the DMF diffuses into the pores of the MOF, dissolves unreacted reagents and takes them out of the material; washing with acetone ensures that all the DMF in the MOF pores is taken outside the pores. Moreover, since acetone has a low boiling, it easily evaporates from the pores and grants an efficient drying of the material.

Micro-Raman measurements were carried out on an instrument equipped with an optical petrographic microscope Olympus BX41. The microscope is arranged to allow observations in transmitted and reflected light, and is equipped with the polarizer, analyser, and a colour video camera. It is characterized by a confocal optical system linked to the spectrometer. The

objectives 10X, 20X, 50X and 100X (spot of about 2.1 µm) are long working distance. A 4X magnification is also available for macroscopic analysis. The instrument is equipped with an Horiba JobinYvon HR800 spectrometer, with two gratings 1800 and 600 grooves/mm and CCD detector cooled at $-70°C$. Measurements were carried out with Nd solid state green laser light (532 nm, 250 mW, spectral resolution 2 cm^{-1}).

SC-XRD measurements, FT-Raman and ATR spectra, DR-UV-Vis-NIR and steady-state emission spectra were recorded with the same instrumentation of section 3.1.

X-ray powder diffraction patterns (p-XRD) were collected by a Philips X'pert PRO automatic diffractometer operating at 40 kV and 40 mA, in theta-theta configuration, secondary monochromator with Cu Kα radiation ($\lambda = 1.5418$ Å) and a Pixel solid-state detector (active length in $2\theta - 3.347°$). Data were collected from 5 to 75° 2θ with a step size of 0.026° and a time per step of 700 s at RT (total time 2 h). 1° fixed soller and divergence slits giving a constant volume of sample illumination were used.

SEM images were recorded with a Hitachi S-4800 FEG-SEM operating at an accelerating voltage of 5 kV. Samples were coated with a 10 nm gold layer in an Emitech K550x ion sputter.

$ZrCl_4$ anhydrous 98% (233.04 g/mol, CAS: 10026-11-6), HCOOH 99% (46.03 g/mol CAS: 64-18-6) CH_3COOH 99.8% (60.05 g/mol, CAS: 64-19-7), CF_3COOH 99% (114.02 g/mol, CAS: 76-05-1) were bought from Acros Organics. Small portions of $ZrCl_4$ anhydrous were put in tightly closed vials and kept in a desiccator. $ZrOCl_2 \cdot 8\,H_2O$ 98% (322.25 g/mol, CAS: 13520-92-8), benzoic acid PhCOOH 99.6% (122.12 g/mol, CAS: 65-85-0) were bought from Thermo Fischer Scientific. H_2sdc 96% (268.26 g/mol, CAS: 100-31-2) was bought from Alfa Aesar.

X-ray fluorescence spectra were recorded with THERMO Niton XL3T GOLDD portable instrumentation, equipped with a Large Drift Detector (25 mm^2 surface, 125 eV resolution). Each analysis covers a circular area of 3 mm, and four sequential measurements were carried out, with 4 different voltage settings and currents, to optimise data collection for different parts of the spectrum. The total analysis time was around 120 s.

4.2.2 $Zr_6(\mu_3\text{-}O)_4(\mu_3\text{-}OH)_4(sdc)_6$ syntheses

The Zr-sdc MOF belongs to the series of UiO-66 frameworks; the first synthesis and characterisation of the material were reported by Marshall et al. [99] The authors used L-proline as modulator, as well as small quantities of concentrated HCl: this strategy has been previously used by the same authors for the synthesis of another MOF of the UiO-66 series [102]. They were interested in studying the selective bromination of the alkene double bond on the 4,4'-stilbenedicarboxylic acid within the MOF, and to characterise the resulting material after the reaction. They claimed they solved the crystal structure for this system, and provide p-XRD diffractograms assessing the phase purity of the product. Xu et al. [100] conducted other studies on $Zr_6(\mu_3\text{-}O)_4(\mu_3\text{-}OH)_4(sdc)_6$, providing further insights on post-synthetic bromination of this MOF. The authors suggest another synthesis, using benzoic and trifluoroacetic acid as modulators, with higher temperatures and longer reaction times.

Besides the differences in temperature and in the choice of the modulator, these two syntheses share some similarities, such as the choice of the metal precursor used and the metal : ligand ratio, set to 1 : 1. The present work aimed to understand if it was possible to synthesise the MOF by avoiding amino acids, using either formic or acetic acid, and to replicate the synthesis proposed by Xu et al. [100, 101] The complete list of the syntheses for $Zr_6(\mu_3\text{-}O)_4(\mu_3\text{-}OH)_4(sdc)_6$ can be found in table 4.3.

Table 4.3: Syntheses of $Zr_6(\mu_3\text{-}O)_4(\mu_3\text{-}OH)_4(sdc)_6$; syntheses marked by * have been carried out in autoclave at 145 °C; AA = acetic acid, FA = formic acid, BA = benzoic acid, TFA = trifluoroacetic acid

Name	**Zr^{IV} salt**	**Zr^{IV}** (mmol)	**H_2sdc** (mmol)	**M:L ratio**	**Modulator**
LA 4-A	$ZrCl_4$	$5.15 \cdot 10^{-2}$	$5.15 \cdot 10^{-2}$	1 : 1	FA
LA 4-B	$ZrCl_4$	$5.15 \cdot 10^{-2}$	$5.15 \cdot 10^{-2}$	1 : 1	AA
LA 6-A	$ZrCl_4$	$4.30 \cdot 10^{-2}$	$4.30 \cdot 10^{-2}$	1 : 1	FA
LA 6-B	$ZrCl_4$	$5.00 \cdot 10^{-2}$	$5.00 \cdot 10^{-2}$	1 : 1	AA
LA 8-A	$ZrCl_4$	$4.30 \cdot 10^{-2}$	$4.30 \cdot 10^{-2}$	1 : 1	FA
LA 8-B	$ZrCl_4$	$5.00 \cdot 10^{-2}$	$5.00 \cdot 10^{-2}$	1 : 1	AA
LA 9-A	$ZrCl_4$	$4.08 \cdot 10^{-2}$	$4.08 \cdot 10^{-2}$	1 : 1	BA, TFA
LA 9-B	$ZrCl_4$	$4.08 \cdot 10^{-2}$	$4.08 \cdot 10^{-2}$	1 : 1	BA, TFA
LA 9-C	$ZrCl_4$	$4.08 \cdot 10^{-2}$	$4.08 \cdot 10^{-2}$	1 : 1	FA
LA 9-D	$ZrCl_4$	$4.08 \cdot 10^{-2}$	$4.08 \cdot 10^{-2}$	1 : 1	FA
LA 10-A	$ZrCl_4$	$4.08 \cdot 10^{-2}$	$4.08 \cdot 10^{-2}$	1 : 1	BA, TFA
LA 10-B	$ZrCl_4$	$4.08 \cdot 10^{-2}$	$4.08 \cdot 10^{-2}$	1 : 1	BA, TFA
LA 10-C	$ZrOCl_2 \cdot 8\,H_2O$	$4.08 \cdot 10^{-2}$	$4.08 \cdot 10^{-2}$	1 : 1	BA, TFA
LA 10-D	$ZrOCl_2 \cdot 8\,H_2O$	$4.08 \cdot 10^{-2}$	$4.08 \cdot 10^{-2}$	1 : 1	BA, TFA
LA 11-A	$ZrCl_4$	$4.08 \cdot 10^{-2}$	$4.08 \cdot 10^{-2}$	1 : 1	BA, TFA
LA 11-B	$ZrCl_4$	$4.08 \cdot 10^{-2}$	$4.08 \cdot 10^{-2}$	1 : 1	BA, TFA
LA 11-C	$ZrCl_4$	$4.08 \cdot 10^{-2}$	$4.08 \cdot 10^{-2}$	1 : 1	BA, TFA
LA 11-D	$ZrCl_4$	$4.08 \cdot 10^{-2}$	$4.08 \cdot 10^{-2}$	1 : 1	BA, TFA
LA 11-E	$ZrCl_4$	$4.08 \cdot 10^{-2}$	$4.08 \cdot 10^{-2}$	1 : 1	BA, TFA

Continued on the next page

Continued from previous page

Name	**Zr^{IV} salt**	**Zr^{IV}**	**H_2sdc**	**M:L**	**Modulator**
LA 11-F	$ZrCl_4$	$4.08 \cdot 10^{-2}$	$4.08 \cdot 10^{-2}$	1 : 1	BA, TFA
LA 24-A	$ZrCl_4$	$4.08 \cdot 10^{-2}$	$4.08 \cdot 10^{-2}$	1 : 1	TFA
LA 24-B	$ZrCl_4$	$4.08 \cdot 10^{-2}$	$4.08 \cdot 10^{-2}$	1 : 1	TFA
LA 36-A	$ZrCl_4$	$5.15 \cdot 10^{-2}$	$2.57 \cdot 10^{-2}$	2 : 1	FA
LA 36-B	$ZrOCl_2 \cdot 8\,H_2O$	$5.15 \cdot 10^{-2}$	$2.57 \cdot 10^{-2}$	2 : 1	FA
LA 44-A	$ZrCl_4$	$5.15 \cdot 10^{-2}$	$2.57 \cdot 10^{-2}$	2 : 1	FA
LA 44-B	$ZrOCl_2 \cdot 8\,H_2O$	$4.96 \cdot 10^{-2}$	$2.48 \cdot 10^{-2}$	2 : 1	FA
LA 45-A	$ZrCl_4$	$5.15 \cdot 10^{-2}$	$3.43 \cdot 10^{-2}$	1.5 : 1	FA
LA 45-B	$ZrOCl_2 \cdot 8\,H_2O$	$4.96 \cdot 10^{-2}$	$3.31 \cdot 10^{-2}$	1.5 : 1	FA
LA 47*	$ZrCl_4$	0.51	0.51	1 : 1	BA, TFA
LA 48*	$ZrOCl_2 \cdot 8\,H_2O$	0.283	0.121	2.3 : 1	FA
LA 49*	$ZrCl_4$	0.643	0.321	2 : 1	FA

Concluded from previous page

Synthesis LA 4 keeps the same M:L ratio, solvent (DMF) and Zr^{IV} salt as the literature recipes; reaction time was 24 h. Using formic acid yielded a product (4-A) that is more crystalline than the one obtained with acetic acid (4-B), as can be seen in the diffractograms in figure 4.13. Compared to the calculated p-XRD pattern of the literature MOF, 4-A shows a few similarities, such as the peak around 10°; however, the diffractogram of 4-A lacks many other peaks, while 4-B can be considered completely amorphous.

Lowering M:L ratio (LA 6) or diluting the synthesis (LA 8, total volume 8 mL) yielded in both cases only unreacted free ligand.

Using DMF-ROH solvent mixtures (LA 9-C,D) with formic acid yielded unreacted ligand as well as a new phase which features two peaks below 10°. These observations suggest that both M:L ratio and the choice of solvent are crucial factors in the synthesis of this MOF: an excess of ligand appears to be an unfavourable choice, since it does not provide a crystalline phase; besides, the excess of H_2sdc can not be eliminated from the final product by washing with DMF, since the ligand is not soluble. On the other hand, mixtures of DMF and alcohols do not provide the desired product.

While low M:L ratios proved to be unsuccessful, raising the ratio (LA 36-A) yielded a crystalline material; the diffractogram shows two strong peaks around 10°, and other smaller ones at higher angles (figure 4.14). An increase in the baseline can be observed between 25° and 30°, suggesting the presence of an amorphous component in the final product. Comparison with the calculated powder diffraction pattern of the literature MOF highlights many differences between the obtained product and the reported material. The same synthesis with $ZrOCl_2 \cdot 8\,H_2O$ (LA 36-B) yielded the same product as 36-A. Replicas of the two syntheses have been carried out for 72 h (LA 44-A,B): the diffraction pattern of 44-A is similar to 36-A, even if there may be more amorphous component compared to 36-A, while 44-B is amorphous. Finally, using a M:L ratio of 1.5 : 1 yields the same products of the syntheses with the 2 : 1 ratio (LA45-A,B). It is thus clear that an excess of Zr^{IV} over the ligand is generally suitable for achieving products with high crystallinity.

Another synthesis was carried out in autoclave, upscaled from 36-A to the maximum solvent level of the autoclave (25 ml) and heated to 145 °C for 24 h. The product shows very high crystallinity, as can be seen by the strong and well resolved diffraction peaks in the p-XRD pattern (figure

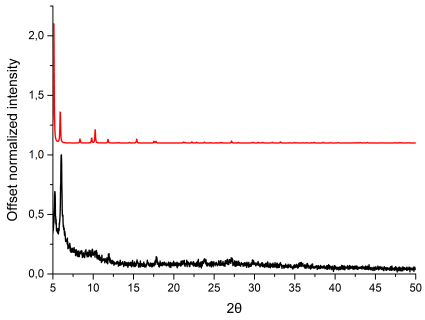

(a) LA4-A (black) and calculated Zr-sdc MOF (red)

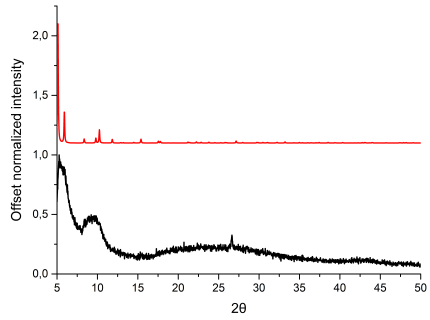

(b) LA4-B (black) and calculated Zr-sdc MOF (red)

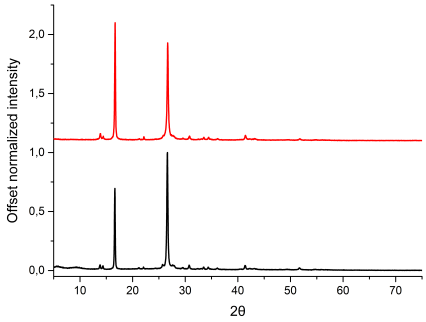

(c) LA6-A (black) and H_2sdc (red)

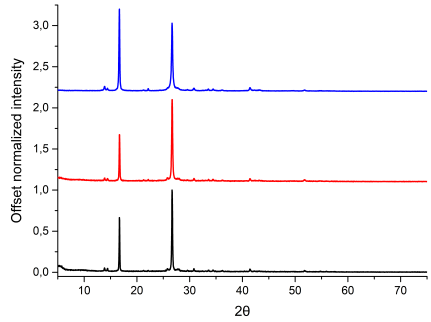

(d) LA8-A (black), 8-B (red) and H_2sdc (blue)

Figure 4.13: Normalized p-XRD diffractograms of syntheses LA-4,6,8

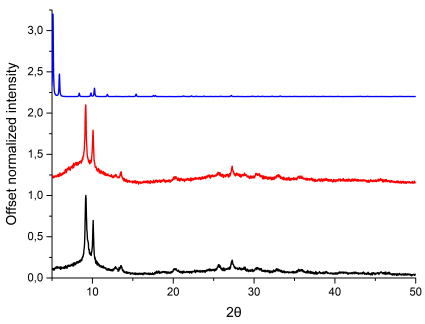

(a) LA36-A (black), B (red) and calculated Zr-sdc MOF (blue)

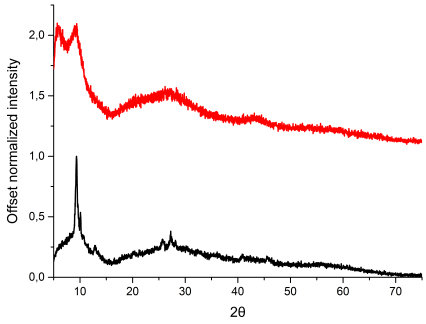

(b) LA44-A (black) and B (red)

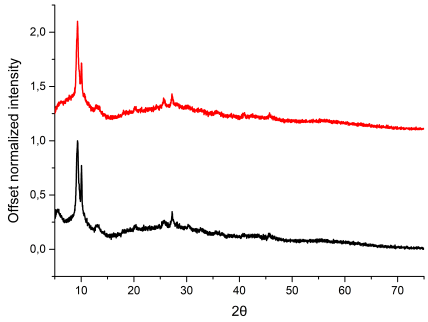

(c) LA45-A (black), B (red)

Figure 4.14: Normalized p-XRD diffractograms of syntheses LA-36,44,45

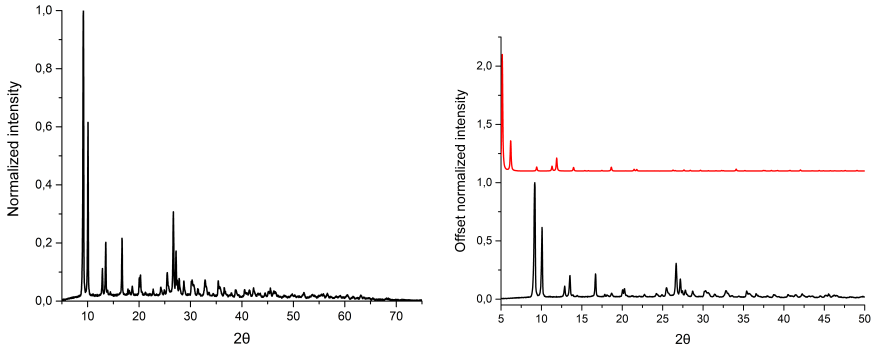

(a) LA-49

(b) LA-49 (black) and calculated Zr-sdc MOF (red)

Figure 4.15: Normalized p-XRD diffractograms of LA-49

4.15). A comparison of the diffractograms suggests that this material should be the same obtained in 36-A, with higher crystallinity and without any amorphous phase. Both these scenarios are equally possible, since many MOFs can show different crystalline phases by varying temperature and pressure, and the modulator used (formic acid) is small enough to occupy coordination sites on the metal nodes preventing further coordination of the ditopic linker. However, the obtained product is not the literature one; it could either be a different phase, or a MOF with a different linker connectivity on the Zr^{IV} clusters. Unfortunately, no single crystal could be obtained from the synthesis, so it was not possible to assess the crystal structure of this material. On the other hand, these observations allow to remark the crucial importance of reaction temperature on the synthesis, as well as the autogenous pressure developed inside the autoclave.

The synthesis proposed by Xu et al. [100] has been downscaled and tried as well: benzoic acid was used as modulator, 30 eq. with respect to Zr^{IV} quantity, and 12 µL of trifluoroacetic acid in each synthesis (unless otherwise noted). Syntheses LA9-A and B share identical synthetic conditions, and yet the products obtained are slightly different: both are amorphous, even if some broad structured profile can be observed, but 9-B features a sharp peak at low angles (figure 4.16). In syntheses LA10-A-D, besides changing the Zr^{IV} precursor, DEF was used as solvent in 10-A and C, yielding amorphous products as the syntheses with DMF 10-B and D.

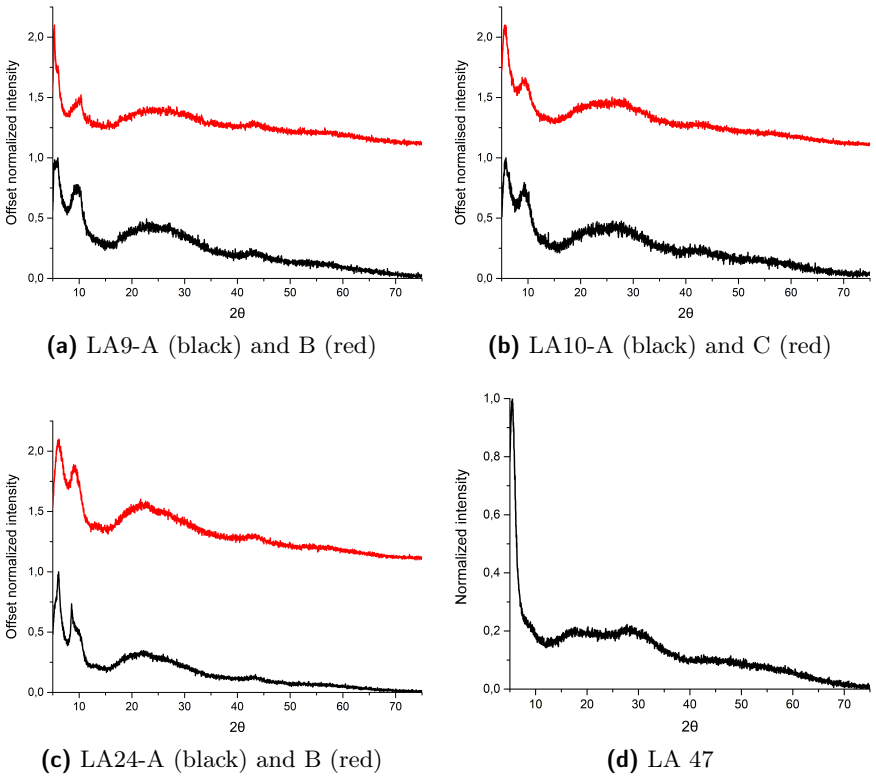

(a) LA9-A (black) and B (red)

(b) LA10-A (black) and C (red)

(c) LA24-A (black) and B (red)

(d) LA 47

Figure 4.16: Normalized p-XRD diffractograms of syntheses LA-9,10,24,47

Higher temperatures (130 °C) have been used for syntheses LA11-A,B,C,D, while lower (80 °C) for LA11-E,F. Products obtained form the first syntheses were amorphous, while from the latter only the free ligand was found. Using only trifluoroacetic acid (200 µL) as modulator yielded amorphous products both in LA24-A,B; finally, synthesis LA47 carried out in autoclave with $ZrCl_4$, benzoic and trifluoroacetic acid in the same stoichiometric ratios as proposed by Xu et al. [100] yielded a material which appears to be mostly amorphous. While showing broad signals throughout the diffractogram, one only peak could be observed at very low angles.

In the end, the synthesis of Xu et al. [100] did not yield the desired product, and even some variations in terms of concentration, stoichiometric

ratios and temperature could not provide the crystalline material reported in literature. On the other hand, a modulated synthesis with formic acid has been optimised, yielding a crystalline material containing both Zr^{IV} and H_2sdc, but the obtained product is different from the known MOF $Zr_6(\mu_3\text{-}O)_4(\mu_3\text{-}OH)_4(sdc)_6$. This material is insoluble in organic solvents and in water as well, suggesting that it is a Zr-MOF; even if no single crystal could be obtained, and thus the crystal structure could not be solved, it is reasonable to suppose that the metal nodes are the same as the known MOF, but the cluster is not 12-coordinated. In fact, formic acid is known for capping coordination sites in MOFs, resulting in a reduced coordination of polytopic linkers connecting two or more nodes[103].

4.2.3 Zr−Fe MOF syntheses

Zr^{IV} − Fe − sdc

Syntheses with Zr^{IV}, the Fe^{II} complex and H_2sdc have been summarised in table 4.4. The first experiments suggested that a crystalline material could be obtained through a M:L:Fe ratio of 4 : 4 : 1 (LA2-B); however, both acetic acid and the benzoic-trifluoroacetic acid couple were not able to modulate the synthesis properly, yielding always poorly crystalline materials. On the other hand, using formic acid as modulator yielded highly crystalline materials, both with $ZrCl_4$ and $ZrOCl_2 \cdot 8\,H_2O$ as precursors (LA41-A and C).

Products from LA41-A and C appear as pink powders, and their diffractograms are completely superimposable, suggesting that these syntheses yielded the same material. Small differences around 8° and 28° can be ascribed to a preferential orientation of the crystallites during the measurement. Same considerations can be done for LA42-B and D, which appear as red powders: the products obtained are the same, but they are not very crystalline.

Diffractograms of LA41-A and C have been compared to the experimental diffractogram of the deprotonated Fe^{II} carbene complex and the calculated powder diffraction pattern for the protonated form. While being very different from the calculated pattern for the protonated complex, the diffractograms of 41-A,C share similarities with the experimental diffraction pattern of the deprotonated complex. In particular, the peaks around 24°

Table 4.4: Syntheses of Zr^{IV} – Fe^{II} – sdc; AA = acetic acid, FA = formic acid, BA = benzoic acid

Name	**Zr^{IV} salt**	**Zr^{IV}** (mmol)	**H_2sdc** (mmol)	**Fe complex** (mmol)	**M:L:Fe ratio**	**Modulator**
LA 2-B	$ZrCl_4$	$4.29 \cdot 10^{-2}$	$4.29 \cdot 10^{-2}$	$1.07 \cdot 10^{-2}$	4 : 4 : 1	AA
LA 2-C	$ZrCl_4$	$4.29 \cdot 10^{-2}$	$4.29 \cdot 10^{-2}$	$2.14 \cdot 10^{-2}$	2 : 2 : 1	AA
LA 16	$ZrCl_4$	$4.08 \cdot 10^{-2}$	$2.04 \cdot 10^{-2}$	$2.04 \cdot 10^{-2}$	2 : 1 : 1	BA, TFA
LA 41-A	$ZrCl_4$	$4.29 \cdot 10^{-2}$	$4.29 \cdot 10^{-2}$	$1.07 \cdot 10^{-2}$	4 : 4 : 1	FA
LA 41-B	$ZrCl_4$	$4.29 \cdot 10^{-2}$	$4.29 \cdot 10^{-2}$	$1.07 \cdot 10^{-2}$	4 : 4 : 1	AA
LA 41-C	$ZrOCl_2 \cdot 8\,H_2O$	$4.29 \cdot 10^{-2}$	$4.29 \cdot 10^{-2}$	$1.07 \cdot 10^{-2}$	4 : 4 : 1	FA
LA 41-D	$ZrOCl_2 \cdot 8\,H_2O$	$4.29 \cdot 10^{-2}$	$4.29 \cdot 10^{-2}$	$1.07 \cdot 10^{-2}$	4 : 4 : 1	AA

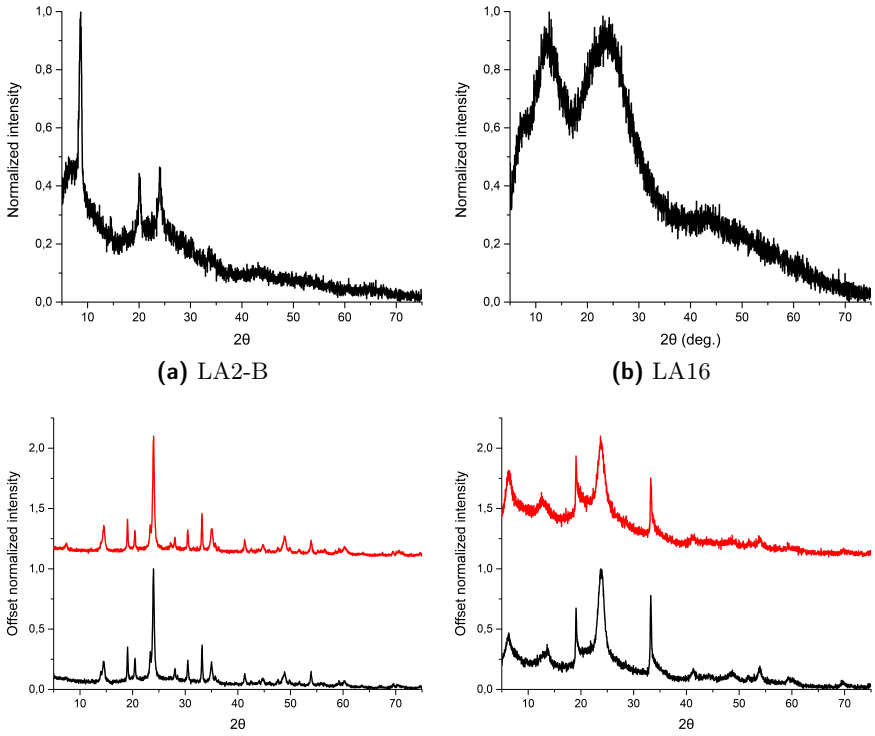

(a) LA2-B **(b)** LA16

(c) LA41-A (black) and C (red) **(d)** LA41-B (black) and D (red)

Figure 4.17: p-XRD diffractograms of the Zr−Fe−sdc syntheses

are preserved in the product, as well as the peak around 14°. These observations suggest that the obtained product are different both from the mere protonated and the deprotonated complex, but they surely contain the deprotonated complex nonetheless. Another important information is that these materials are insoluble in organic solvents and in water: overall, these observations allow us to think that a Zr-MOF with the carbene complex has been obtained.

Zr^{IV} – Fe

There is no evidence thus far that $(sdc)^{2-}$ has been incorporated into the final product; in order to shed light on this issue, syntheses with only

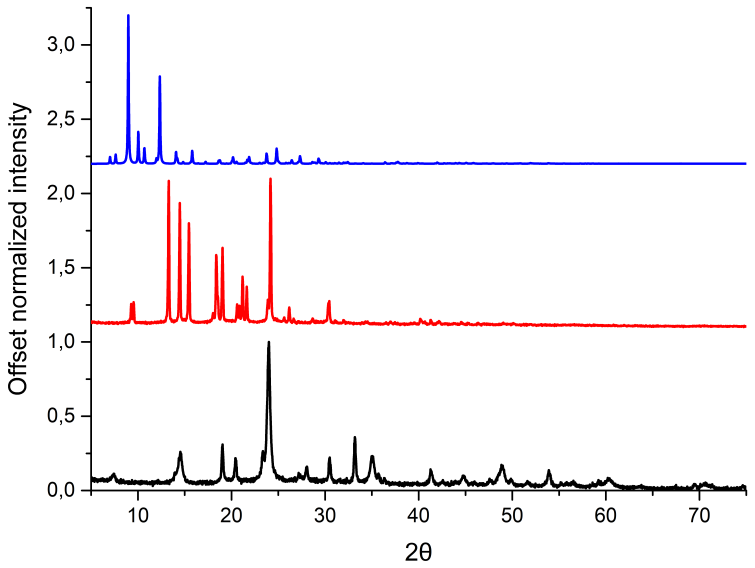

Figure 4.18: LA41-C (black), experimental (red) and calculated (blue) Fe^{II} complex

Zr^{IV} salts and Fe^{II} complex have been carried out. The syntheses and the relative details can be found in table 4.5.

All the syntheses carried out with formic acid as modulator yielded crystalline materials, while those carried out with acetic acid did not. Using a 4 : 1 Zr : Fe ratio as in LA42-A to D yielded the same products as the corresponding syntheses with H_2sdc (LA41-A to D): the pair of diffractograms are identical in the corresponding experiments (figures 4.19 and 4.20). This proves that in the LA41 series the products did not incorporate H_2sdc in their final structure, and only products with Fe^{II} the complex could be obtained.

SEM images of 42-A,E reveal that the material forms highly intergrown platelets; their dimension varies between 500 nm and 1 µm. LA42-B,D are morphologically similar, and they appear as thin foils or petals, less regular and rigid than the previous forms.

Syntheses with only Zr^{IV} and Fe^{II} complex in 2 : 1 ratio have been explored: acetic acid proved again to be an inefficient modulator, while results obtained with formic acid were interesting. Both $ZrCl_4$ and $ZrOCl_2 \cdot$

Table 4.5: Syntheses of Zr^{IV} – Fe^{II}; AA = acetic acid, FA = formic acid, BA = benzoic acid

Name	Zr^{IV} salt	Zr^{IV} (mmol)	Fe complex (mmol)	M:L:Fe ratio	Modulator
LA 42-A	$ZrCl_4$	$4.29 \cdot 10^{-2}$	$1.07 \cdot 10^{-2}$	4 : 1	FA
LA 42-B	$ZrCl_4$	$4.29 \cdot 10^{-2}$	$1.07 \cdot 10^{-2}$	4 : 1	AA
LA 42-C	$ZrOCl_2 \cdot 8\,H_2O$	$4.08 \cdot 10^{-2}$	$1.07 \cdot 10^{-2}$	4 : 1	FA
LA 42-D	$ZrOCl_2 \cdot 8\,H_2O$	$4.29 \cdot 10^{-2}$	$1.07 \cdot 10^{-2}$	4 : 1	AA
LA 42-E	$ZrCl_4$	$4.29 \cdot 10^{-2}$	$2.14 \cdot 10^{-2}$	2 : 1	FA
LA 42-F	$ZrCl_4$	$4.29 \cdot 10^{-2}$	$2.14 \cdot 10^{-2}$	2 : 1	AA
LA 42-G	$ZrOCL_2 \cdot 8\,H_2O$	$4.29 \cdot 10^{-2}$	$2.14 \cdot 10^{-2}$	2 : 1	FA
LA 42-H	$ZrOCl_2 \cdot 8\,H_2O$	$4.29 \cdot 10^{-2}$	$2.14 \cdot 10^{-2}$	2 : 1	AA
LA 68	$ZrOCl_2 \cdot 8\,H_2O$	$4.29 \cdot 10^{-2}$	$4.29 \cdot 10^{-2}$	1 : 1	FA
LA 73	$ZrCl_4$	$4.29 \cdot 10^{-2}$	$2.14 \cdot 10^{-2}$	2 : 1	FA
LA 75-A	$ZrCl_4$	$4.29 \cdot 10^{-2}$	$2.14 \cdot 10^{-2}$	2 : 1	FA, TBACl 1 M
LA 75-B	$ZrCl_4$	$4.29 \cdot 10^{-2}$	$4.29 \cdot 10^{-2}$	1 : 1	FA, TBACl 1 M
LA 75-C	$ZrOCl_2 \cdot 8\,H_2O$	$4.29 \cdot 10^{-2}$	$2.14 \cdot 10^{-2}$	2 : 1	FA, TBACl 1 M
LA 75-D	$ZrOCl_2 \cdot 8\,H_2O$	$4.29 \cdot 10^{-2}$	$4.29 \cdot 10^{-2}$	1 : 1	FA, TBACl 1 M
LA 86	$ZrCl_4$	$3.22 \cdot 10^{-1}$	$1.61 \cdot 10^{-1}$	2 : 1	FA

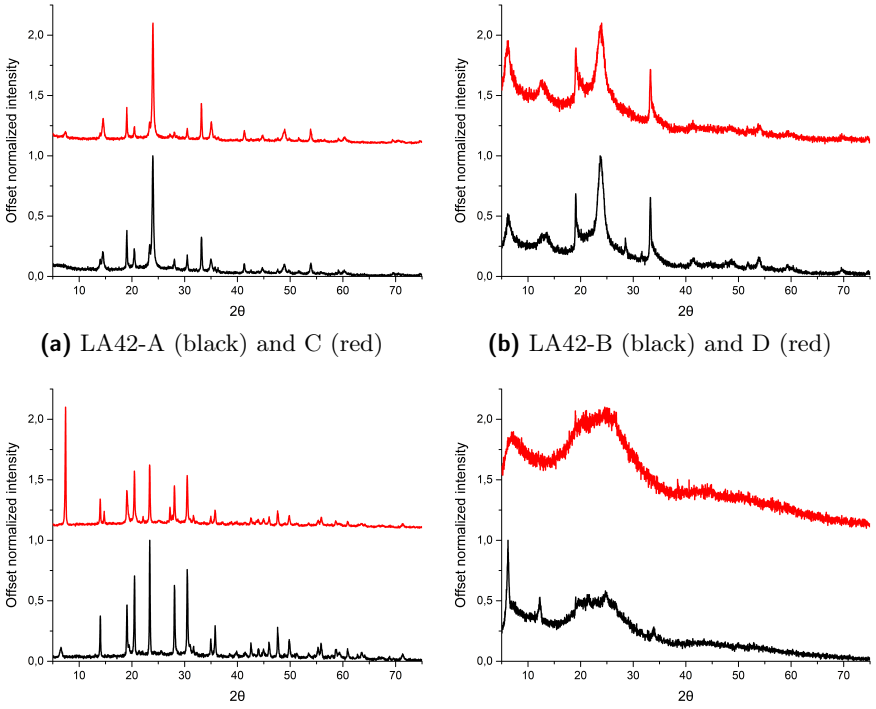

(a) LA42-A (black) and C (red)

(b) LA42-B (black) and D (red)

(c) LA42-E (black) and G (red)

(d) LA42-F (black) and H (red)

Figure 4.19: p-XRD diffractograms of LA42 syntheses

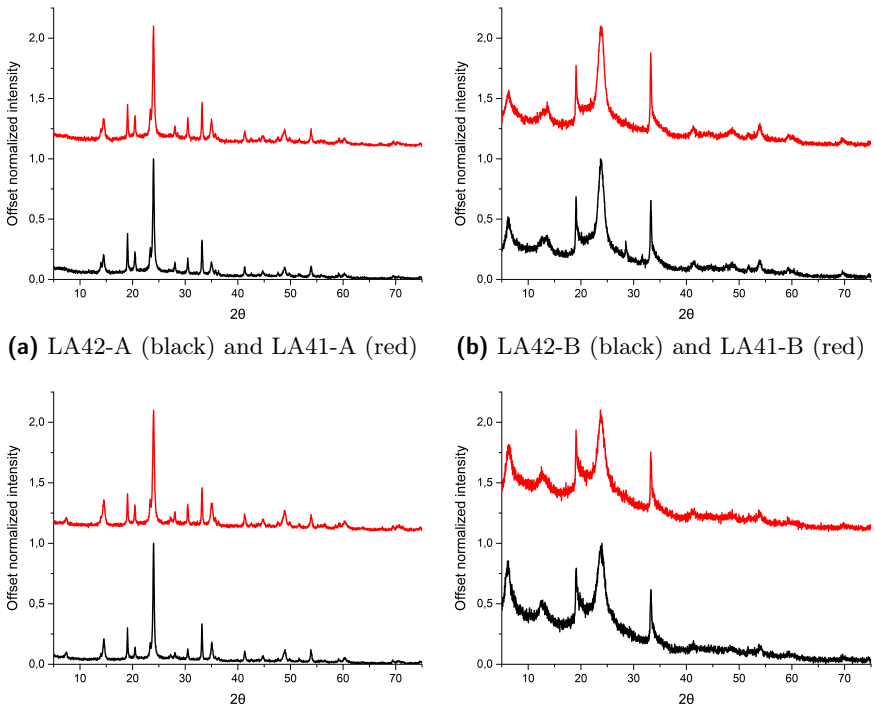

(a) LA42-A (black) and LA41-A (red)

(b) LA42-B (black) and LA41-B (red)

(c) LA42-C (black) and LA41-C (red)

(d) LA42-D (black) and LA41-D (red)

Figure 4.20: p-XRD diffractograms of LA42 syntheses and comparisons with LA41

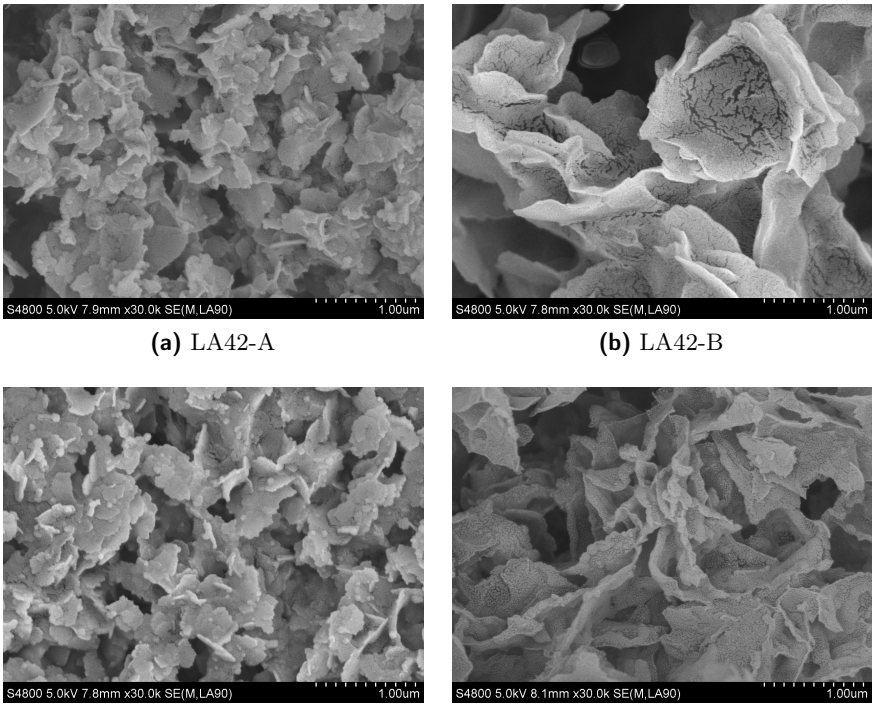

(a) LA42-A **(b)** LA42-B

(c) LA42-C **(d)** LA42-D

Figure 4.21: SEM pictures of LA42 A to D

$8\,H_2O$ yielded crystalline products with formic acid (figures 4.19 and 4.20); SEM images show small cubes whose dimensions are below 500 nm both for 42-E and 42-G, but the latter shows more aggregation of the cubes than the former. On the other hand, diffractogram of 42-G exhibits the same pattern of 42-E with extra peaks around 15° and 27°: these signals could be ascribed to the presence of another crystalline phase in the product obtained from $ZrOCl_2 \cdot 8\,H_2O$. Even if the positions of these signals resemble those of the Fe^{II} complex, these peaks can not be linked to the presence of unreacted complex, since the diffractogram does not feature its most intense signals.

A different metal to ligand ratio (M:L 1 : 1) has been used in LA68, where the reagents were directly mixed in the vial without the preparation

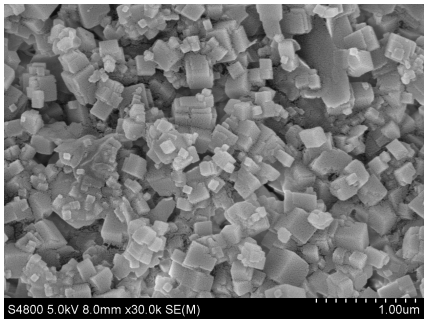

(a) LA42-E

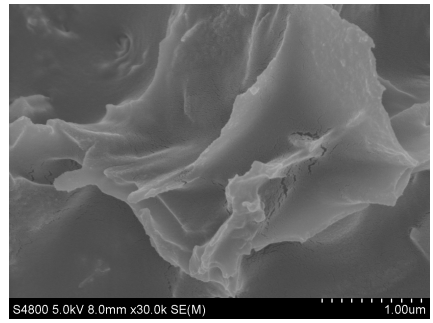

(b) LA42-F

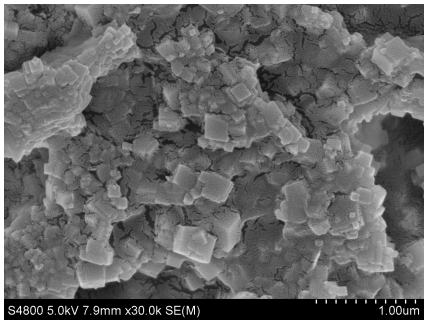

(c) LA42-G

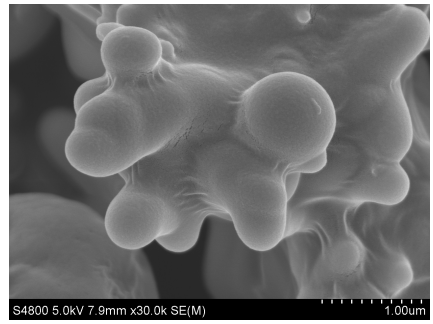

(d) LA42-H

Figure 4.22: SEM pictures of LA42 E to F

of stock solutions. A crystalline product was obtained, however its diffractogram shows more and different peaks compared to the synthesis with a 2 : 1 metal to ligand ratio (LA42-G, see figure 4.23). Albeit many signals are the same in the two diffractograms, suggesting that both syntheses share at least one common product, LA68 must at least contain another crystalline and insoluble product, which accounts for the new recorded signals from the p-XRD pattern. SEM images depict small cubes as in LA42-G, but also a sheet-like product which entangles these cubes. It appears that the latter species is the one responsible for the new peaks in the diffractogram; it is still unclear whether this phase is due to the new M:L ratio or to the direct mixing of the reagent without the preparation of stock solutions (or by both these factors).

A diluted version of 42-E was carried out in a 10 mL round bottom flask and reaction volume of 3 ml (using the same reagent quantities as 42-E). Here, stock solutions of metal salt and ligand have been used. The obtained product is crystalline (LA73), but the diffractogram is significantly different from 42-E in peak position and multiplicity both. Even the morphology is totally different from the non diluted synthesis; probably, the dilution and the use of a different reaction vessel lead to a different product. Round bottom flasks expose a different amount of surface to the reaction mixture compared to vials; moreover, the overpressure in the flask was slightly released to prevent explosion, since it was carried out in an oil bath inside a pyrex vessel. Thus, it could be argued that the increase of pressure during the reaction is important for obtaining a pure crystalline phase.

Reactions with 1:1 M:L ratio have been carried out in 6 mL vial (LA75-B,D), as well as with 2 : 1 ratio with the addition of 4 µL of a solution 1 $\mathrm{mol\,dm^{-3}}$ of tetrabuthylammonium chloride (TBACl) (LA75-A,C). Products obtained from the two different Zr^{IV} salts in a 2 : 1 ratio are the same as those obtained by the previous syntheses, even though the signal at lowest angles is absent; morphology of the products is exactly the same of the previous syntheses. Thus, it can be concluded that the addition of TBACl does not influence the formation of the desired product. Product 75-B is similar to 42-E (and thus to 75-A as well), without the low angle peak and very few differences that could be linked to preferential crystal orientation. On the other hand, 75-D exhibits more peaks in the p-XRD pattern compared to 75-C (figure 4.24); moreover, the SEM images reveal

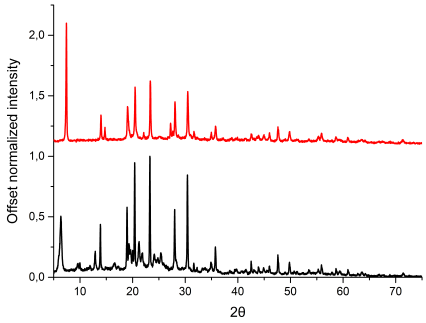

(a) Diffractograms of LA68 (black) and LA42-G (red)

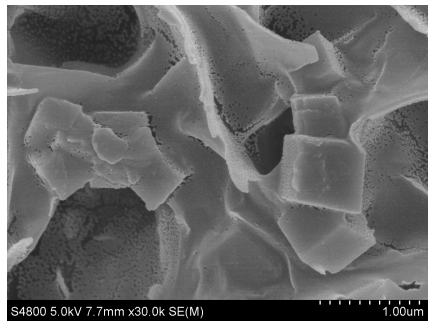

(b) SEM picture of LA68

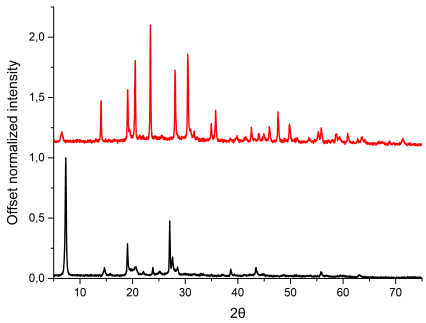

(c) Diffractograms of LA73 (black) and LA42-E (red)

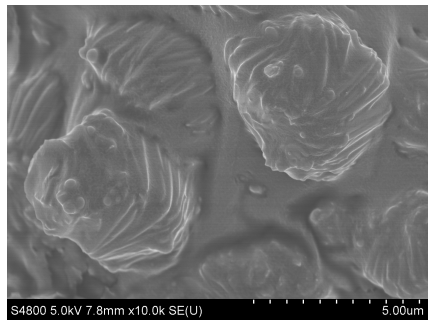

(d) SEM picture of LA73

Figure 4.23: p-XRD diffractograms and SEM of LA68 and LA73

that there are at least two different morphologies in the sample. Small cubes are found, along with some thick platelets: this observation suggests that there is another crystalline phase in the sample (figure 4.25).

Overall, a single-phase product could be obtained with $ZrCl_4$ as metal precursor, in a 2 : 1 or 1 : 1 M:L ratio. Modest differences in water content and modulator quantity do not have a strong impact on the quality and nature of the final product, while the choice of modulator surely is, formic acid being the only modulator able to yield highly crystalline products. Reaction vessel and the endogenous pressure generated during the reaction may be important factors to take account of.

An upscaled replica of LA75-A has been carried out in autoclave, but in different laboratories, using the same $ZrCl_4$ batch, formic acid of the same concentration, but DEF from a different supplier (Alfa Aesar). The retrieved product (34.2 mg) was washed with the same procedure of the other syntheses; surprisingly, the p-XRD pattern of this product shows differences compared to LA75-A. First, LA86 features a very strong signal at 6.5°, which is also the strongest of all the pattern; second, it exhibits a great number of new signals compared to LA75-A. Since it features all the peaks of 75-A, it is clear that the two syntheses share the same product, but the presence of new diffraction peaks in LA86 suggests the presence of another crystalline phase (figure 4.26). Albeit it is difficult to univocally attribute a cause for this phenomenon, several hypotheses can be made: first, the different solvent batch used could contain too much water, which may interfere with the formation of the desired product, while favouring others. Second, the temperature control and homogeneity of the oven in which the autoclave was left to react could be less precise than the oil bath, thus causing the formation of different phases in the product. On the other hand, it is reasonable to assess that the secondary product could be another MOF built on the same units of the other one, since both are insoluble in the same solvents and the overall colour of the final product is the same as that of the previous products. A different phase built with Zr^{IV} and Zr^{IV} could have a different connectivity on the metal nodes, thus resulting in a more or less expanded structure and in a different p-XRD pattern. Although the structure should be slightly different, the spectroscopic properties of the two phases should not change dramatically nonetheless, since they are made out of the same units. To test this hypothesis, a spectroscopic study

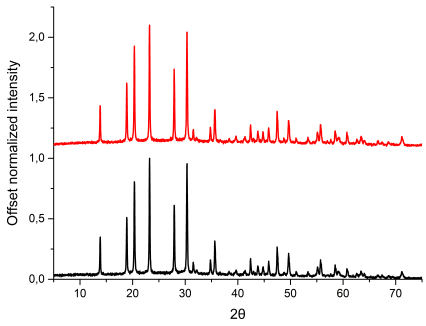

(a) LA75-A (black) and C (red)

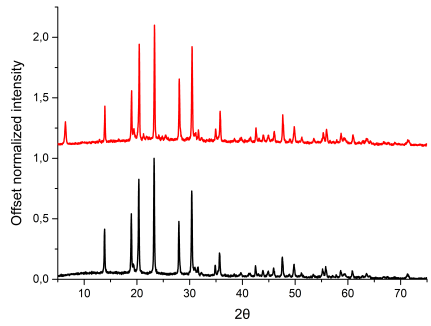

(b) LA75-B (black) and D (red)

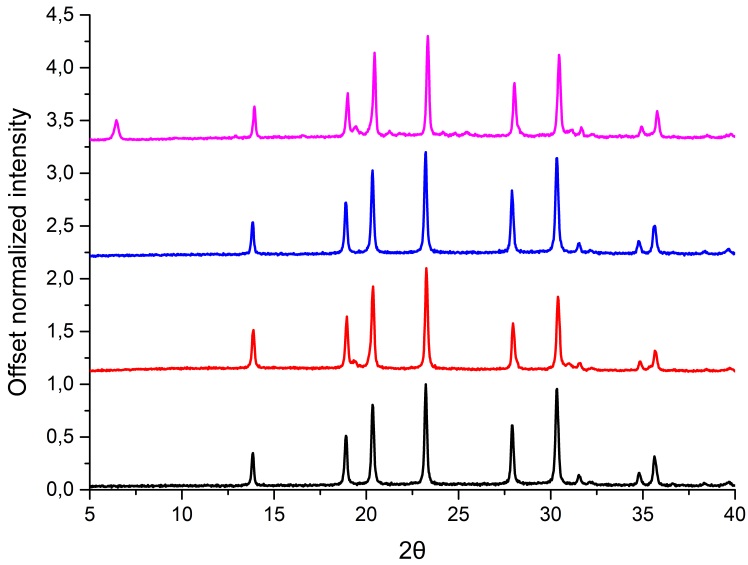

(c) Detail of LA75-A (black), B (red), C (blue) and D (violet)

Figure 4.24: p-XRD diffractograms of LA75 syntheses

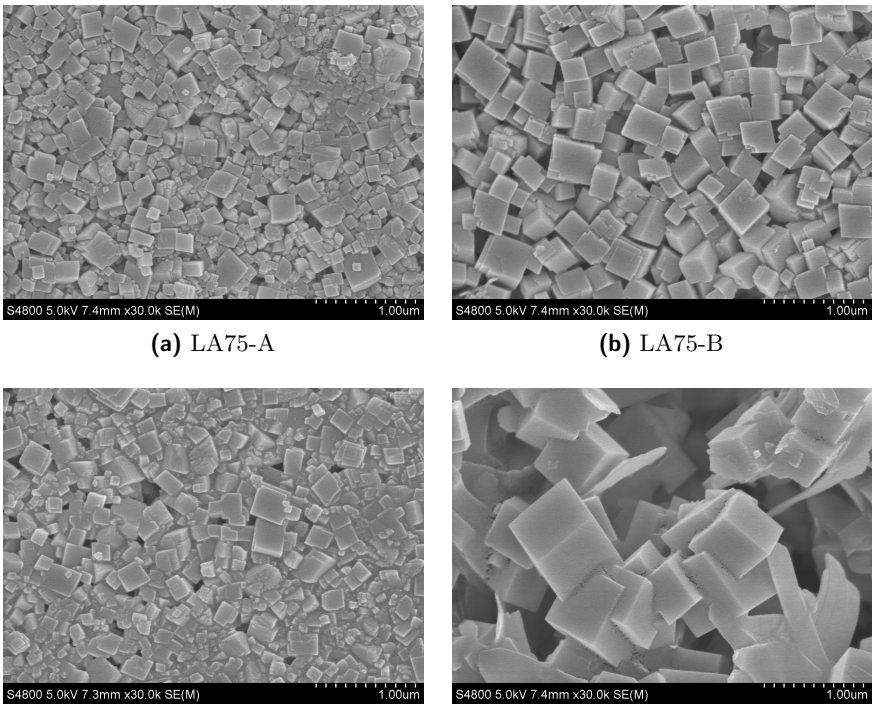

(a) LA75-A **(b)** LA75-B

(c) LA75-C **(d)** LA75-D

Figure 4.25: SEM images of LA75 syntheses

has been carried out, to verify whether the pure material (LA75-A) and the mixture (LA86) share the same behaviour or not.

4.2.4 Spectroscopic characterisation of LA75-A and LA86

Micro-Raman spectroscopy

Micro-Raman spectroscopy was performed on LA75-A and LA86, to investigate possible differences in spectroscopic behaviour between the pure product and the MOF mixture. Spectra were recorded between 800 and 1000 cm^{-1}, and for both LA-75A and LA86 the same peaks can be observed in the same spectral positions. In fact, the spectra of these two products are completely superimposable over all the examined spectral range (figure 4.27). Spectra were taken on different spots of the powder sample, to ensure representativity for both products and to ensure an averaged sampling among the possible phases of LA86: since all the spectra recorded for LA75-A and LA86 are completely superimposable, it can be concluded that the different phases in LA86 share the same spectroscopic behaviour of the pure product LA75-A. Moreover, the Raman signals recorded for the two products match those of the deprotonated Fe^{II} carbene complex: both LA75-A and LA86 have signals at 1620, 1127, 985, 542 and 370 cm^{-1}, and the complex has its strongest signals in the same positions. This observation proves not only that the complex is present in both LA75-A and LA86, but also that it is preserved in the final products without being decomposed during the synthetic procedure.

On the other hand, only in LA86 a few small red spots could be observed at the microscope; micro-Raman spectra of these parts yields the vibrational pattern of haematite, Fe_2O_3 (table 4.6). However, hematite is present only in very small amount, since its diffraction pattern could not be observed through p-XRD analyses and the red spots in the product were low in number. Micro-Raman spectroscopy was also useful to exclude the presence of Zirconia in the product: the spectra of monoclinic and tetragonal Zirconia have lattice vibrations whose signals lie at low wavenumbers, all below 1000 cm^{-1} (see table 4.7). These signals are absent in spectra of the products, thus proving that they do not contain ZrO_2.

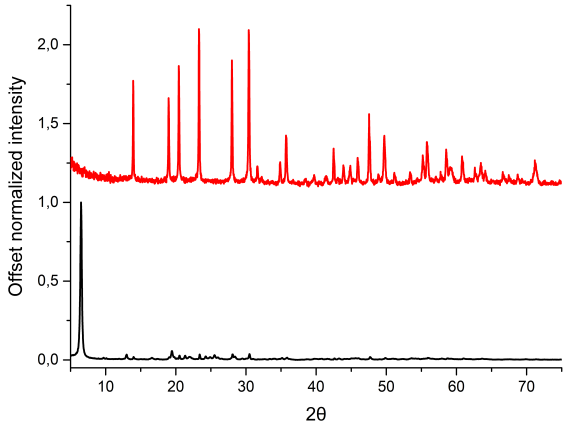

(a) LA86 (black) and LA75-A (red)

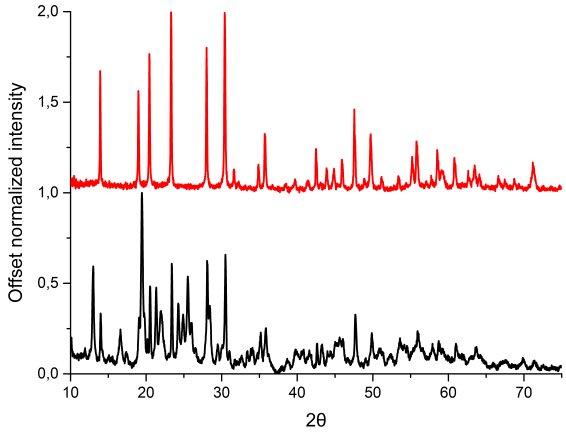

(b) Detail of the $10° - 75°$ range; intensity maximised to ease the comparison

Figure 4.26: Comparison between diffractograms of LA86 and LA75-A

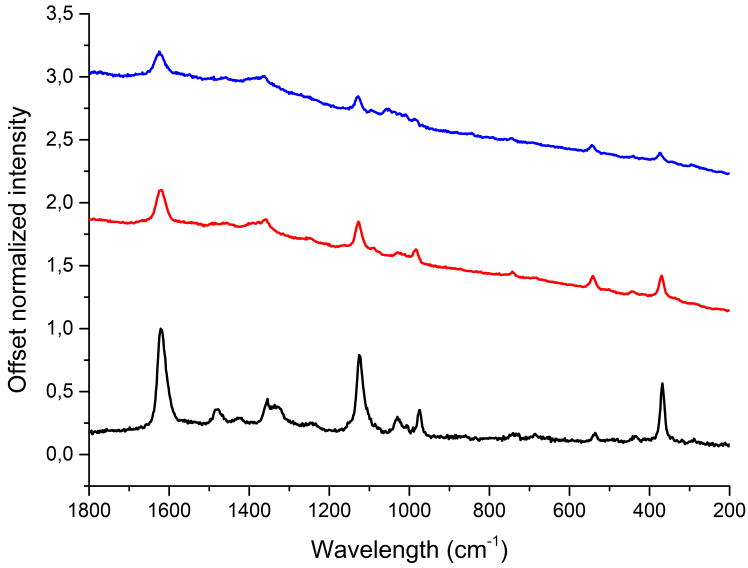

Figure 4.27: Micro-Raman spectra of Fe^{II} deprotonated complex (black), LA75-A (red) and LA86 (blue)

Table 4.6: Raman modes of haematite in LA86

Experimental (cm^{-1})	Haematite [104] (cm^{-1}) (RUFF ID R040024)
220	227
287	293
398	412

Table 4.7: Phonon modes of monoclinic and tetragonal Zirconia. From [105, 106]

m-ZrO_2 (cm^{-1})	t-ZrO_2 (cm^{-1})
103	145
177	264
189	320
222	460
305	606
331	641
343	-
376	-
473	-
498	-
534	-
613	-
633	-

X-ray fluorescence spectroscopy

XRF spectroscopy measurements were carried out to assess the presence of both Zr and Fe in LA86. The analysis was carried out on the powder sample; spectral lines of Zr and Fe were found, and since no superimposition with spectral lines of other elements was detected, the presence of these two metals can be univocally assessed. Concerning their quantification, the instrument yields values according to an internal calibration, thus the data can be evaluated only qualitatively. The atomic ratio between Zr and Fe was found to be around 14 : 1, which is quite surprising, since the value exceeds by far the 2 : 1 ratio used during the synthesis. Moreover, this datum does not agree with the fact that the syntheses with a 1 : 1 Zr:Fe ratio yielded twice the product of those with a 2 : 1 ratio, which suggested that the final product could contain nearly the same amount of Zr and Fe.

Even if XRF detects also P in high quantities (3.5% in weight), it is not possible to confirm its presence in the sample, since K lines of P are found at the same energy as L lines of Zr. It is worthy to note that, since the the Fe^{II} complex was used as hexafluorophosphate salt, the latter anion

could be present in the final Zr-based material, but this method does not allow to confirm this hypothesis.

UV-Vis diffuse reflectance spectroscopy and fluorimetry

Diffuse reflectance measurements were carried out on the pure sample without dilution. In the near IR region the reflectance is around 70%, and decreases gradually while approaching the visible light range. Absolute reflectance minima are found at 505, 384 and 260 nm, the latter being the centre of a very broad transition starting around 330 nm and ending in the UV range of the spectrum (figure 4.28). Zr^{IV} does not provide electronic transitions in the visible range, since its free unoccupied orbitals lie at energies too high for a possible electron transfer from the metallo-ligand molecules: thus, the transitions observed for this Zr−Fe material are those of the Fe^{II} carbene complex. However, the transitions observed in LA86 are slightly shifted to higher energies compared to those of the free complex, while the one at 260 nm is common in both the complex and the Zr−Fe product (see table 4.8). The lowest energy transition in the free complex is broader, and has two shoulders around 564 and 660 nm, while Zr−Fe product completely lacks this structured absorption profile; furthermore, the relative intensity of the two transitions centred at 505 and 384 nm versus the 260 nm band is notably decreased in LA86 compared to the free complex. This phenomenon is very similar to the one reported for the $[Ru(pytpy)]^{2+}$ complex in the Zn-based MOF [55]; the reason why only the low energy two bands are less intense in the Zr−Fe product could be manifold, but it could be speculated that it is a result of the new environment around the complex when it is bound to Zr^{IV}. Even if dramatic changes in the geometry of the Fe^{II} carbene complex are not expected, slight distortions of the symmetry could result in a decrease of intensity of these bands. Even the small shifts in the energy of these charge transfer bands could be ascribed to the change in the chemical environment around the Fe^{II} complex, or to the more ordered alignment of the complex inside the final material, leading to a partial overlap of the orbitals on different molecules involved in the transition. On the other hand, not only the band at 260 nm is more intense in the Zr−Fe product, but it is also broader, and has an inflection point at 316 nm. Even in this case, the broadness associated to this band may be the result of an increased overlap between molecular

Table 4.8: Diffuse reflectance minima of complex **3** and LA86

Complex **3** (nm)	LA86 (nm)
260	260
410	384
522	505

orbitals of different molecules, which could be enhanced by an ordered disposition inside the final material: while the nature of the electronic transition remains unaltered, the positive overlap results in a lowering of the transition energies, which is seen in electronic spectrum as a broad tail at the right of the main absorption band.

It is worthy to note that these considerations are based on an extension of the molecular orbital approach to the solid state, and thus are limited to a general description of the electronic properties; to gain better insights on the phenomena observed in these systems, a detailed crystal structure would be necessary, so that a solid state approach could be used to better understand the observations.

Solid state UV-Vis fluorescence measurements on LA86 did not reveal any emission from the sample: exciting wavelength used for the experiments were the reflectance minima in table 4.8.

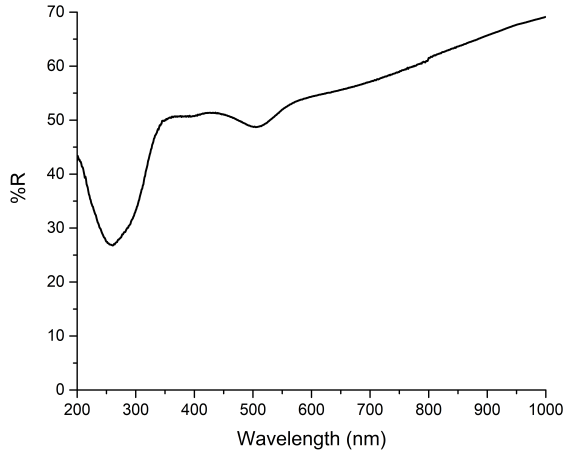

(a) Reflectance

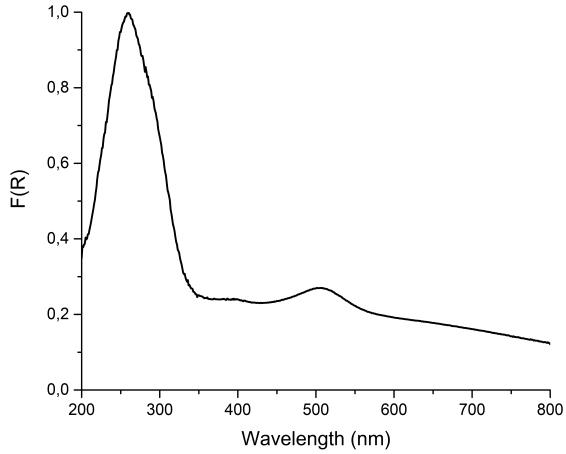

(b) Kubelka-Munk

Figure 4.28: Solid state UV-Vis spectra of LA86

Chapter 5

Photocatalytic measurements

As already stated, the longer is the lifetime of an excited state, the higher are the pobabilities of observing the properties and the reactivity of a photoexcited molecule. Whether luminescence or photo-driven reactions are studied, long lived excited states are usually required to observe the effects of the processes involved; Ru^{II} or Cr^{III} polypyridyl complexes, for example, feature excited states with high lifetimes, and they find applications as light emitters and in photocatalysis. On the other hand, even if Fe^{II} complexes suffer from short lived excited state and have limited applications in these fields, it has been demonstrated that Fe^{II}-NHC complexes can engage in intermolecular photoinduced electron transfer: complex **3** proved to be effective in the photoinjection of one electron from the Fe^{II} ion into the conduction band of TiO_2. There are three key factors related to this phenomenon:

1. Photoredox potentials of complex **3**
2. Energetic match between photoexcited electron and TiO_2 conduction band
3. The timescale of the photoinjection

Photo-oxidation (1.9) and photo-reduction (1.10) potentials for excited state molecules and complexes have already been discussed in section 1.1.1: usually, molecules in their excited states are both good photo-reductants and photo-oxidants. Using equations 1.9 and 1.10, one can

estimate the excited state redox potentials; however, while ground state (GS) oxidation and reduction potentials for complex **3** are known from experimental measurements reported in the literature ($E_{ox}^{GS} = 0.85$ V, $E_{red}^{GS} = -1.35$ V) [36], the $E_{00}(A^*/A)$ term is not known, nor it can be obtained experimentally, since the complex is non-luminescent. On the other hand, literature provides TD-DFT calculations on excited states of complex **3** [107], which positioned the energy of the ^{3}MLCT state at 1.40 eV. Thus, the photoredox potentials can be calculated:

$$E_{ox}^{0} = 0.85 - 1.40 = -0.55\text{V}$$

$$E_{red}^{0} = -1.35 + 1.40 = +0.05\text{V}$$

As explained in 1.1.1, these photoredox potentials refer to *reduction* semi-reaction of the excited state species; thus, E°_{ox} and E°_{red} refer to the following semi-reactions, respectively (ligands have been omitted for better clarity):

$$Fe^{3+} + e^- \longrightarrow {}^*Fe^{2+} \qquad -0.55\,\text{V} \qquad \{7\}$$

$${}^*Fe^{2+} + e^- \longrightarrow Fe^{+} \qquad +0.05\,\text{V} \qquad \{8\}$$

It is thus clear that complex **3** is a weak photo-oxidant, since the photo-reduction potential is very low (reaction 8), while it can be a good photo-reductant (reaction 7). For understanding the photo-reducing power of the complex, it is more convenient to write the *oxidation* semi-reaction, by reversing reaction 7 along with the sign of the associated potential:

$${}^*Fe^{2+} \longrightarrow Fe^{3+} + e^- \qquad +0.55\,\text{V} \qquad \{9\}$$

The complex in its excited state should be a better reductant than in the ground state, oxidising to Fe^{III}. However, to efficiently transfer the photoexcited electron on TiO_2, a good overlap between orbitals of the complex and the conduction band of the metal oxide is required, as well as a proper energetic matching between the unoccupied orbital of the photoexcited species and the conduction band of the oxide. Harlang et al.

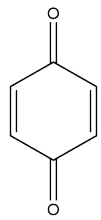

Figure 5.1: 1,4-benzoquinone

[37] demonstrated that both of these requirements are fulfilled; moreover, they explain that even if the ^{3}MLCT state has a lifetime of nearly 16 ps, the timescale of the photoinjection is comparable to the lifetime of the photoexcitation, and has been measured to be 3.1 ± 0.7 ps.

As far as photocatalysis is concerned, the thermodynamic considerations depicted so far suggest that complex **3** may be able to reduce molecules with reduction potentials higher than -0.55 V; the main issue remains the short ^{3}MLCT lifetimes of the Fe^{II} complex. The non-radiative deactivation pathways could prevent effective electron transfer to the substrate, and no photocatalysis would be observed. To the best of our knowledge, to date there are no works in the literature about photocatalysis of Fe-NHC complexes, neither in homogeneous phase nor in heterogeneous phase (e.g. complexes supported on Al_2O_3 or TiO_2). Since the synthesised Fe-NHC complex should exhibit photo-reducing properties, we designed a reaction with an organic molecule, whose ground state redox potential could match the one of the complex. The molecule 1,4-benzoquinone (BQ) (figure 5.1) was selected as ideal candidate for testing the photoactivity of complex **3**, since it has the first one-electron reduction potential of -0.22 V [108], and could theoretically be reduced by complex **3**. Moreover, 1,4-benzoquinone only absorbs in the UV range, so the photoreaction with Fe^{II}-NHC complex can be carried out in the visible range, where MLCT transition lies, without any interference from UV initiated photoprocesses of benzoquinone [109].

In order to assess the photoactivity of complex **3** alone and of the Zr-MOF incorporating the complex, we carried out photoreactions with 1,4-benzoquinone (BQ), irradiating solutions with green light and analysing over regular periods of time the reaction through high-performance liquid chromatography (HPLC), as discussed in the next sections.

5.1 Materials and methods

For the metal complex, two solutions were prepared, one in deionised water and one in $HClO_4$ 0.01 M (pH =2); both the solutions were $3.0 \cdot 10^{-5}$ M in complex **3** and 0.1 mM in 1,4-benzoquinone. For the MOF, product **LA86** was used: 8.5 mg of MOF were put in a 25 mL graduated flask; 25 µL of a 0.1 mM solution of 1,4-benzoquinone were added, then the volume was adjusted to 25 mL with deionised water. The final concentration of 1,4-benzoquinone was 0.1 mM. Reactions were carried out in cylindrical Pyrex glass cells (6 cm diameter), on a volume of 20 mL; for the MOF suspension, sonication for 10 mL was performed, until a stable suspension could be observed. All the solutions were degassed under a N_2 stream for 10 min before irradiation. Solutions were irradiated for 2 h with a green led ($\lambda_{max} = 530$ nm; irradiation range from 460 to 640 nm); the photoreactor was kept at 6.5 cm from the lamp, the measured irradiance being $1.83 \cdot 10^3$ µWcm^{-2} in the $450 - 650$ nm range (figure A.15).

Each solution was sampled every 15 min of irradiation, taking about 0.5 mL with a syringe and pumping into the reaction vessel the same amount of volume of N_2 with a gas-tight syringe, to prevent oxygen contamination. For reactions with MOF, each sampled solution was filtered with syringe filters in PTFE (pore size 0.4 µm) and collected in vials, which were stored in the fridge, at dark, before the analysis. A t_0 sample was taken for each synthesis, that is the solution before any irradiation with visible light; for MOF synthesis, two additional samples were taken after 30 and 45 min of mixing, *before* irradiation, to assess the degree of adsorption of reagents into the pores or at the surface of the material.

HPLC determination of 1,4-benzoquinone has been carried out with an Agilent Technologies HPLC chromatograph 1200 Series equipped with a diode array detector, binary gradient high-pressure pump and an automatic sampler. Isocratic elution was carried out with a mixture of 20/80 acetonitrile/formic acid aqueous solution (0.1 % w/v), flow rate 0.2 mL $\cdot$ min^{-1}, injection volume 20 µL. The column used was a Kinetex C18 150-2 (150 mm length, 2 mm diameter Phenomenex), packed with 2.6 µm core-shell stationary phase. Benzoquinone elution was monitored by checking the absorbance at 240 nm, while the Fe^{II} complex was better observed at 500 nm.

For reactions with Fe^{II} complex, data have been plotted as the ratio

between the integrated area of benzoquinone elution peak at each time and the integrated area at t_0 versus time. For the reaction with the MOF, the ratio between the integrated area of benzoquinone at each time and the area of the benzoquinone eluted after 45 min in dark was plotted versus time.

5.2 Results

5.2.1 Photocatalytic trials with Fe^{II} complex

HPLC analyses of t_0 samples revealed that 1,4-benzoquinone eluted at around 5 min, while complex **3** eluted around 12 min. No significant variation in the concentration of benzoquinone has been detected: plotting the ratio between the integrated area of the benzoquinone peak in each chromatogram and the integrated area at the respective t_0 ($S(t)/S(t_0)$) versus the time elapsed, small oscillations can be detected, up to 2% of the total amount of benzoquinone (figure 5.2). However, these variations can be ascribed to experimental error, since they are very small and they do not follow a particular trend. It can be nonetheless noted that after 2 h of irradiation, the amount of benzoquinone eluted is systematically lower than the one at t_0, around 2% of the starting amount: this very small variation is found both in the photo-reaction at uncontrolled pHand pH=2, and may be attributed to a certain degree of volatility of 1,4-benzoquinone, which fills the headspace of the cell. Moreover, no other peaks ascribable to other products of the photoreaction could be observed, suggesting that no photoreaction is occurring. It can thus be concluded that the Fe^{II}-NHC complex is not able to promote the photoreduction of benzoquinone in the experimental conditions adopted.

5.2.2 Photocatalytic trials with Zr−Fe MOF

Before irradiation, the suspension with MOF was kept under stirring for 45 minutes, and sampled two times, to check if some adsorption of benzoquinone occurred; a reduction of less than 1% of the signal was recorded, thus suggesting that no significant adsorption occurs. Moreover, during this "dark" phase the solution does not contain any trace of the metal complex, confirming the stability of the synthesised framework.

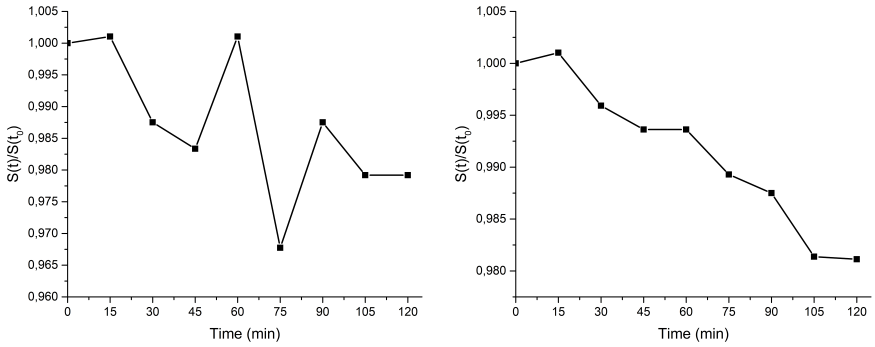

(a) At pH 2 **(b)** Uncontrolled pH

Figure 5.2: Plots for the photo-reactions with complex **3**

The results of the irradiation are plotted in figure 5.3; here, the integrated area for each point has been averaged to t_2d, which is the area of benzoquinone eluted from the suspension kept in a dark place for 45 min. Besides the point collected at 60 min irradiation time, the amount of benzoquinone eluted diminishes gradually over time: the last point (120 min) exhibit about 7.7% reduction of the benzoquinone concentration compared to the starting point. The value recorded at 60 min irradiation time should be discarded, since the sudden drop in the recorded signal does not agree with the general trend observed, and does not have any physical and chemical sense. It is highly probable that an experimental error affected that measurement, most probably during the sampling operation.

Even after 2 h of irradiation time, no trace of Fe^{II} complex was detected, confirming the excellent photo-stability of the MOF in aqueous suspensions even under irradiation. The observed reduction in benzoquinone eluted after 120 min of irradiation is surely greater than the one observed for the solutions previously discussed; however, even in this case it was not possible to detect any other organic compound besides benzoquinone. While the latter consideration may suggest that no photoreduction occurred, here the decrease of benzoquinone is more significant than in the homogeneous phase reactions; moreover, since the amount of sampled point is the same in all reactions, we could speculate that in this case the hypothesis of volatility of benzoquinone in aqueous solutions is not valid. If the observed

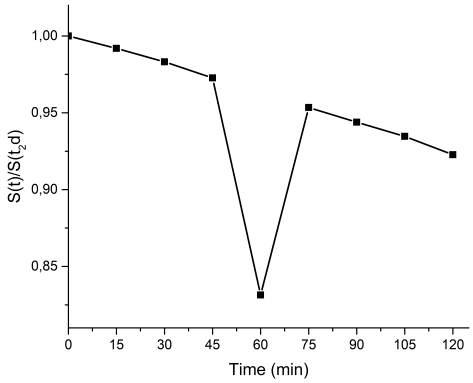

Figure 5.3: Plots for the photo-reaction with MOF

decrease in benzoquinone was ascribed only to its volatility, we would have observed the same decrease even in the reactions with MOF. It could thus be concluded that a different behaviour is observed in the photo-reduction of benzoquinone between homogeneous (the Fe^{II} complex in solution) and heterogeneous phase (MOF with Fe^{II} complex), and it is linked to the different behaviour of the Fe^{II} complex when inside a metal-organic framework. However, we still can not say whether this effect can be univocally attributed to an effective elongation ^{3}MLCT excited state lifetime or to other effects arising from the incorporation of the metal complex into a MOF.

Chapter 6

Conclusions

The exhaustive analysis of recent literature shed light on the recent works and efforts in Earth abundant metal complex photochemistry; different electron configurations have been examined, highlighting both the advantages and drawbacks of different systems. We discussed in detail the case of Fe^{II} complexes, with their drawbacks and limitations, focusing on the problem of their short excited state lifetimes, and on the recent literature adressing this issue: all the analysed strategies aimed to stabilise MLCT and destabilise MC states by increasing ligand field strength on Fe^{II}, resulting in a molecular based approach. Thus, we developed the idea of exploiting the interesting advantages of metal-organic frameworks as potential scaffolds for hosting a Fe^{II} complex. While the concept of binding a metallo-ligand with luminescent or photocatalytic properties to a MOF is not new, we pointed out that the effects on the photochemical and photophysical properties of a metal complex inside a MOF is still not very defined and completely predictable; however, we provided evidence of some successful studies, in which the incorporation of a luminophore into a MOF could extend the excited state lifetime of the emissive state.

We then designed a new ligand able to provide both a strong field on Fe^{II} and functional groups for further bonding with other metals. The attempted syntheses could not afford the desired product, probably because of the low reactivity of the reagents; however, we were able to provide a computational characterisation of the ligand and the corresponding homoleptic complex with Fe^{II}. Focusing our attention on NHC ligands,

we replicated the literature synthesis of 2,6-bis(3-methylimidazolium-1-yl)pyridine-4-carboxylic acid bis-hexafluorophosphate and its homoleptic complex with Fe^{II}, and provided a better computational characterisation with TPSSh functional. The successful upscale of the reaction allowed the use of the Fe^{II} complex as metallo-ligand in MOF syntheses; the Fe^{II}-NHC complex was stable in different solvents, in acidic and basic solutions and in a wide temperature range, thus being compatible with the synthetic requirements of different MOFs.

The mixed ligand approach was adopted for the synthesis of Zn-based MOFs: 2,6-naphtalenedicarboxylic and 4,4'-stilbenedicarboxylic acid were used along with the Fe^{II}-NHC complex. For both Zn−ndc−Fe and Zn−sdc−Fe systems big crystals were obtained, but in both cases they faded very quickly: outside the mother liquor, solvent loss rapidly results in colour loss and pulverization of the samples, and loss of crystallinity has been confirmed through p-XRD. Vibrational spectroscopy suggested that both the complex and the dicarboxylic acids were present in the final products, proving that mixed-ligand materials with Zn^{II} can be obtained both with polytopic acids with the same length as Fe^{II}-NHC complex (e.g. H_2sdc) and with shorter ones (e.g. H_2ndc).

The same synthetic approach was used for Zr-based MOFs, combined with modulated synthesis; we proved that mixed ligand systems could not be obtained with Zr^{IV}, whereas only the Fe^{II}-NHC complex could be incorporated into a crystalline material. The obtained products showed high thermal and chemical stability, and they preserved crystallinity after drying and solvent exchange. Even if the crystal structure of the resulting Zr-based material could not be solved, we proved through vibrational and electron spectroscopy that the Fe^{II}-NHC complex is successfully incorporated in the final structure, and preserves its electronic UV-Vis transitions in the final material. The huge amount of syntheses provided enough data to depict the synthetic methodology that provides the highest crystallinity; on the other hand, we highlight issues concerning the reproducibility of the synthesis, mostly concerning phase purity. Even if the material can always be synthesised through the reported procedure and has been obtained several times as a pure crystalline phase, we found that other crystalline phases with Zr^{IV} and Fe^{II}-NHC complex could be obtained as well in a few syntheses.

Lastly, we reported the results of photoreaction of the complex and the MOF with 1,4-benzoquinone: to the best of our knowledge, this is one of the first attempts in testing photoredox reactivity of Fe^{II}-NHC complexes. As expected, we observed that no photoreaction occurred for Fe^{II}-NHC complex solutions when irradiated in the green part of the visible spectrum: excited state lifetimes are too low to allow photoinduced electron transfer from the complex to the organic molecule. The small decrease in benzoquinone concentration may be linked to experimental error and to loss of reagent due to its modest volatility; formation of other products was not observed. Concerning the photoreactivity of the MOF, we first proved that the material is stable in aqueous suspensions, even under irradiation, since no quantitative release of complex was detected during HPLC analyses. Moreover, we observed a slight decrease in benzoquinone concentration over time, around 7.7%: while we did not detect any reaction product, which could have clearly demonstrated the occurrence of a photo-driven reaction, we confidently excluded that the observed decrease in benzoquinone under irradiation is ascribed to experimental error or to the volatility of the organic compound. The data gathered thus far assess that the modest decrease in benzoquinone concentration can occur only with the MOF irradiated with green light, at the absorption wavelength of the incorporated metal complex: this leads us to think that an improvement in the photochemical and photophysical properties of Fe^{II}-NHC complex occurred after the incorporation into a MOF.

On the other hand, a clear and direct correlation between the positive photocatalytic effect and the increase in ^{3}MLCT excited state lifetime for the complex can not be proved by the data collected thus far. First, further evidence concerning the photo-reduction of 1,4-benzoquinone is required, such as the identification of possible reaction products: if a photo-driven process can be proved and characterised, then the lifetimes issues can be adressed and discussed. Second, we argue that an indirect measurement, such as the assessment of the catalytic activity, may not the best way to demonstrate and evaluate the elongation of excited state lifetimes within this MOF, especially since the expected lifetime elongation may be too modest to decree a dramatic enhancement in photocatalytic activity. Therefore, a technique able to detect changes in the picosecond time scale, such as transient absorption spectroscopy, should be used for

studying the excited state. To the best of our knowledge, the techniques adopted so far by chemists for investigating lifetimes of non emissive excited states are limited to liquid solutions, or to thin films, where an absorbance can still be measured. No diffuse reflectance setup has been reported in literature for studying transient absorption on powder samples, and this limits the investigations which can be carried out on the systems synthesised in this work. A possible way to overcome this issue would be to set up a synthetic procedure yielding a thin film of the MOF, or to press the obtained powder to form a thin pellet, so that transmittance measurements can be carried out. However, setting up a synthetic method for thin films of Zr-MOFs can be quite hard, given the synthetic requirements for these materials; moreover, pressing the obtained powders in a pellet may bring defects or even destroy the local structure of the MOF, thus invalidating the measurements on it. To the best of our knowledge, evaluating the increase of lifetimes in non-emissive MOFs still remains a very difficult and challenging topic, since no standard procedure and instrumentation exist yet.

To conclude, the results obtained in this work help providing a more complete panorama of the inorganic synthesis of MOFs with NHC metalloligands, yielding a complete synthetic methodology and strategy for achieving highly crystalline products. Although still unclear, a correlation between the incorporation of a Fe^{II} complex into a MOF and the enhancement in its photo-reducing properties has been highlighted: hopefully, this positive result represents a novel strategy for improving photochemical and photophysical properties of an Earth abundant metal complex. By adressing the major challenges, both for the synthesis and the characterisation part, we hope to have paved the way for future works in this exciting field, which we strongly believe worthy of attention and efforts.

Appendix A

Supplementary figures

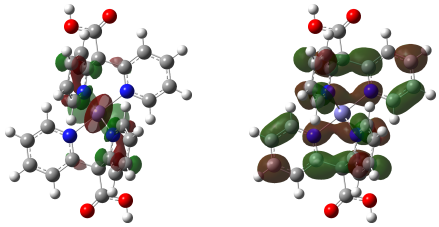

(a) HOMO **(b)** LUMO

Figure A.1: NTO for state 7 in $[Fe(tpa)_2]^{2+}$

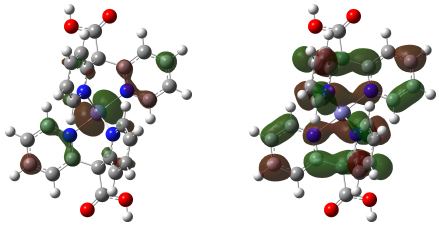

(a) HOMO **(b)** LUMO

Figure A.2: NTO for state 8 in $[Fe(tpa)_2]^{2+}$

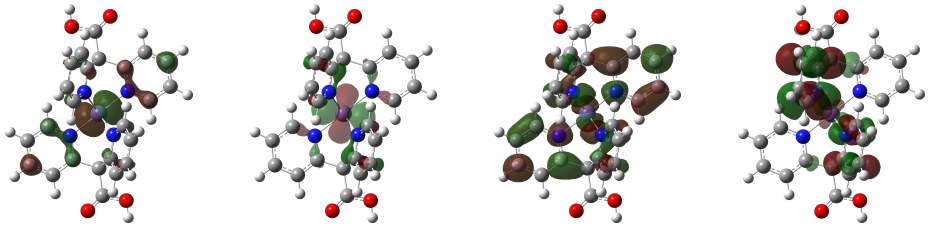

(a) HOMO-1 **(b)** HOMO **(c)** LUMO **(d)** LUMO+1

Figure A.3: NTO for state 11 in $[Fe(tpa)_2]^{2+}$

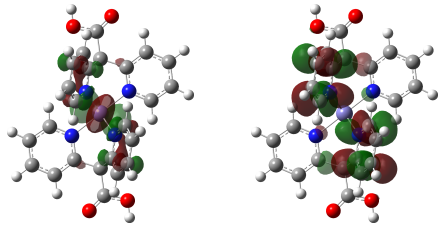

(a) HOMO **(b)** LUMO

Figure A.4: NTO for state 13 in $[Fe(tpa)_2]^{2+}$

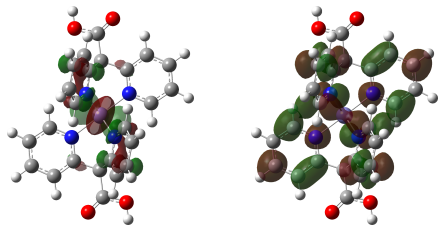

(a) HOMO **(b)** LUMO

Figure A.5: NTO for state 16 in $[Fe(tpa)_2]^{2+}$

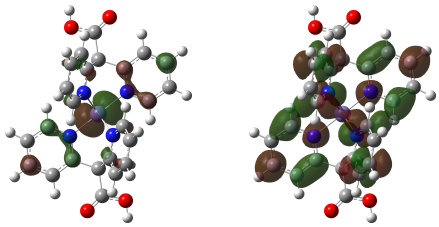

(a) HOMO **(b)** LUMO

Figure A.6: NTO for state 17 in $[Fe(tpa)_2]^{2+}$

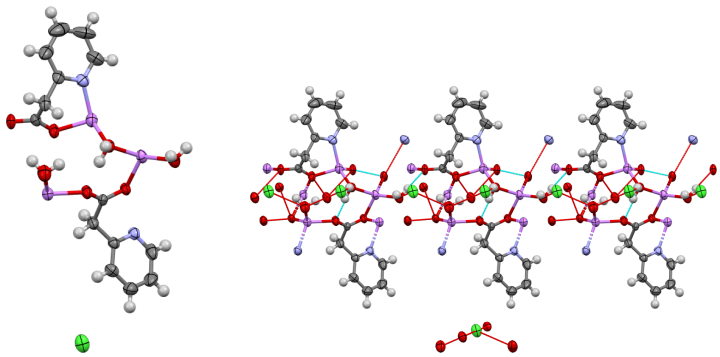

(a) Asymmetric unit along axis b **(b)** Connectivity expanded along axis b

Figure A.7: Structure of the coordination polymer $C_{14}H_{18}Li_3N_2O_7Cl$

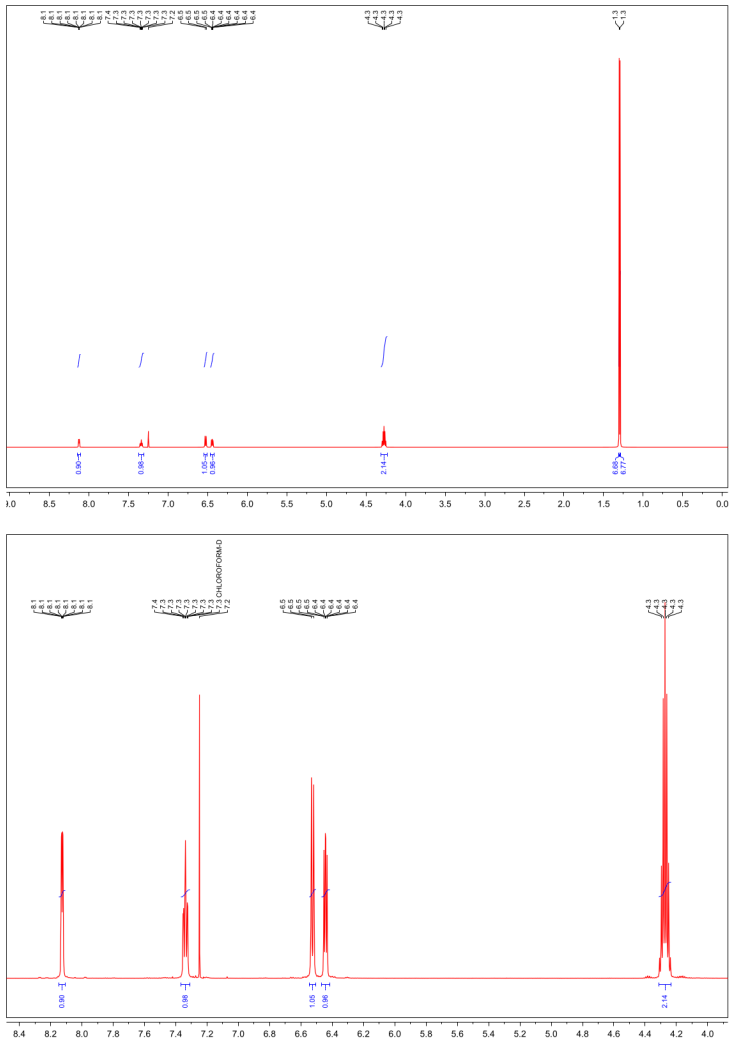

Figure A.8: ^{1}H-NMR ($CDCl_3$) spectra of 2-(diispropylamino)pyridine

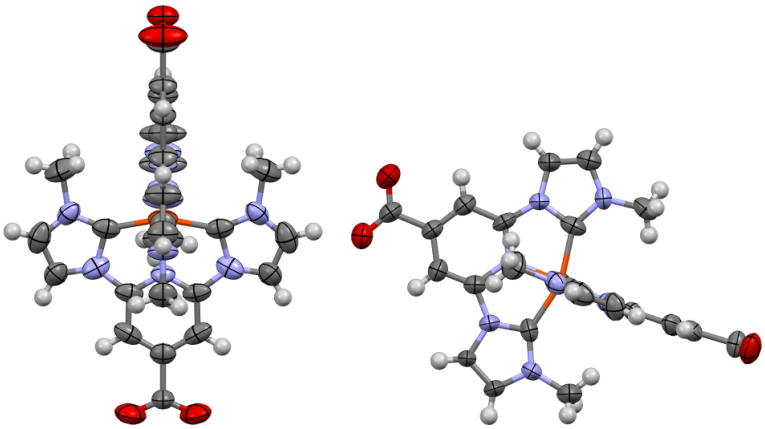

(a) View along a

(b) View along b

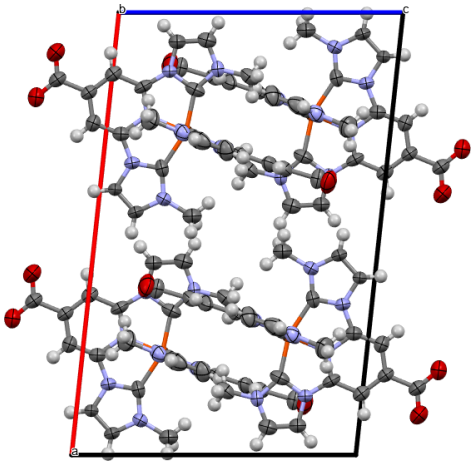

(c) Packing along b

Figure A.9: Crystallographic structure of complex **6**

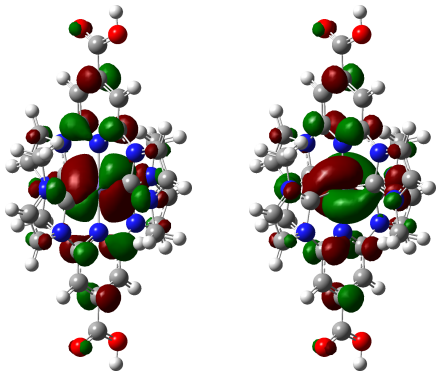

(a) HOMO −1 **(b)** HOMO

(c) LUMO **(d)** LUMO +1

Figure A.10: NTO for state 5 in complex **3**

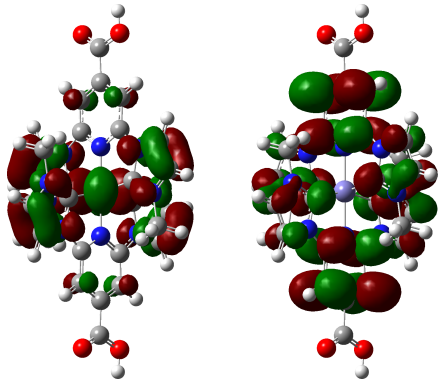

(a) HOMO **(b)** LUMO

Figure A.11: NTO for state 7 in complex **3**

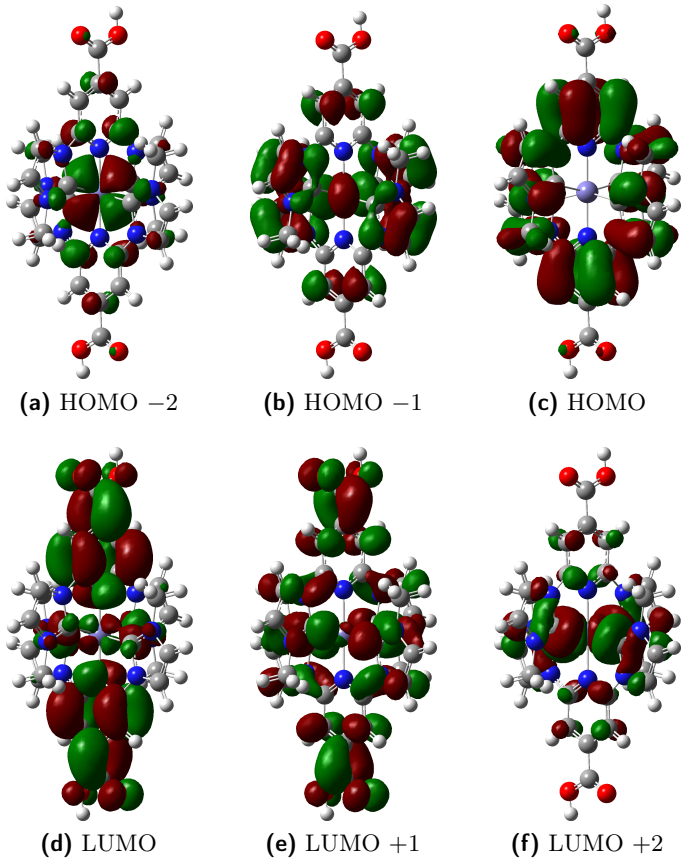

(a) HOMO −2 **(b)** HOMO −1 **(c)** HOMO

(d) LUMO **(e)** LUMO +1 **(f)** LUMO +2

Figure A.12: NTO for state 31 in complex **3**

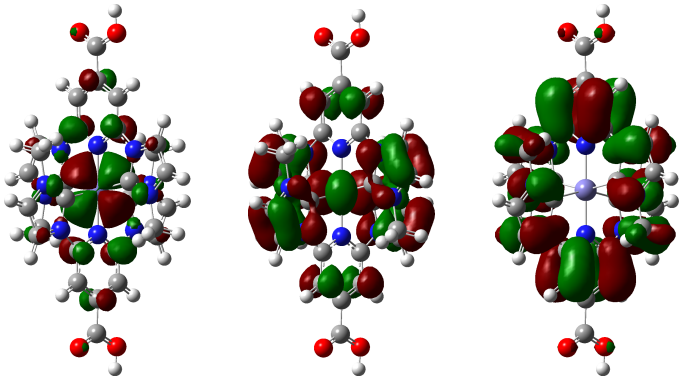

(a) HOMO −2 **(b)** HOMO −1 **(c)** HOMO

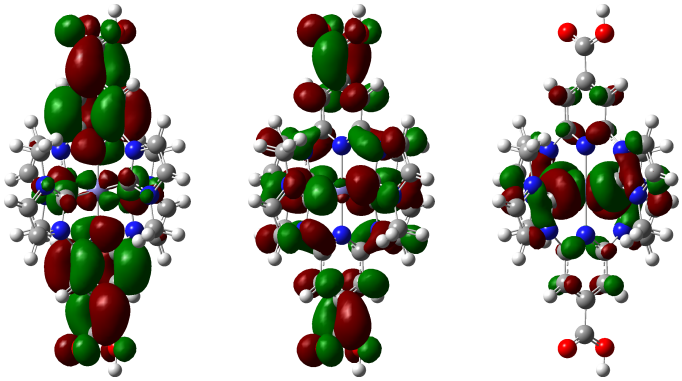

(d) LUMO **(e)** LUMO +1 **(f)** LUMO +2

Figure A.13: NTO for state 32 in complex **3**

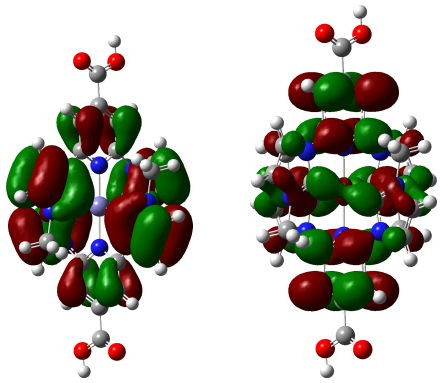

(a) HOMO **(b)** LUMO

Figure A.14: NTO for state 33 in complex **3**

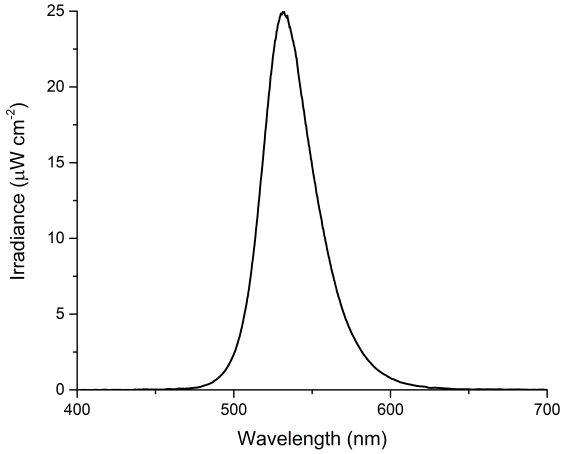

Figure A.15: Irradiance of the green LED used in the photocatalytic reactions

Appendix B

Crystallographic tables

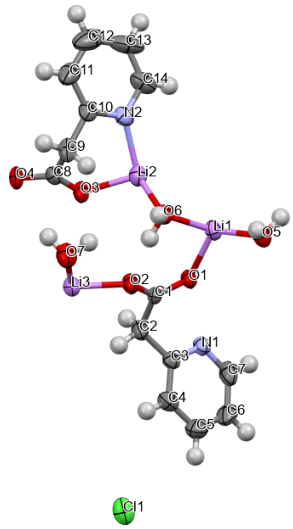

Figure B.1: Asymmetric unit of compound **1**

Table B.1: Crystal data and structure refinement for compound **1**

Identification code	$[Li(H_2O)]_3(2-pyridylacetate)_2Cl$
Empirical formula	$C_{14}H_{18}ClLi_3N_2O_7$
Formula weight	382.57
Temperature/K	298.00
Crystal system	monoclinic
Space group	Cc
a/Å	18.908(2)
b/Å	9.9803(13)
c/Å	9.7792(8)
$\alpha/^\circ$	90
$\beta/^\circ$	93.492(9)
$\gamma/^\circ$	90
Volume/Å^3	1842.0(3)
Z	4
ρ_{calc}g/cm^3	1.380
μ/mm^{-1}	0.244
F(000)	792.0
Crystal size/mm^3	$0.12 \times 0.1 \times 0.08$
Radiation MoK$_\alpha$	($\lambda = 0.71073$)
2θ range for data collection/$^\circ$	6.312 to 52.74
Index ranges	$-22 \leq h \leq 23$, $-12 \leq k \leq 8$, $-10 \leq l \leq 12$
Reflections collected	7086
Independent reflections	3312 [$R_{int} = 0.0427$, $R_{sigma} = 0.0652$]
Data/restraints/parameters	3312/2/254
Goodness-of-fit on F^2	1.014
Final R indexes [I>= 2σ (I)]	$R_1 = 0.0455$, $wR_2 = 0.0809$
Final R indexes [all data]	$R_1 = 0.0658$, $wR_2 = 0.0913$
Largest diff. peak/hole / e Å^{-3}	$0.20/-0.19$
Flack parameter	$-0.02(6)$

Table B.2: Bond lengths for compound **1** ([1]=+X,-1-Y,1/2+Z; [2]=+X,-1-Y,-1/2+Z)

Atom	Atom	Length/Å	Atom	Atom	Length/Å
O1	C1	1.257(4)	Li2	N2	2.067(8)
O1	Li3[1]	1.972(8)	Li2	C8	2.774(8)
O1	Li1	2.007(8)	Li2	O4[1]	1.902(9)
O2	C1	1.259(5)	Li2	Li1	3.049(10)
O2	Li3	1.966(7)	Li2	Li1[2]	3.451(10)
N1	C3	1.343(6)	O3	C8	1.258(5)
N1	C7	1.344(6)	O3	Li1[2]	1.956(8)
N1	Li3[1]	2.068(8)	C10	N2	1.336(5)
C1	C2	1.509(6)	C10	C9	1.511(7)
C3	C4	1.386(6)	C10	C11	1.372(7)
C3	C2	1.497(6)	N2	C14	1.342(6)
C4	C5	1.374(7)	C8	C9	1.522(6)
C7	C6	1.366(7)	C8	O4	1.249(5)
C6	C5	1.370(8)	C8	Li1[2]	2.772(8)
O6	Li2	1.963(9)	C14	C13	1.362(8)
O6	Li1	2.003(8)	C11	C12	1.379(10)
O7	Li3	1.927(9)	C12	C13	1.388(10)
Li3	Li1[2]	3.147(11)	Li1	O5	1.923(7)
Li2	O3	1.949(7)			

Table B.3: Bond angles for compound **1** ([1]=+X,-1-Y,1/2+Z; [2]=+X,-1-Y,-1/2+Z)

Atom	Atom	Atom	Angle/°	Atom	Atom	Atom	Angle/°
C1	O1	Li3[1]	125.6(3)	C8	O3	Li1[2]	117.6(3)
C1	O1	Li1	127.8(3)	N2	C10	C9	115.5(4)
Li3[1]	O1	Li1	104.6(3)	N2	C10	C11	122.5(5)
C1	O2	Li3	139.0(4)	C11	C10	C9	121.9(5)
C3	N1	C7	116.9(4)	C10	N2	Li2	114.8(4)
C3	N1	Li3[1]	119.5(4)	C10	N2	C14	117.7(4)
C7	N1	Li3[1]	118.3(3)	C14	N2	Li2	125.4(4)
O1	C1	O2	123.7(4)	O3	C8	Li2	38.3(2)
O1	C1	C2	119.8(4)	O3	C8	C9	117.9(4)
O2	C1	C2	116.4(4)	O3	C8	Li1[2]	38.7(2)
N1	C3	C4	121.1(4)	C9	C8	Li2	80.1(3)
N1	C3	C2	117.2(4)	C9	C8	Li1[2]	155.9(3)
C4	C3	C2	121.7(4)	O4	C8	Li2	159.9(4)
C5	C4	C3	120.8(5)	O4	C8	O3	124.1(4)
C3	C2	C1	117.1(4)	O4	C8	C9	118.0(4)
N1	C7	C6	124.7(5)	O4	C8	Li1[2]	85.8(3)
C7	C6	C5	118.4(5)	Li1[2]	C8	Li2	77.0(2)
C6	C5	C4	118.1(5)	C10	C9	C8	110.1(4)
Li2	O6	Li1	100.5(3)	C8	O4	Li2[2]	130.0(4)
O1[2]	Li3	N1[2]	92.3(3)	N2	C14	C13	123.3(6)
O1[2]	Li3	Li1[2]	38.1(2)	C10	C11	C12	119.4(6)
O2	Li3	O1[2]	110.0(4)	C11	C12	C13	118.2(6)
O2	Li3	N1[2]	111.9(4)	C14	C13	C12	118.8(6)
O2	Li3	Li1[2]	83.1(3)	O1	Li1	Li3[1]	37.3(2)
N1[2]	Li3	Li1[2]	128.3(4)	O1	Li1	Li2[1]	118.5(3)
O7	Li3	O1[2]	126.4(4)	O1	Li1	Li2	96.7(3)
O7	Li3	O2	104.4(4)	O1	Li1	C8[1]	97.5(3)
O7	Li3	N1[2]	111.6(4)	O6	Li1	O1	96.6(3)
O7	Li3	Li1[2]	111.6(3)	O6	Li1	Li3[1]	129.9(3)
O6	Li2	N2	122.5(5)	O6	Li1	Li2[1]	133.9(3)
O6	Li2	C8	109.0(4)	O6	Li1	Li2	39.3(2)
O6	Li2	Li1	40.3(2)	O6	Li1	C8[1]	97.9(3)
O6	Li2	Li1[2]	105.7(3)	Li3[1]	Li1	Li2[1]	81.4(2)
O3	Li2	O6	108.6(4)	Li2	Li1	Li3[1]	111.2(3)
O3	Li2	N2	95.3(3)	Li2	Li1	Li2[1]	103.5(3)
O3	Li2	C8	23.56(16)	O3[1]	Li1	O1	108.1(4)
O3	Li2	Li1[2]	28.0(2)	O3[1]	Li1	O6	116.5(4)
O3	Li2	Li1	128.0(4)	O3[1]	Li1	Li3[1]	77.1(3)
N2	Li2	C8	75.4(3)	O3[1]	Li1	Li2[1]	27.85(19)

Continued on the next page

Continued from previous page

Atom	Atom	Atom	Angle/°	Atom	Atom	Atom	Angle/°
N2	Li2	$Li1^2$	117.5(3)	$O3^1$	Li1	Li2	79.5(3)
N2	Li2	Li1	135.2(4)	$O3^1$	Li1	$C8^1$	23.72(15)
C8	Li2	$Li1^2$	51.50(19)	$C8^1$	Li1	$Li3^1$	77.1(2)
C8	Li2	Li1	142.1(3)	$C8^1$	Li1	$Li2^1$	51.54(19)
$O4^1$	Li2	O6	108.7(4)	$C8^1$	Li1	Li2	58.8(2)
$O4^1$	Li2	O3	108.7(4)	O5	Li1	O1	120.3(4)
$O4^1$	Li2	N2	111.6(4)	O5	Li1	O6	113.8(4)
$O4^1$	Li2	C8	127.6(4)	O5	Li1	$Li3^1$	108.9(3)
$O4^1$	Li2	Li1	68.9(3)	O5	Li1	Li2	139.2(4)
$O4^1$	Li2	$Li1^2$	84.1(3)	O5	Li1	$Li2^1$	75.0(3)
Li1	Li2	$Li1^2$	107.2(3)	O5	Li1	$O3^1$	102.3(3)
Li2	O3	$Li1^2$	124.2(3)	O5	Li1	$C8^1$	125.2(3)
C8	O3	Li2	118.2(4)				

Concluded from previous page

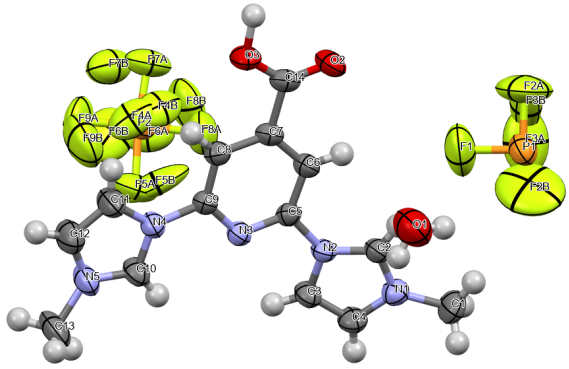

Figure B.2: Asymmetric unit compound **4**

Table B.4: Crystal data and structure refinement for compound **4**

Identification code	$[H_3L][H_2L][PF_6]_2$
Empirical formula	$C_{14}H_{16.5}F_9N_5O_3P_{1.5}$
Formula weight	520.28
Temperature/K	298.00
Crystal system	triclinic
Space group	P-1
a/Å	6.6868(7)
b/Å	12.3126(14)
c/Å	13.4479(15)
$\alpha/^\circ$	69.164(10)
$\beta/^\circ$	83.357(9)
$\gamma/^\circ$	89.867(9)
Volume/Å^3	1026.9(2)
Z	2
ρ_{calc}g/cm^3	1.683
μ/mm^{-1}	0.281
F(000)	526.0
Crystal size/mm^3	$0.12 \times 0.09 \times 0.05$
Radiation MoK$_\alpha$	($\lambda = 0.71073$)
2θ range for data collection/$^\circ$	6.59 to 52.734
Index ranges	$-8 \leq h \leq 8$, $-15 \leq k \leq 15$, $-16 \leq l \leq 16$
Reflections collected	18248
Independent reflections	4208 [$R_{int} = 0.0807$, $R_{sigma} = 0.0789$]
Data/restraints/parameters	4208/6/374
Goodness-of-fit on F^2	1.010
Final R indexes [I>= 2σ (I)]	$R_1 = 0.0602$, $wR_2 = 0.1181$
Final R indexes [all data]	$R_1 = 0.1361$, $wR_2 = 0.1490$
Largest diff. peak/hole / e Å^{-3}	$0.35/-0.21$

Table B.5: Bond lengths for compound **4** ([1]= -1-X,-1-Y,3-Z)

Atom	Atom	Length/Å	Atom	Atom	Length/Å
P1	F1	1.562(3)	N2	C2	1.332(4)
P1	F1[1]	1.562(3)	N2	C3	1.374(4)
P1	F2A	1.509(11)	N3	C9	1.324(4)
P1	F2A[1]	1.510(11)	N3	C5	1.323(4)
P1	F3A[1]	1.514(9)	O3	C14	1.278(4)
P1	F3A	1.514(9)	O2	C14	1.213(4)
P1	F2B	1.431(11)	C9	N4	1.421(4)
P1	F2B[1]	1.431(11)	C9	C8	1.366(4)
P1	F3B	1.554(12)	C5	C6	1.383(4)
P1	F3B[1]	1.554(12)	C7	C6	1.383(4)
P2	F5A	1.550(7)	C7	C8	1.380(4)
P2	F4A	1.561(8)	C7	C14	1.505(4)
P2	F9A	1.501(6)	N4	C10	1.321(4)
P2	F7A	1.574(5)	N4	C11	1.369(4)
P2	F6A	1.587(5)	C2	N1	1.312(4)
P2	F8A	1.616(5)	N1	C4	1.369(4)
P2	F9B	1.581(10)	N1	C1	1.460(4)
P2	F7B	1.632(9)	C3	C4	1.333(5)
P2	F4B	1.520(11)	N5	C10	1.310(4)
P2	F5B	1.508(12)	N5	C13	1.467(4)
P2	F8B	1.492(7)	N5	C12	1.360(5)
P2	F6B	1.571(9)	C11	C12	1.336(5)
N2	C5	1.429(4)			

Table B.6: Bond angles for compound **4** ([1]=-1-X,-1-Y,3-Z)

Atom	Atom	Atom	Angle/°	Atom	Atom	Atom	Angle/°
F1[1]	P1	F1	180.0	F4B	P2	F6B	169.2(10)
F2A	P1	F1	92.0(7)	F5B	P2	F9B	88.8(11)
F2A[1]	P1	F1	88.0(7)	F5B	P2	F7B	170.6(10)
F2A[1]	P1	F1[1]	92.0(7)	F5B	P2	F4B	94.3(13)
F2A	P1	F1[1]	88.0(7)	F5B	P2	F6B	94.6(11)
F2A	P1	F2A[1]	180.0	F8B	P2	F9B	172.6(8)
F2A[1]	P1	F3A	90.9(8)	F8B	P2	F7B	90.3(6)
F2A	P1	F3A	89.1(8)	F8B	P2	F4B	93.9(8)
F2A	P1	F3A[1]	90.9(8)	F8B	P2	F5B	98.4(10)
F2A[1]	P1	F3A[1]	89.1(8)	F8B	P2	F6B	90.8(7)

Continued on the next page

Continued from previous page

Atom	Atom	Atom	Angle/°	Atom	Atom	Atom	Angle/°
F2A[1]	P1	F3B[1]	49.3(7)	F6B	P2	F9B	86.7(8)
F2A	P1	F3B[1]	130.7(7)	F6B	P2	F7B	81.6(7)
F3A	P1	F1[1]	91.3(5)	C2	N2	C5	125.9(3)
F3A[1]	P1	F1[1]	88.7(5)	C2	N2	C3	108.1(3)
F3A	P1	F1	88.7(5)	C3	N2	C5	125.7(3)
F3A[1]	P1	F1	91.3(5)	C5	N3	C9	116.1(3)
F3A[1]	P1	F3A	179.999(14)	N3	C9	N4	114.6(3)
F3A[1]	P1	F3B1	39.8(8)	N3	C9	C8	124.7(3)
F3A	P1	F3B1	140.2(9)	C8	C9	N4	120.8(3)
F2B[1]	P1	F1	85.9(8)	N3	C5	N2	113.3(3)
F2B	P1	F1	94.1(8)	N3	C5	C6	125.1(3)
F2B	P1	F3B	91.3(8)	C6	C5	N2	121.6(3)
F2B[1]	P1	F3B[1]	91.3(8)	C6	C7	C14	121.1(3)
F2B[1]	P1	F3B	88.7(8)	C8	C7	C6	119.4(3)
F2B	P1	F3B[1]	88.7(8)	C10	N4	C9	125.5(3)
F3B[1]	P1	F1	89.7(5)	C10	N4	C11	108.1(3)
F3B[1]	P1	F3B	180.000(17)	C11	N4	C9	126.3(3)
F5A	P2	F4A	89.9(8)	C7	C6	C5	116.8(3)
F5A	P2	F7A	173.8(6)	N1	C2	N2	108.6(3)
F5A	P2	F6A	88.0(6)	C9	C8	C7	118.0(3)
F5A	P2	F8A	85.2(5)	C2	N1	C4	108.7(3)
F4A	P2	F7A	89.3(6)	C2	N1	C1	124.9(3)
F4A	P2	F6A	175.4(6)	C4	N1	C1	126.4(3)
F4A	P2	F8A	87.7(4)	O3	C14	C7	112.0(3)
F9A	P2	F5A	92.2(6)	O2	C14	O3	126.6(3)
F9A	P2	F4A	90.7(5)	O2	C14	C7	121.4(3)
F9A	P2	F7A	94.0(4)	C4	C3	N2	107.0(3)
F9A	P2	F6A	93.4(5)	C10	N5	C13	125.8(3)
F9A	P2	F8A	176.9(4)	C10	N5	C12	108.0(3)
F7A	P2	F6A	92.4(3)	C12	N5	C13	125.9(3)
F7A	P2	F8A	88.6(4)	N5	C10	N4	109.3(3)
F6A	P2	F8A	88.1(4)	C3	C4	N1	107.5(3)
F9B	P2	F7B	82.4(7)	C12	C11	N4	106.5(3)
F4B	P2	F9B	87.4(8)	C11	C12	N5	108.0(4)
F4B	P2	F7B	88.6(10)				

Concluded from previous page

Table B.7: Crystal data and structure refinement for compound **5**

Identification code	$[H_3L][NO_3][PF_6]$
Empirical formula	$C_{14}H_{15}F_6N_6O_5P$
Formula weight	492.29
Temperature/K	298.00
Crystal system	triclinic
Space group	P-1
a/Å	13.0056(17)
b/Å	13.754(2)
c/Å	13.8133(19)
$\alpha/^\circ$	60.214(15)
$\beta/^\circ$	77.997(11)
$\gamma/^\circ$	67.880(13)
Volume/Å^3	1986.0(6)
Z	4
ρ_{calc}g/cm^3	1.646
μ/mm^{-1}	0.236
F(000)	1000.0
Crystal size/mm^3	$0.13 \times 0.11 \times 0.1$
Radiation MoK$_\alpha$	($\lambda = 0.71073$)
2θ range for data collection/$^\circ$	6.33 to 52.744
Index ranges	$-16 \leq h \leq 14$, $-15 \leq k \leq 17$, $-17 \leq l \leq 17$
Reflections collected	17146
Independent reflections	8100 [$R_{int} = 0.1386$, $R_{sigma} = 0.3058$]
Data/restraints/parameters	8100/117/693
Goodness-of-fit on F^2	0.946
Final R indexes [I>= 2σ (I)]	$R_1 = 0.0926$, $wR_2 = 0.0905$
Final R indexes [all data]	$R_1 = 0.3351$, $wR_2 = 0.1459$
Largest diff. peak/hole / e Å^{-3}	$0.26/-0.23$

Table B.8: Bond lengths for compound **5**

Atom	Atom	Length/Å	Atom	Atom	Length/Å
P1	F3A	1.544(7)	C5	C6	1.383(8)
P1	F3AA	1.562(5)	C8	C9	1.365(8)
P1	F5A	1.546(5)	O2	C14	1.320(7)
P1	F6A	1.586(6)	C3	C2	1.325(8)
P1	F2AA	1.573(7)	N3	C12	1.308(8)
P1	F4A	1.540(6)	N3	C11	1.366(8)
P1	F2B	1.55(2)	N3	C13	1.472(8)
P1	F4B	1.565(18)	C10	C11	1.340(9)
P1	F3B	1.566(19)	N10	C19	1.323(7)
P1	F1B	1.59(2)	N10	C23	1.322(7)
P1	F6B	1.535(19)	N9	C23	1.426(7)
P1	F5B	1.548(18)	N9	C8CA	1.340(7)
P2	F8A	1.587(10)	N9	C24	1.368(7)
P2	F11A	1.545(14)	O4	C27	1.318(7)
P2	F7A	1.552(13)	C19	N11	1.430(7)
P2	F9A	1.631(10)	C19	C20	1.378(8)
P2	F12A	1.580(11)	N12	C16	1.315(7)
P2	F10A	1.572(12)	N12	C15	1.468(7)
P2	F9B	1.633(12)	N12	C17	1.366(8)
P2	F10B	1.583(14)	N11	C16	1.335(7)
P2	F8B	1.560(12)	N11	C18	1.372(7)
P2	F11B	1.564(10)	C23	C22	1.372(8)
P2	F7B	1.582(15)	N8	C8CA	1.317(7)
P2	F12B	1.571(15)	N8	C25	1.374(7)
N6	C5	1.425(7)	N8	C26	1.459(7)
N6	C3	1.367(7)	O3	C27	1.202(7)
N6	C4	1.350(7)	C21	C20	1.405(7)
N5	C5	1.305(7)	C21	C22	1.357(8)
N5	C9	1.321(7)	C21	C27	1.513(9)
C7	C8	1.377(8)	C25	C24	1.334(8)
C7	C6	1.381(8)	C17	C18	1.352(8)
C7	C14	1.496(9)	O5	N1	1.241(6)
N4	C12	1.327(8)	O6	N1	1.228(7)
N4	C9	1.433(8)	N1	O7	1.206(7)
N4	C10	1.384(7)	O9	N2	1.277(7)
O1	C14	1.198(8)	O8	N2	1.215(7)
N7	C4	1.311(7)	N2	O10	1.212(7)
N7	C2	1.376(8)	F2B	F1B	1.51(11)
N7	C1	1.470(7)	F1B	F5B	1.67(9)

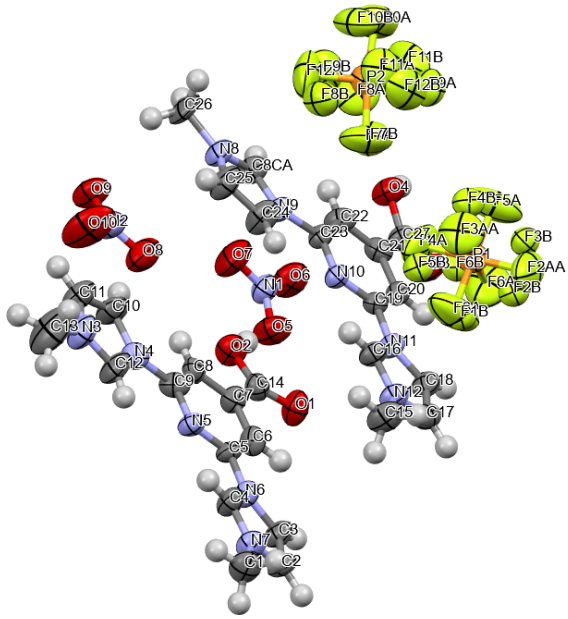

Figure B.3: Asymmetric unit of compound **5**

Table B.9: Bond angles for compound **5**

Atom	Atom	Atom	Angle/°	Atom	Atom	Atom	Angle/°
F3A	P1	F3AA	92.5(7)	C10	N4	C9	126.7(6)
F3A	P1	F5A	178.2(7)	C4	N7	C2	108.7(5)
F3A	P1	F6A	85.3(7)	C4	N7	C1	126.5(6)
F3A	P1	F2AA	89.2(8)	C2	N7	C1	124.7(6)
F3AA	P1	F6A	175.5(4)	N5	C5	N6	114.7(6)
F3AA	P1	F2AA	84.9(5)	N5	C5	C6	124.5(6)
F5A	P1	F3AA	89.2(3)	C6	C5	N6	120.8(6)
F5A	P1	F6A	93.0(4)	C9	C8	C7	117.4(6)
F5A	P1	F2AA	90.3(4)	C2	C3	N6	108.3(6)
F2AA	P1	F6A	91.1(5)	C7	C6	C5	117.0(6)
F4A	P1	F3A	91.7(8)	C12	N3	C11	109.3(6)
F4A	P1	F3AA	95.1(4)	C12	N3	C13	126.1(7)
F4A	P1	F5A	88.8(4)	C11	N3	C13	124.6(7)
F4A	P1	F6A	89.0(4)	N3	C12	N4	108.5(6)

Continued on the next page

Continued from previous page

Atom	Atom	Atom	Angle/°	Atom	Atom	Atom	Angle/°
F4A	P1	F2AA	179.1(5)	N5	C9	N4	113.1(6)
F2B	P1	F4B	113(2)	N5	C9	C8	124.7(7)
F2B	P1	F3B	76(2)	C8	C9	N4	122.2(6)
F2B	P1	F1B	57(5)	N7	C4	N6	108.6(6)
F4B	P1	F3B	88.5(19)	O1	C14	C7	123.1(7)
F4B	P1	F1B	136(3)	O1	C14	O2	125.5(7)
F3B	P1	F1B	123(4)	O2	C14	C7	111.4(7)
F6B	P1	F2B	123(3)	C3	C2	N7	107.2(6)
F6B	P1	F4B	119(2)	C11	C10	N4	106.5(6)
F6B	P1	F3B	82(2)	C10	C11	N3	107.3(6)
F6B	P1	F1B	96(4)	C23	N10	C19	115.7(5)
F6B	P1	F5B	97(2)	C8CA	N9	C23	126.2(5)
F5B	P1	F2B	110(2)	C8CA	N9	C24	107.3(6)
F5B	P1	F4B	85(2)	C24	N9	C23	126.4(5)
F5B	P1	F3B	173(2)	N10	C19	N11	113.1(5)
F5B	P1	F1B	64(4)	N10	C19	C20	125.1(6)
F8A	P2	F9A	89.6(8)	C20	C19	N11	121.8(6)
F11A	P2	F8A	176.0(9)	C16	N12	C15	125.1(6)
F11A	P2	F7A	90.3(10)	C16	N12	C17	108.9(6)
F11A	P2	F9A	86.5(7)	C17	N12	C15	125.9(6)
F11A	P2	F12A	91.6(9)	C16	N11	C19	123.0(5)
F11A	P2	F10A	88.2(10)	C16	N11	C18	108.3(5)
F7A	P2	F8A	88.3(8)	C18	N11	C19	128.7(6)
F7A	P2	F9A	86.5(11)	N10	C23	N9	111.9(5)
F7A	P2	F12A	92.5(12)	N10	C23	C22	125.9(6)
F7A	P2	F10A	173.4(12)	C22	C23	N9	122.1(6)
F12A	P2	F8A	92.2(8)	C8CA	N8	C25	108.2(6)
F12A	P2	F9A	177.9(8)	C8CA	N8	C26	126.8(6)
F10A	P2	F8A	92.7(9)	C25	N8	C26	125.0(6)
F10A	P2	F9A	87.0(7)	C20	C21	C27	117.2(6)
F10A	P2	F12A	94.0(9)	C22	C21	C20	120.8(6)
F10B	P2	F9B	86.0(12)	C22	C21	C27	122.0(6)
F8B	P2	F9B	87.2(8)	C19	C20	C21	115.9(6)
F8B	P2	F10B	90.8(9)	C21	C22	C23	116.5(6)
F8B	P2	F11B	174.7(11)	N12	C16	N11	108.7(6)
F8B	P2	F7B	87.3(11)	O4	C27	C21	110.7(6)
F8B	P2	F12B	89.4(11)	O3	C27	O4	125.8(6)
F11B	P2	F9B	87.5(10)	O3	C27	C21	123.4(6)
F11B	P2	F10B	88.2(7)	N8	C8CA	N9	109.2(6)
F11B	P2	F7B	93.2(11)	C24	C25	N8	107.3(6)
F11B	P2	F12B	95.9(11)	C25	C24	N9	108.0(6)

Continued on the next page

Continued from previous page

Atom	Atom	Atom	Angle/°	Atom	Atom	Atom	Angle/°
F7B	P2	F9B	88.2(11)	C18	C17	N12	107.3(6)
F7B	P2	F10B	173.9(14)	C17	C18	N11	106.7(6)
F12B	P2	F9B	176.0(12)	O6	N1	O5	117.5(6)
F12B	P2	F10B	91.9(12)	O7	N1	O5	121.3(7)
F12B	P2	F7B	93.8(12)	O7	N1	O6	121.2(6)
C3	N6	C5	129.6(6)	O8	N2	O9	120.0(7)
C4	N6	C5	123.2(6)	O10	N2	O9	118.4(7)
C4	N6	C3	107.2(5)	O10	N2	O8	121.5(7)
C5	N5	C9	116.9(6)	F1B	F2B	P1	63(3)
C8	C7	C6	119.6(6)	P1	F1B	F5B	56.6(19)
C8	C7	C14	121.6(6)	F2B	F1B	P1	60(3)
C6	C7	C14	118.8(7)	F2B	F1B	F5B	106(3)
C12	N4	C9	124.9(6)	P1	F5B	F1B	59(2)
C12	N4	C10	108.3(6)				

Concluded from previous page

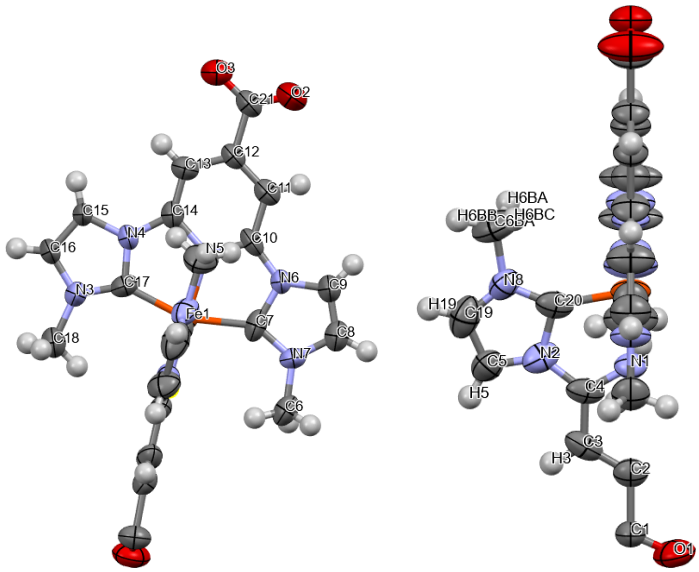

Figure B.4: Asymmetric unit of compound **6**

Table B.10: Crystal data and structure refinement for compound **6**

Identification code	FeL_2
Empirical formula	$C_{28}H_{24}FeN_{10}O_4$
Formula weight	620.42
Temperature/K	298.00
Crystal system	monoclinic
Space group	C2/m
a/Å	19.813(5)
b/Å	14.342(2)
c/Å	12.655(2)
$\alpha/^\circ$	90
$\beta/^\circ$	96.10
$\gamma/^\circ$	90
Volume/$Å^3$	3575.6(13)
Z	4
ρ_{calc}g/cm^3	1.153
μ/mm^{-1}	0.465
F(000)	1280.0
Crystal size/mm^3	$0.13 \times 0.11 \times 0.06$
Radiation MoK_α	($\lambda = 0.71073$)
2θ range for data collection/$^\circ$	6.54 to 52.742
Index ranges	$-24 \leq h \leq 24$, $-17 \leq k \leq 17$, $-15 \leq l \leq 15$
Reflections collected	28680
Independent reflections	3801 [$R_{int} = 0.1109$, $R_{sigma} = 0.2783$]
Data/restraints/parameters	3801/0/235
Goodness-of-fit on F^2	0.912
Final R indexes [I>= 2σ (I)]	$R_1 = 0.0519$, $wR_2 = 0.1235$
Final R indexes [all data]	$R_1 = 0.2519$, $wR_2 = 0.1826$
Largest diff. peak/hole / e $Å^{-3}$	$0.72/-0.45$

Table B.11: Bond lengths for compound **6** ([1]=+X,1-Y,+Z)

Atom	Atom	Length/Å	Atom	Atom	Length/Å
Fe1	N1	1.936(9)	C14	C13	1.330(15)
Fe1	N5	1.888(8)	C10	C11	1.448(15)
Fe1	C17	1.933(12)	C10	N6	1.353(14)
Fe1	C20	1.940(9)	C17	N4	1.346(13)
Fe1	C20[1]	1.940(9)	N4	C15	1.407(14)
Fe1	C7	1.937(11)	C13	C12	1.378(15)
N1	C4	1.311(9)	C11	C12	1.367(15)
N1	C41	1.311(9)	C16	C15	1.366(16)
N3	C17	1.370(14)	C21	C12	1.521(16)
N3	C16	1.383(15)	C21	O3	1.240(15)
N3	C18	1.478(14)	C21	O2	1.202(15)
N7	C6	1.456(13)	N6	C7	1.395(14)
N7	C8	1.370(14)	N6	C9	1.358(14)
N7	C7	1.367(13)	N8	C20	1.353(10)
N5	C14	1.417(14)	N8	C6BA	1.546(10)
N5	C10	1.294(13)	N8	C19	1.307(12)
C2	C1	1.559(16)	C5	N2	1.358(10)
C2	C31	1.358(10)	C5	C19[1]	1.380(12)
C2	C3	1.358(10)	N2	C20[1]	1.412(10)
C1	O1	1.200(7)	N2	C4	1.409(11)
C1	O11	1.200(7)	C4	C3	1.406(11)
C14	N4	1.383(14)	C8	C9	1.325(17)

Table B.12: Bond angles for compound **6** (^{1}=+X,1-Y,+Z)

Atom	Atom	Atom	Angle/°	Atom	Atom	Atom	Angle/°
N1	Fe1	C20	79.5(3)	N3	C17	Fe1	142.9(9)
N1	Fe1	C20^1	79.5(3)	N4	C17	Fe1	113.4(8)
N1	Fe1	C7	100.4(5)	N4	C17	N3	103.7(9)
N5	Fe1	N1	179.2(4)	C14	N4	C15	126.3(10)
N5	Fe1	C17	79.6(4)	C17	N4	C14	121.1(10)
N5	Fe1	C20	100.5(3)	C17	N4	C15	112.6(9)
N5	Fe1	C20^1	100.5(3)	C14	C13	C12	119.0(11)
N5	Fe1	C7	78.8(5)	C12	C11	C10	119.6(11)
C17	Fe1	N1	101.2(4)	C15	C16	N3	107.1(12)
C17	Fe1	C20	91.4(2)	O3	C21	C12	117.6(11)
C17	Fe1	C20^1	91.4(2)	O2	C21	C12	116.1(13)
C17	Fe1	C7	158.5(5)	O2	C21	O3	126.4(13)
C20^1	Fe1	C20	159.0(5)	C13	C12	C21	120.4(11)
C7	Fe1	C20	92.5(2)	C11	C12	C13	119.5(11)
C7	Fe1	C20^1	92.5(2)	C11	C12	C21	120.1(11)
C4^1	N1	Fe1	119.8(5)	C16	C15	N4	104.9(10)
C4	N1	Fe1	119.8(5)	C10	N6	C7	114.0(10)
C4	N1	C4^1	120.4(10)	C10	N6	C9	134.6(10)
C17	N3	C16	111.7(10)	C9	N6	C7	111.4(9)
C17	N3	C18	124.6(10)	C20	N8	C6BA	121.0(8)
C16	N3	C18	123.7(11)	C19	N8	C20	116.9(8)
C8	N7	C6	124.4(10)	C19	N8	C6BA	122.1(8)
C7	N7	C6	124.1(10)	N2	C5	C19^1	104.2(9)
C7	N7	C8	111.5(10)	C5	N2	C20^1	113.8(7)
C14	N5	Fe1	121.2(8)	C5	N2	C4	132.3(8)
C10	N5	Fe1	120.3(8)	C4	N2	C20^1	113.9(8)
C10	N5	C14	118.4(10)	N8	C20	Fe1	147.2(7)
C3^1	C2	C1	120.4(6)	N8	C20	N2^1	98.3(7)
C3	C2	C1	120.4(6)	N21	C20	Fe1	114.5(7)
C3	C2	C3^1	119.1(11)	N1	C4	N2	112.3(7)
O1^1	C1	C2	114.3(6)	N1	C4	C3	121.1(9)
O1	C1	C2	114.3(6)	C3	C4	N2	126.6(8)
O1	C1	O1^1	131.4(13)	C2	C3	C4	119.1(9)
N4	C14	N5	104.6(10)	N8	C19	C5^1	106.8(9)
C13	C14	N5	123.2(11)	C9	C8	N7	107.7(11)
C13	C14	N4	132.1(11)	N7	C7	Fe1	144.3(10)
N5	C10	C1^1	120.2(11)	N7	C7	N6	102.0(10)
N5	C10	N6	113.1(10)	N6	C7	Fe1	113.7(8)
N6	C10	C11	126.7(11)	C8	C9	N6	107.4(11)

Bibliography

[1] G. Ciamician, "The Photochemistry of the Future", *Science* **1912**, *36*, 385–394, DOI 10.1126/science.36.926.385.

[2] V. Balzani, P. Ceroni, A. Juris, *Photochemistry and photophysics: concepts, research, applications*, John Wiley & Sons, **2014**, ISBN: 3-527-33479-3.

[3] W. E. J. Jones, M. A. Fox, "Determination of Excited-State Redox Potentials by Phase-Modulated Voltammetry", *The Journal of Physical Chemistry* **1994**, *98*, 5095–5099, DOI 10.1021/j100070a025.

[4] S. Campagna, F. Puntoriero, F. Nastasi, G. Bergamini, V. Balzani in *Photochemistry and Photophysics of Coordination Compounds I*, (Eds.: V. Balzani, S. Campagna), Topics in Current Chemistry, Springer, Berlin, Heidelberg, **2007**, pp. 117–214, ISBN: 978-3-540-73347-8, DOI 10.1007/128_2007_133.

[5] O. S. Wenger, "Photoactive Complexes with Earth-Abundant Metals", *Journal of the American Chemical Society* **2018**, *140*, 13522–13533, DOI 10.1021/jacs.8b08822.

[6] N. A. P. Kane-Maguire in *Photochemistry and Photophysics of Coordination Compounds I*, (Eds.: V. Balzani, S. Campagna), Topics in Current Chemistry, Springer, Berlin, Heidelberg, **2007**, pp. 37–67, ISBN: 978-3-540-73347-8, DOI 10.1007/128_2007_141.

[7] C. Conti, F. Castelli, L. S. Forster, "Photophysics of $Cr(CN_6)^{3-}$ and $Co(CN_6)^{3-}$ in polyalcohol-water solutions at room temperature", *The Journal of Physical Chemistry* **1979**, *83*, 2371–2376, DOI 10.1021/j100481a013.

[8] P. Riccieri, E. Zinato, A. Damiani, "Ligand field photochemistry of trans-tetraamminechromium(III) complexes with one strong-field and one weak-field axial ligand", *Inorganic Chemistry* **1987**, *26*, 2667–2674, DOI 10.1021/ic00263a023.

[9] P. Riccieri, E. Zinato, "Pentacyanoamminechromate(III). Synthesis, characterization, and photochemistry", *Inorganic Chemistry* **1990**, *29*, 5035–5041, DOI 10.1021/ic00350a007.

[10] E. Zinato, P. Riccieri, "Pentacyanochromate(III) complexes: ground- and excited-state chemistry", *Coordination Chemistry Reviews* **2001**, *211*, 5–24, DOI 10.1016/S0010-8545(00)00290-3.

[11] L. A. Büldt, O. S. Wenger, "Chromium complexes for luminescence, solar cells, photoredox catalysis, upconversion, and phototriggered NO release", *Chemical Science* **2017**, *8*, 7359–7367, DOI 10.1039/C7SC03372A.

[12] S. M. Stevenson, M. P. Shores, E. M. Ferreira, "Photooxidizing Chromium Catalysts for Promoting Radical Cation Cycloadditions", *Angewandte Chemie International Edition* **2015**, *54*, 6506–6510, DOI 10.1002/anie.201501220.

[13] R. F. Higgins, S. M. Fatur, S. G. Shepard, S. M. Stevenson, D. J. Boston, E. M. Ferreira, N. H. Damrauer, A. K. Rappé, M. P. Shores, "Uncovering the Roles of Oxygen in Cr(III) Photoredox Catalysis", *Journal of the American Chemical Society* **2016**, *138*, 5451–5464, DOI 10.1021/jacs.6b02723.

[14] S. Otto, M. Grabolle, C. Förster, C. Kreitner, U. Resch-Genger, K. Heinze, "$[Cr(ddpd)_2]^{3+}$: A Molecular, Water-Soluble, Highly NIR-Emissive Ruby Analogue", *Angewandte Chemie International Edition* **2015**, *54*, 11572–11576, DOI 10.1002/anie.201504894.

[15] N. Armaroli, G. Accorsi, F. Cardinali, A. Listorti in *Photochemistry and Photophysics of Coordination Compounds I*, (Eds.: V. Balzani, S. Campagna), Topics in Current Chemistry, Springer, Berlin, Heidelberg, **2007**, pp. 69–115, ISBN: 978-3-540-73347-8, DOI 10.1007/128_2007_128.

[16] C. Femoni, S. Muzzioli, A. Palazzi, S. Stagni, S. Zacchini, F. Monti, G. Accorsi, M. Bolognesi, N. Armaroli, M. Massi, G. Valenti, M. Marcaccio, "New tetrazole-based Cu(I) homo- and heteroleptic complexes with various P^P ligands: synthesis, characterization, redox and photophysical properties", *Dalton Transactions* **2012**, *42*, 997–1010, DOI 10.1039/C2DT32056H.

[17] O. Reiser, "Shining Light on Copper: Unique Opportunities for Visible-Light-Catalyzed Atom Transfer Radical Addition Reactions and Related Processes", *Accounts of Chemical Research* **2016**, *49*, 1990–1996, DOI 10.1021/acs.accounts.6b00296.

[18] C. Minozzi, A. Caron, J.-C. Grenier-Petel, J. Santandrea, S. K. Collins, "Heteroleptic Copper(I)-Based Complexes for Photocatalysis: Combinatorial Assembly, Discovery, and Optimization", *Angewandte Chemie International Edition* **2018**, *57*, 5477–5481, DOI 10.1002/anie.201800144.

[19] S. E. Creutz, K. J. Lotito, G. C. Fu, J. C. Peters, "Photoinduced Ullmann C−N Coupling: Demonstrating the Viability of a Radical Pathway", *Science* **2012**, *338*, 647–651, DOI 10.1126/science.1226458.

[20] S. Shanmugam, J. Xu, C. Boyer, "Exploiting Metalloporphyrins for Selective Living Radical Polymerization Tunable over Visible Wavelengths", *Journal of the American Chemical Society* **2015**, *137*, 9174–9185, DOI 10.1021/jacs.5b05274.

[21] K. Rybicka-Jasińska, W. Shan, K. Zawada, K. M. Kadish, D. Gryko, "Porphyrins as Photoredox Catalysts: Experimental and Theoretical Studies", *Journal of the American Chemical Society* **2016**, *138*, 15451–15458, DOI 10.1021/jacs.6b09036.

[22] Y. Sakai, Y. Sagara, H. Nomura, N. Nakamura, Y. Suzuki, H. Miyazaki, C. Adachi, "Zinc complexes exhibiting highly efficient thermally activated delayed fluorescence and their application to organic light-emitting diodes", *Chemical Communications* **2015**, *51*, 3181–3184, DOI 10.1039/C4CC09403D.

[23] B. J. Shields, B. Kudisch, G. D. Scholes, A. G. Doyle, "Long-Lived Charge-Transfer States of Nickel(II) Aryl Halide Complexes Facilitate Bimolecular Photoinduced Electron Transfer", *Journal of the American Chemical Society* **2018**, *140*, 3035–3039, DOI 10.1021/jacs.7b13281.

[24] L. A. Büldt, C. B. Larsen, O. S. Wenger, "Luminescent Ni^0 Diisocyanide Chelates as Analogues of CuI Diimine Complexes", *Chemistry – A European Journal* **2017**, *23*, 8577–8580, DOI 10.1002/chem.201700103.

[25] C. Creutz, M. Chou, T. L. Netzel, M. Okumura, N. Sutin, "Lifetimes, spectra, and quenching of the excited states of polypyridine complexes of iron(II), ruthenium(II), and osmium(II)", *Journal of the American Chemical Society* **1980**, *102*, 1309–1319, DOI 10.1021/ja00524a014.

[26] A. Cannizzo, C. J. Milne, C. Consani, W. Gawelda, C. Bressler, F. van Mourik, M. Chergui, "Light-induced spin crossover in Fe(II)-based complexes: The full photocycle unraveled by ultrafast optical and X-ray spectroscopies", *Coordination Chemistry Reviews* **2010**, *254*, 2677–2686, DOI 10.1016/j.ccr.2009.12.007.

[27] A. Gualandi, M. Marchini, L. Mengozzi, M. Natali, M. Lucarini, P. Ceroni, P. G. Cozzi, "Organocatalytic Enantioselective Alkylation of Aldehydes with $[Fe(bpy)_3]Br_2$ Catalyst and Visible Light", *ACS Catalysis* **2015**, *5*, 5927–5931, DOI 10.1021/acscatal.5b01573.

[28] O. S. Wenger, "Is Iron the New Ruthenium?", *Chemistry – A European Journal* **2019**, *25*, 6043–6052, DOI 10.1002/chem.201806148.

[29] M. Cammarata, R. Bertoni, M. Lorenc, H. Cailleau, S. Di Matteo, C. Mauriac, S. F. Matar, H. Lemke, M. Chollet, S. Ravy, C. Laulhé, J.-F. Létard, E. Collet, "Sequential Activation of Molecular Breathing and Bending during Spin-Crossover Photoswitching Revealed by Femtosecond Optical and X-Ray Absorption Spectroscopy", *Physical Review Letters* **2014**, *113*, 227402, DOI 10.1103/PhysRevLett.113.227402.

[30] L. L. Jamula, A. M. Brown, D. Guo, J. K. McCusker, "Synthesis and Characterization of a High-Symmetry Ferrous Polypyridyl Complex: Approaching the $^5T_2/^3T_1$ Crossing Point for Fe(II)", *Inorganic Chemistry* **2014**, *53*, 15–17, DOI 10.1021/ic402407k.

[31] A. K. C. Mengel, C. Förster, A. Breivogel, K. Mack, J. R. Ochsmann, F. Laquai, V. Ksenofontov, K. Heinze, "A Heteroleptic Push-Pull Substituted Iron(II) Bis(tridentate) Complex with Low-Energy Charge-Transfer States", *Chemistry – A European Journal* **2015**, *21*, 704–714, DOI 10.1002/chem.201404955.

[32] P. J. Vallett, N. H. Damrauer, "Experimental and Computational Exploration of Ground and Excited State Properties of Highly Strained Ruthenium Terpyridine Complexes", *The Journal of Physical Chemistry A* **2013**, *117*, 6489–6507, DOI 10.1021/jp404248z.

[33] S. G. Shepard, S. M. Fatur, A. K. Rappé, N. H. Damrauer, "Highly Strained Iron(II) Polypyridines: Exploiting the Quintet Manifold To Extend the Lifetime of MLCT Excited States", *Journal of the American Chemical Society* **2016**, *138*, 2949–2952, DOI 10.1021/jacs.5b13524.

[34] Y. Liu, T. Harlang, S. E. Canton, P. Chábera, K. Suárez-Alcántara, A. Fleckhaus, D. A. Vithanage, E. Göransson, A. Corani, R. Lomoth, V. Sundström, K. Wärnmark, "Towards longer-lived metal-to-ligand charge transfer states of iron(II) complexes: an N-heterocyclic carbene approach", *Chem. Commun.* **2013**, *49*, 6412–6414, DOI 10.1039/C3CC43833C.

[35] L. A. Fredin, M. Pápai, E. Rozsályi, G. Vankó, K. Wärnmark, V. Sundström, P. Persson, "Exceptional Excited-State Lifetime of an Iron(II)-N-Heterocyclic Carbene Complex Explained", *The Journal of Physical Chemistry Letters* **2014**, *5*, 2066–2071, DOI 10.1021/jz500829w.

[36] T. Duchanois, T. Etienne, C. Cebrián, L. Liu, A. Monari, M. Beley, X. Assfeld, S. Haacke, P. C. Gros, "An Iron-Based Photosensitizer with Extended Excited-State Lifetime: Photophysical and Photovoltaic Properties", *European Journal of Inorganic Chemistry* **2015**, *2015*, 2469–2477, DOI https://doi.org/10.1002/ejic.201500142.

[37] T. C. B. Harlang, Y. Liu, O. Gordivska, L. A. Fredin, C. S. Ponseca, P. Huang, P. Chábera, K. S. Kjaer, H. Mateos, J. Uhlig, R. Lomoth, R. Wallenberg, S. Styring, P. Persson, V. Sundström, K. Wärnmark, "Iron sensitizer converts light to electrons with 92% yield", *Nature Chemistry* **2015**, *7*, 883–889, DOI 10.1038/nchem.2365.

[38] L. Liu, T. Duchanois, T. Etienne, A. Monari, M. Beley, X. Assfeld, S. Haacke, P. C. Gros, "A new record excited state ^{3}MLCT lifetime for metalorganic iron(II) complexes", *Physical Chemistry Chemical Physics* **2016**, *18*, 12550–12556, DOI 10.1039/C6CP01418F.

[39] P. Zimmer, L. Burkhardt, A. Friedrich, J. Steube, A. Neuba, R. Schepper, P. Müller, U. Flörke, M. Huber, S. Lochbrunner, M. Bauer, "The Connection between NHC Ligand Count and Photophysical Properties in Fe(II) Photosensitizers: An Experimental Study", *Inorganic Chemistry* **2018**, *57*, 360–373, DOI 10.1021/acs.inorgchem.7b02624.

[40] Y. Liu, P. Persson, V. Sundström, K. Wärnmark, "Fe N-Heterocyclic Carbene Complexes as Promising Photosensitizers", *Accounts of Chemical Research* **2016**, *49*, 1477–1485, DOI 10.1021/acs.accounts.6b00186.

[41] T. Duchanois, L. Liu, M. Pastore, A. Monari, C. Cebrián, Y. Trolez, M. Darari, K. Magra, A. Francés-Monerris, E. Domenichini, M. Beley, X. Assfeld, S. Haacke, P. C. Gros, "NHC-Based Iron Sensitizers for DSSCs", *Inorganics* **2018**, *6*, 63, DOI 10.3390/inorganics6020063.

[42] I. M. Dixon, F. Alary, M. Boggio-Pasqua, J.-L. Heully, "The $(N_4C_2)^-$ Donor Set as Promising Motif for Bis(tridentate) Iron(II) Photoactive Compounds", *Inorganic Chemistry* **2013**, *52*, 13369–13374, DOI 10.1021/ic402453p.

[43] I. M. Dixon, F. Alary, M. Boggio-Pasqua, J.-L. Heully, "Reversing the relative ^{3}MLCT-^{3}MC order in Fe(II) complexes using cyclometallating ligands: a computational study aiming at luminescent Fe(II) complexes", *Dalton Transactions* **2015**, *44*, 13498–13503, DOI 10.1039/C5DT01214G.

[44] C. Kreitner, E. Erdmann, W. W. Seidel, K. Heinze, "Understanding the Excited State Behavior of Cyclometalated Bis(tridentate)ruthenium(II) Complexes: A Combined Experimental and Theoretical Study", *Inorganic Chemistry* **2015**, *54*, 11088–11104, DOI 10.1021/acs.inorgchem.5b01151.

[45] C. Kreitner, K. Heinze, "Excited state decay of cyclometalated polypyridine ruthenium complexes: insight from theory and experiment", *Dalton Transactions* **2016**, *45*, 13631–13647, DOI 10.1039/C6DT01989G.

[46] Y. Liu, K. S. Kjær, L. A. Fredin, P. Chábera, T. Harlang, S. E. Canton, S. Lidin, J. Zhang, R. Lomoth, K.-E. Bergquist, P. Persson, K. Wärnmark, V. Sundström, "A Heteroleptic Ferrous Complex with Mesoionic Bis(1,2,3-triazol-5-ylidene) Ligands: Taming the MLCT Excited State of Iron(II)", *Chemistry – A European Journal* **2015**, *21*, 3628–3639, DOI 10.1002/chem.201405184.

[47] P. Chábera, K. S. Kjaer, O. Prakash, A. Honarfar, Y. Liu, L. A. Fredin, T. C. B. Harlang, S. Lidin, J. Uhlig, V. Sundström, R. Lomoth, P. Persson, K. Wärnmark, "Fe(II) Hexa N-Heterocyclic Carbene Complex with a 528 ps Metal-to-Ligand Charge-Transfer Excited-State Lifetime", *The Journal of Physical Chemistry Letters* **2018**, *9*, 459–463, DOI 10.1021/acs.jpclett.7b02962.

[48] P. Chábera, Y. Liu, O. Prakash, E. Thyrhaug, A. E. Nahhas, A. Honarfar, S. Essén, L. A. Fredin, T. C. B. Harlang, K. S. Kjær, K. Handrup, F. Ericson, H. Tatsuno, K. Morgan, J. Schnadt, L. Häggström, T. Ericsson, A. Sobkowiak, S. Lidin, P. Huang, S. Styring, J. Uhlig, J. Bendix, R. Lomoth, V. Sundström, P. Persson, K. Wärnmark, "A low-spin Fe(III) complex with 100-ps ligand-to-metal charge transfer photoluminescence", *Nature* **2017**, *543*, 695–699, DOI 10.1038/nature21430.

[49] B. Sarkar, L. Suntrup, "Illuminating Iron: Mesoionic Carbenes as Privileged Ligands in Photochemistry", *Angewandte Chemie International Edition* **2017**, *56*, 8938–8940, DOI 10.1002/anie.201704522.

[50] K. S. Kjær, N. Kaul, O. Prakash, P. Chábera, N. W. Rosemann, A. Honarfar, O. Gordivska, L. A. Fredin, K.-E. Bergquist, L. Häggström, T. Ericsson, L. Lindh, A. Yartsev, S. Styring, P. Huang, J. Uhlig,

J. Bendix, D. Strand, V. Sundström, P. Persson, R. Lomoth, K. Wärnmark, "Luminescence and reactivity of a charge-transfer excited iron complex with nanosecond lifetime", *Science* **2019**, *363*, 249–253, DOI 10.1126/science.aau7160.

[51] A. K. Pal, C. Li, G. S. Hanan, E. Zysman-Colman, "Blue-Emissive Cobalt(III) Complexes and Their Use in the Photocatalytic Trifluoromethylation of Polycyclic Aromatic Hydrocarbons", *Angewandte Chemie International Edition* **2018**, *57*, 8027–8031, DOI 10.1002/anie.201802532.

[52] J. Yu, J. Park, A. Van Wyk, G. Rumbles, P. Deria, "Excited-State Electronic Properties in Zr-Based Metal-Organic Frameworks as a Function of a Topological Network", *Journal of the American Chemical Society* **2018**, *140*, 10488–10496, DOI 10.1021/jacs.8b04980.

[53] L. Zhu, B. Zhu, J. Luo, B. Liu, "Design and Property Modulation of Metal-Organic Frameworks with Aggregation-Induced Emission", *ACS Materials Letters* **2021**, *3*, 77–89, DOI 10.1021/acsmaterialslett.0c00477.

[54] M. A. Nasalevich, C. H. Hendon, J. G. Santaclara, K. Svane, B. van der Linden, S. L. Veber, M. V. Fedin, A. J. Houtepen, M. A. van der Veen, F. Kapteijn, A. Walsh, J. Gascon, "Electronic origins of photocatalytic activity in d^0 metal organic frameworks", *Scientific reports* **2016**, *6*, 23676, DOI 10.1038/srep23676.

[55] D. Luo, T. Zuo, J. Zheng, Z.-H. Long, X.-Z. Wang, Y.-L. Huang, X.-P. Zhou, D. Li, "Enabling photocatalytic activity of [Ru(2,2':6',2"-terpyridine)$_2$]$^{2+}$ integrated into a metal–organic framework", *Materials Chemistry Frontiers* **2021**, *5*, 2777–2782, DOI 10.1039/D1QM00024A.

[56] D. Huo, F. Lin, S. Chen, Y. Ni, R. Wang, H. Chen, L. Duan, Y. Ji, A. Zhou, L. Tong, "Ruthenium Complex-Incorporated Two-Dimensional Metal-Organic Frameworks for Cocatalyst-Free Photocatalytic Proton Reduction from Water", *Inorganic Chemistry* **2020**, *59*, 2379–2386, DOI 10.1021/acs.inorgchem.9b03250.

[57] D. W. Thompson, C. N. Fleming, B. D. Myron, T. J. Meyer, "Rigid Medium Stabilization of Metal-to-Ligand Charge Transfer Excited States", *The Journal of Physical Chemistry B* **2007**, *111*, 6930–6941, DOI 10.1021/jp0686821.

[58] D. Micheroni, Z. Lin, Y.-S. Chen, W. Lin, "Luminescence Enhancement of cis- $[Ru(bpy)_2(py)_2]^{2+}$ via Confinement within a Metal-Organic Framework", *Inorganic Chemistry* **2019**, *58*, 7645–7648, DOI 10.1021/acs.inorgchem.9b00396.

[59] J. M. Mayers, R. W. Larsen, "Modulation of Osmium(II) Tris(2,2'-bipyridine) Photophysics through Encapsulation within Zinc(II) Trimesic Acid Metal Organic Frameworks", *Inorganic Chemistry* **2020**, *59*, 7761–7767, DOI 10.1021/acs.inorgchem.0c00807.

[60] L. F. Szczepura, L. M. Witham, K. J. Takeuchi, "Tris(2-pyridyl) tripod ligands", *Coordination Chemistry Reviews* **1998**, *174*, 5–32, DOI 10.1016/S0010-8545(98)00122-2.

[61] A. J. Plajer, A. L. Colebatch, F. J. Rizzuto, P. Pröhm, A. D. Bond, R. García-Rodríguez, D. S. Wright, "How Changing the Bridgehead Can Affect the Properties of Tripodal Ligands", *Angewandte Chemie International Edition* **2018**, *57*, 6648–6652, DOI 10.1002/anie.201802350.

[62] J. P. Wibaut, A. P. de Jonge, H. G. P. van der Voort, P. P. H. L. Otto, "Syntheses with the aid of lithiopyridines: Preparation of di-pyridyl ketones, pyridyl-phenyl-carbinols and tri-pyridyl-carbinols", *Recueil des Travaux Chimiques des Pays-Bas* **1951**, *70*, 1054–1066, DOI 10.1002/recl.19510701206.

[63] A. Santoro, C. Sambiagio, P. C. McGowan, M. A. Halcrow, "Synthesis and coordination chemistry of 1,1,1-tris-(pyrid-2-yl)ethane", *Dalton Transactions* **2014**, *44*, 1060–1069, DOI 10.1039/C4DT02824D.

[64] S. Treiling, C. Wang, C. Förster, F. Reichenauer, J. Kalmbach, P. Boden, J. P. Harris, L. M. Carrella, E. Rentschler, U. Resch-Genger, C. Reber, M. Seitz, M. Gerhards, K. Heinze, "Luminescence and Light-Driven Energy and Electron Transfer from an Exceptionally Long-Lived Excited State of a Non-Innocent Chromium(III) Complex", *Angewandte Chemie International Edition* **2019**, *58*, 18075–18085, DOI 10.1002/anie.201909325.

[65] M. J. Frisch, G. W. Trucks, H. B. Schlegel, G. E. Scuseria, M. A. Robb, J. R. Cheeseman, G. Scalmani, V. Barone, G. A. Petersson, H. Nakatsuji, X. Li, M. Caricato, A. V. Marenich, J. Bloino, B. G. Janesko, R. Gomperts, B. Mennucci, H. P. Hratchian, J. V. Ortiz, A. F. Izmaylov, J. L. Sonnenberg, D. Williams-Young, F. Ding, F. Lipparini, F. Egidi, J. Goings, B. Peng, A. Petrone, T. Henderson, D. Ranasinghe, V. G. Zakrzewski, J. Gao, N. Rega, G. Zheng, W. Liang, M. Hada, M. Ehara, K. Toyota, R. Fukuda, J. Hasegawa, M. Ishida, T. Nakajima, Y. Honda, O. Kitao, H. Nakai, T. Vreven, K. Throssell, J. A. Montgomery, Jr., J. E. Peralta, F. Ogliaro, M. J. Bearpark, J. J. Heyd, E. N. Brothers, K. N. Kudin, V. N. Staroverov, T. A. Keith, R. Kobayashi, J. Normand, K. Raghavachari, A. P. Rendell, J. C. Burant, S. S. Iyengar, J. Tomasi, M. Cossi, J. M. Millam, M. Klene, C. Adamo, R. Cammi, J. W. Ochterski, R. L. Martin, K. Morokuma, O. Farkas, J. B. Foresman, D. J. Fox, *Gaussian 16 Revision B.01*, **2016**.

[66] A. D. Becke, "Density-functional exchange-energy approximation with correct asymptotic behavior", *Phys. Rev. A* **1988**, *38*, 3098–3100, DOI 10.1103/PhysRevA.38.3098.

[67] W. G. Kofron, L. M. Baclawski, "A convenient method for estimation of alkyllithium concentrations", *The Journal of Organic Chemistry* **1976**, *41*, 1879–1880, DOI 10.1021/jo00872a047.

[68] C. E. Stivala, A. Zakarian, "Highly Enantioselective Direct Alkylation of Arylacetic Acids with Chiral Lithium Amides as Traceless Auxiliaries", *Journal of the American Chemical Society* **2011**, *133*, 11936–11939, DOI 10.1021/ja205107x.

[69] G. M. Sheldrick, "A short history of SHELX", *Acta Crystallographica Section A: Foundations of Crystallography* **2008**, *64*, 112–122, DOI 10.1107/S0108767307043930.

[70] G. M. Sheldrick, "SHELXT - Integrated space-group and crystal-structure determination", *Acta Crystallographica Section A* **2015**, *71*, 3–8, DOI 10.1107/S2053273314026370.

[71] O. V. Dolomanov, L. J. Bourhis, R. J. Gildea, J. a. K. Howard, H. Puschmann, "OLEX2: a complete structure solution, refinement

and analysis program", *Journal of Applied Crystallography* **2009**, *42*, 339–341, DOI 10.1107/S0021889808042726.

[72] C. Bannwarth, E. Caldeweyher, S. Ehlert, A. Hansen, P. Pracht, J. Seibert, S. Spicher, S. Grimme, "Extended tight-binding quantum chemistry methods", *WIREs Computational Molecular Science* **2021**, *11*, e1493, DOI 10.1002/wcms.1493.

[73] S. Grimme, C. Bannwarth, P. Shushkov, "A Robust and Accurate Tight-Binding Quantum Chemical Method for Structures, Vibrational Frequencies, and Noncovalent Interactions of Large Molecular Systems Parametrized for All spd-Block Elements (Z = 1-86)", *Journal of Chemical Theory and Computation* **2017**, *13*, 1989–2009, DOI 10.1021/acs.jctc.7b00118.

[74] S. Grimme, C. Bannwarth, "Ultra-fast computation of electronic spectra for large systems by tight-binding based simplified Tamm-Dancoff approximation (sTDA-xTB)", *The Journal of Chemical Physics* **2016**, *145*, 054103, DOI 10.1063/1.4959605.

[75] J. Tao, J. P. Perdew, V. N. Staroverov, G. E. Scuseria, "Climbing the Density Functional Ladder: Nonempirical Meta-Generalized Gradient Approximation Designed for Molecules and Solids", *Physical Review Letters* **2003**, *91*, 146401, DOI 10.1103/PhysRevLett.91.146401.

[76] R. G. Pearson, "Hard and Soft Acids and Bases", *Journal of the American Chemical Society* **1963**, *85*, 3533–3539, DOI 10.1021/ja00905a001.

[77] H. Li, M. Eddaoudi, T. L. Groy, O. M. Yaghi, "Establishing Microporosity in Open Metal-Organic Frameworks: Gas Sorption Isotherms for Zn(BDC) (BDC = 1,4-Benzenedicarboxylate)", *Journal of the American Chemical Society* **1998**, *120*, 8571–8572, DOI 10.1021/ja981669x.

[78] H. Chun, D. N. Dybtsev, H. Kim, K. Kim, "Synthesis, X-ray Crystal Structures, and Gas Sorption Properties of Pillared Square Grid Nets Based on Paddle-Wheel Motifs: Implications for Hydrogen Storage in Porous Materials", *Chemistry – A European Journal* **2005**, *11*, 3521–3529, DOI 10.1002/chem.200401201.

[79] H. Li, M. Eddaoudi, M. O'Keeffe, O. M. Yaghi, "Design and synthesis of an exceptionally stable and highly porous metal-organic framework", *Nature* **1999**, *402*, 276–279, DOI 10.1038/46248.

[80] S. Vagin, A. K. Ott, B. Rieger, "Paddle-Wheel Zinc Carboxylate Clusters as Building Units for Metal-Organic Frameworks", *Chemie Ingenieur Technik* **2007**, *79*, 767–780, DOI 10.1002/cite.200700062.

[81] K. I. Hadjiivanov, D. A. Panayotov, M. Y. Mihaylov, E. Z. Ivanova, K. K. Chakarova, S. M. Andonova, N. L. Drenchev, "Power of Infrared and Raman Spectroscopies to Characterize Metal-Organic Frameworks and Investigate Their Interaction with Guest Molecules", *Chemical Reviews* **2021**, *121*, 1286–1424, DOI 10.1021/acs.chemrev.0c00487.

[82] Y. Bai, Y. Dou, L.-H. Xie, W. Rutledge, J.-R. Li, H.-C. Zhou, "Zr-based metal-organic frameworks: design, synthesis, structure, and applications", *Chemical Society Reviews* **2016**, *45*, 2327–2367, DOI 10.1039/C5CS00837A.

[83] D. Feng, Z.-Y. Gu, Y.-P. Chen, J. Park, Z. Wei, Y. Sun, M. Bosch, S. Yuan, H.-C. Zhou, "A Highly Stable Porphyrinic Zirconium Metal-Organic Framework with shp-a Topology", *Journal of the American Chemical Society* **2014**, *136*, 17714–17717, DOI 10.1021/ja510525s.

[84] V. Bon, I. Senkovska, I. A. Baburin, S. Kaskel, "Zr- and Hf-Based Metal-Organic Frameworks: Tracking Down the Polymorphism", *Crystal Growth & Design* **2013**, *13*, 1231–1237, DOI 10.1021/cg301691d.

[85] D. Feng, Z.-Y. Gu, J.-R. Li, H.-L. Jiang, Z. Wei, H.-C. Zhou, "Zirconium-Metalloporphyrin PCN-222: Mesoporous Metal–Organic Frameworks with Ultrahigh Stability as Biomimetic Catalysts", *Angewandte Chemie International Edition* **2012**, *51*, 10307–10310, DOI 10.1002/anie.201204475.

[86] H.-L. Jiang, D. Feng, K. Wang, Z.-Y. Gu, Z. Wei, Y.-P. Chen, H.-C. Zhou, "An Exceptionally Stable, Porphyrinic Zr Metal-Organic Framework Exhibiting pH-Dependent Fluorescence", *Journal of the American Chemical Society* **2013**, *135*, 13934–13938, DOI 10.1021/ja406844r.

[87] D. Feng, W.-C. Chung, Z. Wei, Z.-Y. Gu, H.-L. Jiang, Y.-P. Chen, D. J. Darensbourg, H.-C. Zhou, "Construction of Ultrastable Porphyrin Zr Metal-Organic Frameworks through Linker Elimination", *Journal of the American Chemical Society* **2013**, *135*, 17105–17110, DOI 10.1021/ja408084j.

[88] D. Feng, K. Wang, J. Su, T.-F. Liu, J. Park, Z. Wei, M. Bosch, A. Yakovenko, X. Zou, H.-C. Zhou, "A Highly Stable Zeotype Mesoporous Zirconium Metal-Organic Framework with Ultralarge Pores", *Angewandte Chemie International Edition* **2015**, *54*, 149–154, DOI 10.1002/anie.201409334.

[89] D. Feng, H.-L. Jiang, Y.-P. Chen, Z.-Y. Gu, Z. Wei, H.-C. Zhou, "Metal-Organic Frameworks Based on Previously Unknown Zr_8/Hf_8 Cubic Clusters", *Inorganic Chemistry* **2013**, *52*, 12661–12667, DOI 10.1021/ic4018536.

[90] M. Taddei, F. Costantino, F. Marmottini, A. Comotti, P. Sozzani, R. Vivani, "The first route to highly stable crystalline microporous zirconium phosphonate metal-organic frameworks", *Chemical Communications* **2014**, *50*, 14831–14834, DOI 10.1039/C4CC06223J.

[91] M. Taddei, F. Costantino, R. Vivani, "Synthesis and Crystal Structure from X-ray Powder Diffraction Data of Two Zirconium Diphosphonates Containing Piperazine Groups", *Inorganic Chemistry* **2010**, *49*, 9664–9670, DOI 10.1021/ic1014048.

[92] M. Taddei, F. Costantino, R. Vivani, S. Sabatini, S.-H. Lim, S. M. Cohen, "The use of a rigid tritopic phosphonic ligand for the synthesis of a robust honeycomb-like layered zirconium phosphonate framework", *Chemical Communications* **2014**, *50*, 5737–5740, DOI 10.1039/C4CC01253D.

[93] V. Guillerm, F. Ragon, M. Dan-Hardi, T. Devic, M. Vishnuvarthan, B. Campo, A. Vimont, G. Clet, Q. Yang, G. Maurin, G. Férey, A. Vittadini, S. Gross, C. Serre, "A Series of Isoreticular, Highly Stable, Porous Zirconium Oxide Based Metal-Organic Frameworks", *Angewandte Chemie International Edition* **2012**, *51*, 9267–9271, DOI 10.1002/anie.201204806.

[94] W. Liang, R. Babarao, T. L. Church, D. M. D'Alessandro, "Tuning the cavities of zirconium-based MIL-140 frameworks to modulate CO_2 adsorption", *Chemical Communications* **2015**, *51*, 11286–11289, DOI 10.1039/C5CC02539G.

[95] L. Cooper, N. Guillou, C. Martineau, E. Elkaim, F. Taulelle, C. Serre, T. Devic, "ZrIV Coordination Polymers Based on a Naturally Occurring Phenolic Derivative", *European Journal of Inorganic Chemistry* **2014**, *2014*, 6281–6289, DOI 10.1002/ejic.201402891.

[96] G. Mouchaham, L. Cooper, N. Guillou, C. Martineau, E. Elkaïm, S. Bourrelly, P. L. Llewellyn, C. Allain, G. Clavier, C. Serre, T. Devic, "A Robust Infinite Zirconium Phenolate Building Unit to Enhance the Chemical Stability of Zr MOFs", *Angewandte Chemie International Edition* **2015**, *54*, 13297–13301, DOI 10.1002/anie.201507058.

[97] A. Schaate, P. Roy, A. Godt, J. Lippke, F. Waltz, M. Wiebcke, P. Behrens, "Modulated Synthesis of Zr-Based Metal-Organic Frameworks: From Nano to Single Crystals", *Chemistry – A European Journal* **2011**, *17*, 6643–6651, DOI 10.1002/chem.201003211.

[98] X.-P. Wu, L. Gagliardi, D. G. Truhlar, "Cerium Metal-Organic Framework for Photocatalysis", *Journal of the American Chemical Society* **2018**, *140*, 7904–7912, DOI 10.1021/jacs.8b03613.

[99] R. J. Marshall, T. Richards, C. L. Hobday, C. F. Murphie, C. Wilson, S. A. Moggach, T. D. Bennett, R. S. Forgan, "Postsynthetic bromination of UiO-66 analogues: altering linker flexibility and mechanical compliance", *Dalton Transactions* **2016**, *45*, 4132–4135, DOI 10.1039/C5DT03178H.

[100] X. Xu, F. Yang, S.-L. Chen, J. He, Y. Xu, W. Wei, "Dynamic behaviours of a rationally prepared flexible MOF by postsynthetic modification of ligand struts", *Chemical Communications* **2017**, *53*, 3220–3223, DOI 10.1039/C7CC00230K.

[101] X. Xu, F. Yang, H. Han, Y. Xu, W. Wei, "Postsynthetic Addition of Ligand Struts in Metal–Organic Frameworks: Effect of Syn/Anti Addition on Framework Structures with Distinct Topologies", *Inorganic Chemistry* **2018**, *57*, 2369–2372, DOI 10.1021/acs.inorgchem.7b02899.

[102] R. J. Marshall, S. L. Griffin, C. Wilson, R. S. Forgan, "Single-Crystal to Single-Crystal Mechanical Contraction of Metal–Organic Frameworks through Stereoselective Postsynthetic Bromination", *Journal of the American Chemical Society* **2015**, *137*, 9527–9530, DOI 10.1021/jacs.5b05434.

[103] H. Furukawa, F. Gándara, Y.-B. Zhang, J. Jiang, W. L. Queen, M. R. Hudson, O. M. Yaghi, "Water Adsorption in Porous Metal-Organic Frameworks and Related Materials", *Journal of the American Chemical Society* **2014**, *136*, 4369–4381, DOI 10.1021/ja500330a.

[104] B. Lafuente, R. T. Downs, H. Yang, N. Stone in *1. The power of databases: The RRUFF project*, De Gruyter (O), **2015**, pp. 1–30, ISBN: 978-3-11-041710-4, DOI 10.1515/9783110417104-003.

[105] X. Zhao, D. Vanderbilt, "Phonons and lattice dielectric properties of zirconia", *Physical Review B* **2002**, *65*, 075105, DOI 10.1103/PhysRevB.65.075105.

[106] P. E. Quintard, P. Barbéris, A. P. Mirgorodsky, T. Merle-Méjean, "Comparative Lattice-Dynamical Study of the Raman Spectra of Monoclinic and Tetragonal Phases of Zirconia and Hafnia", *Journal of the American Ceramic Society* **2002**, *85*, 1745–1749, DOI 10.1111/j.1151-2916.2002.tb00346.x.

[107] L. A. Fredin, K. Wärnmark, V. Sundström, P. Persson, "Molecular and Interfacial Calculations of Iron(II) Light Harvesters", *ChemSusChem* **2016**, *9*, 667–675, DOI 10.1002/cssc.201600062.

[108] A. Harriman, G. Porter, A. Wilowska, "Photoreduction of benzo-1,4-quinone sensitised by metalloporphyrins", *Journal of the Chemical Society Faraday Transactions 2: Molecular and Chemical Physics* **1983**, *79*, 807–816, DOI 10.1039/F29837900807.

[109] H. Görner, "Photoprocesses of p-Benzoquinones in Aqueous Solution", *The Journal of Physical Chemistry A* **2003**, *107*, 11587–11595, DOI 10.1021/jp030789a.